The University of Nottingham

Power Electronics, Machines and Control Group
Department of Electrical and Electronic Engineering

On Multi-Phase Machines and Current Harmonic Injection for Torque Capability Improvement

Daniele De Gaetano

Submitted to University of Nottingham
for the degree of Doctor of Philosophy

April 11, 2022

Abstract

The increased energy demand and the need for electrical machines capable to deliver high torque and power in small volumes is pushing the research community to identify suitable solutions for this target. Nowadays, electrical machines are deeply used also in applications where the weight containment is important such as automotive and aerospace.

Multi-phase electrical machines are a suitable candidate to help to get this goal. They present different advantages with respect to classical three-phase machines for example an increased machine torque capability and more tolerance to sustain fault conditions. The average torque is increased thanks to an improved winding factor whereas the fault tolerance improvement is due to the higher number of machine phases. In addition, the torque ripple is lower thanks to an improved magneto-motive force distribution. Moreover, the voltage on the single converter is lower, supplying the machine with the same current of a three-phase system. Another important advantage for the multi-phase arrangement is the possibility to control more harmonics of magnetic field independently thanks to the more degrees of freedom. It means new possibilities to implement various control techniques for improving the machine performance by the injection of additional harmonics higher than the fundamental.

This thesis describes the work which has been carried out in the past three years, during the Ph.D program with the results achieved by analytical model implementations, finite element analysis simulations and experimental tests. The main target is to improve the machine torque capability and/or reduce its permanent magnet content. To reach this goal, the multi-phase re-arrangement of three-phase machines and current harmonic injection techniques are proposed for different machine topologies.

An analytical model is implemented to reduce the magnet content in surface permanent magnet machines without affecting Joule losses and the average torque. The analytical

model is validated via FEA.

A model-free technique to improve the torque capability by current harmonic injection is proposed and its concept is validated experimentally on a V-Shape interior permanent magnet machine. Sensitivity analyses are carried out to optimise the V-Shape rotor configuration to improve the torque under fifth current harmonic injection.

Studying the flux density in the stator core on a classical three-phase surface permanent magnet machine with a distributed winding layout, it is possible to highlight another advantage of multi-phase machines which consists in a better flux density distribution.

The proposed work gives a contribution to the research community in terms of new solutions for increasing the torque capability and/or reducing the permanent magnet content in the machine without affecting its efficiency for different rotor topologies. Moreover, the proposed stator flux density analysis can give important information about the electromagnetic behaviour in three-phase distributed winding surface permanent magnet machines.

Acknowledgements

In this section, I would like to express my gratitude to people who accompanied me during my Ph.D degree.

First of all, many thanks to my supervisors Prof. Michele Degano, Dr. Giacomo Sala and Prof. Chris Gerada without whom would not have been possible this amazing period as research student. In particular, special thanks to Dr. Michele Degano and Dr. Giacomo Sala who supported me on both technically and morally.

Additionally, I am very grateful to all my friends and colleagues who endured me during these three and more years. Thanks to them, I can call Nottingham "home".

I would like to spend some words for my friend Dr. Alessandro Costabeber. He was an amazing researcher of inspiration for all people whom want to start the research and teaching careers, but mostly, he was an amazing guy, friendly and always available with everybody.

A big thank you goes to my family who always supported me.

Finally, I would like to dedicate this thesis to my cousin Giuseppe who would has been proud of me for this important achievement, surely.

Contents

List of Figures

List of Tables

Chapter 1

Introduction

This chapter presents an overview about multiphase machines and current harmonic injection techniques to improve their performance. After a short introduction of the multiphase machines concept, highlighting the main benefits, particular emphasis is given to the current harmonic injection techniques which is the focus of this work. The motivations and thesis outline are also here presented. Finally, the scientific contributions are described together with the list of publications resulting from the research work carried out.

1.1 Overview on multiphase machines and current harmonic injection

Nowadays, thanks to the power electronics introduction, the electrical machines can be decoupled from the supply source, so that they can be studied and designed with an arbitrary number of phases m. This concept permits to think more complex designs and controls

thanks to the more freedom of degrees given by each additional phase than the classical three. An intrinsic benefit of the multi-phase concept is the possibility to reduce the voltage on the power drives supplying the same current of the three-phase winding arrangement. For example, a nine-phase machine system can be supplied by three different inverters which supply the machine with the same current of one inverter for a classical three-phase configuration but the voltage is three times lower on each of them. This benefit is really important for high power drives applications, such as the electric ship propulsion [1]- [7], but it can fit also for low power applications as the automotive sector [8], [9]; the main advantage is from a sizing point of view. Viceversa, it is possible to reduce the current on each inverter leg, by means reducing the inverter switches size, to keep the same voltage. It is really important where the target is to work with higher switching frequencies. Indeed, the reduced power of electronic components permits their commuting frequencies increment. The multi-phase approach can be applied on existent machines with a winding re-arrangement or on new machines which can be designed starting from the multi-phase concept directly. In both cases, the multi-phase winding layout gives the possibility to apply control techniques which permit to inject more independent current harmonics in the phases and control more magnetic field harmonics at the airgap with respect to the classical three-phase winding layout. The multi-phase machine re-arrangement is based on the slots and poles combination. Therefore, it strongly depends from the machine design. Usually, the multi-phase winding layout is configured as sum of three-phase subsystems which can be asymmetrical and symmetrical [10]. In the asymmetrical configuration the different three-phase subsystems are not equally shifted in the space with a phase progression $\beta = \pi/m$ whereas the symmetrical one presents a phase progression of $\beta = 2\pi/m$ which means that the phase are equally distributed in the space. An example of a dual three-phase winding arrangement in both configurations asymmetrical and symmetrical is shown in Fig. 1.1.

As well known, the constraints on the current control is related to the number phases m and the star connection of the system Nstar by the relationship m-Nstar. Therefore, an higher

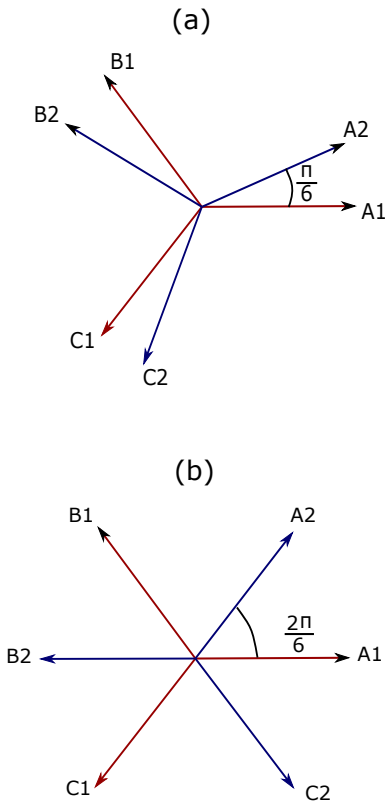

Figure 1.1: Two possible magnetic axis configurations of a generic dual three-phase winding arrangement: (a) asymmetrical - (b) symmetrical.

number of phases permits to control the magnetic field generated by different stator current harmonics separately as mentioned already. For example, the three-phase system gives the possibility to control only two currents independently, meaning that only the magnetic field generated by the fundamental stator current can be controlled. In contrast, the control of four current harmonics in a separate way is possible for a dual three-phase system, controlling the fundamental magnetic field and an higher order one. Indeed, additional harmonics of the armature magnetic field can be controlled by each pair of injected additional currents.

The benefits of multi-phase machines can be summarised with improved performance, lower

vibrations and acoustic noise, a better fault tolerance and the possibility to implement new control techniques thanks to the more degrees of freedom of the system [11].

Even if this thesis focuses on improved performance due to the multiphase machines with and without current harmonic injection, it looks worth to introduce shortly the other main benefit of the multiphase system: the improved fault tolerance. The main faults of electrical machines can be summarised in open/short circuit faults and high resistance connections due to the winding deterioration. Other faults which can depend to the machine electromagnetic behaviour are rotor cage faults, bearing faults, eccentricities, permanent magnet demagnetisation and sensor fault. A short number of papers are following proposed for the main faults mitigation only. The multiphase machines present an internal redundancy. Indeed, if one phase is opened, the others can compensate the missing power, minimising the performance and avoiding the machine failure [12]. The fault tolerance strategies depend strongly by the machine topology [13]- [16]. A possible solution to improve the performance in fault conditions could be supply, with suitable currents, the remaining healthy phases [17]. Usually, the high resistance faults are compensate by PI regulators. However, better performance are obtained using additional inverse sequence or resonance regulators, which is proposed in [18] for multiphase systems. Many works are oriented to find solutions for avoiding the machine failure due to the short circuit faults. Fault tolerance controls to maintain the same performance of the healthy machine, increasing the phase currents significantly, are proposed in [19] and [20] whereas in [21] the short circuit current is kept to zero compensating the faulty phase back electro-motive force by using the healthy ones.

As mentioned already, multi-phase machines can increase, in a significant way, the performance with respect to a classical three-phase one. Indeed, the machine torque capability and the output power consequently can be increased by improving the winding factor thanks to a better distribution in the stator phases. Indeed, it is possible to maximise the fundamental spatial harmonic of the magneto-motive force and minimising the non-fundamental ones taking into account the current phase shift control. Various machine and drive topolo-

gies are used for the different applications. An overview of multi-phase machines and drives in the transportation field such as road vehicles, rail, aircraft and ship is proposed in [22].

The higher number of phases permit to implement more control strategies to increase the output torque. Usually, these techniques use the injection of current harmonics with an order higher than the fundamental [23]- [25]. They are known as current harmonic injection techniques. This mentioned techniques require a detailed investigation for the different machine topologies. Indeed, their effects depending strongly from the design and machine topology. In [26], the authors apply the third current harmonic injection on a dual three-phase SPM machine, where the optimum third harmonic current value is derived analytically, taking into account both constant peak and root-mean-square (RMS) current constrains. It shows that the torque can be improved by 15% for a machine which does not present a third harmonic in the back electro-motive force. If this component is present, the torque can be further improved based on the interaction between the third harmonic of magneto-motive forces generated by rotor and stator. The third harmonic injection for maximising the torque is investigated also for a five-phase SPM machine with unequal stator teeth in [27]. It shows that the torque can be improved by 2.1% for a 10 slots/8 poles unequal stator teeth machine under third current harmonic injection with the constrain to keep the same RMS value. The article [28] proposes the third harmonic injection applied on a five-phase dual rotor machine. It highlights the advantages of the dual rotor solution which can be designed with a thin back iron. In this way, it is possible to design the rotor configurations to generate a trapezoidal flux density at the airgap to permit a better torque improvement under current harmonic injection and in the same time to keep under control the machine iron losses. A strategy to increase the torque injecting fifth and seventh harmonic of current is implemented on a dual three-phase SPM machine in [29], where it is shown that the average torque can be improved by 8.6% thanks to the proposed technique. A modelling approach to inject the third harmonic in isotropic permanent magnet machines for a generic winding configuration based on the vector space decomposition and rotational

transformation is presented in [30]. The work strategy is to minimise the average stator winding losses for a given reference torque by using the airgap flux density third and first spatial harmonics. An algorithm for designing symmetrical multi-phase concentrated windings for maximizing the average torque considering the non-fundamental spatial harmonics to produce the torque in order to inject additional current harmonics for SPM machines is proposed in [31]. A general approach for the torque enhancement on a nine-phase SPM machine is proposed for different magnet span injecting the third and fifth current harmonics [32]. First, the optimum rotor configuration has been found for the proposed control and then the analysis until the current seventh harmonic injection is carried out. The paper shows that there is the possibility to increase the torque by 45%. It is clear that the harmonic injection technique has been well investigated in literature for isotropic permanent magnet machines. It shows that to know the back electro-motive force is a fundamental aspect to implement appropriate control algorithms. Indeed, the state-of-art current harmonic injection techniques for SPM machines are based on the current amplitudes obtained directly by the back electro-motive force values. Therefore, they strongly depend from the machine design, for example permanent magnet span percentage on the rotor surface.

However, there is a lower number of works on the current harmonic injection for increasing the torque production for IPM machines. It is applied to improve the torque capability and reduce the ripple is applied on an anisotropic doubly salient synchronous reluctance machine for different multi-phase configurations in [33], finding the optimum injection values by a study on the interaction between self and mutual inductances with the current harmonics, where the investigation takes into account losses and dynamic performance in different torque regions. In [34], the current injection technique to increase the torque on both SPM and IPM machines is proposed without crossing the peak current limit and using a look-up table for the injection algorithm. The paper proposes a torque model considering the harmonics in the permanent magnet flux linkages, inductances and stator currents in order to investigate the induced torque components which are used in the current harmonic

design to improve the maximum torque per peak current control. The article [35] offers a comparative study between doubly salient synchronous reluctance machines with three different winding configurations by using a current harmonic injection technique. This technique permits to mitigate the torque ripple produced by the fundamental current generating an opposite one, presenting an improvement of the average torque at the same time. The authors in [36] propose an analytical model for three-phase, 12-slot/8-pole single layer doubly salient synchronous reluctance machines. It is shown that the third current harmonic injection improves the average torque and reduces the torque ripple in the constant region, while maintaining similar torque performance of the machine supplied with the fundamental current only in the flux weakening region. Moreover, the paper shows that the injection of the fifth or seventh current harmonics reduces the output torque. A second current harmonic method is developed for a 6 stator slots/4 rotor teeth variable flux reluctance machine in order to enhance the torque density in [37]. The paper displays that applying the proposed method the output torque can be improved by 22%, with the drawback of a larger torque ripple. In [38], the authors investigate on a current harmonic injection method to optimise the flux density at the air-gap and in the yoke simultaneously for a multiphase induction motor. The method works under heavy load conditions, improving the torque by 8.47%. Huang et al. investigate the feasibility and effectiveness of the second current harmonic injection technique in variable flux reluctance machines with different stator/pole combinations [39] . It shows that the second harmonic current injection is only effective in $6j/(6i \pm 2)j$ stator/pole e.g., 6/4, 6/8, 12/4, 12/8. It is clear that the control algorithms need a different approach with respect to the state-of-art for the SPM machine. Indeed, the reluctance effects due to the anisotropic topology cannot be neglected, having a strong impact on the control algorithm injection. Even in this case, it is important to know in advance the electromagnetic behaviour of the machine in order to set up an appropriate control algorithm. The literature lacks about current harmonic injection technique controls which do not need to know in advance any machine values i.e., model-free techniques.

1.2 Motivations

From the literature, it is clear that the multi-phase approach combined with the current harmonic injection technique, can lead to important benefits in terms of machine torque capability improvement. Starting from the previous knowledge, it seems worth to investigate more on the multi-phase and current harmonic injection solutions to get improved torque per volume machines. The literature presents many work focused on the torque improvement by current harmonic injection for SPM and just a few for anisotropic machines such as IPM. Moreover it lacks about techniques which do not need to know in advance any machine values. Therefore, to find a model-free solution, which can be suitable for both machine topologies, is one of the target of this thesis. The multi-phase and current harmonic injection approaches can be used on existing machines which were originally designed with a classical three-phase winding layout supplied by a sinusoidal current. Therefore, this combination of solutions can give "new life" to the machines without excessive costs, improving their power density or decreasing the Joule losses for a reference torque. On the other hand, optimising the rotor starting from multi-phase machines which are supplied by a non-sinusoidal current can give the possibility to reduce the permanent magnet content into the machine, keeping high propulsion performance. Nowadays, reducing the magnets amount, keeping high power density, is one of the biggest challenges for the research community. Indeed, rare earth permanent magnets have high performance in terms of flux production per volume but with the drawbacks of high and fluctuating costs.

Additionally, the stator core flux density distribution in three-phase and multi-phase machines needs to be study for understanding the two different winding layouts behaviour.

1.3 Thesis Outline

This Ph.D thesis focuses on multi-phase machines and the identification of techniques to improve their torque capability. A number of studies are carried out on different machine topologies, which originally were designed with classical three-phase winding arrangements, supplied with a sinusoidal current. An important part of the proposed thesis work investigates the possibility to increase the average torque by injecting current harmonics with a higher order than the fundamental. Based on the control with current harmonic injection, the possibility to reduce the PM content without affect both torque performance and Joule losses in SPM and IPM machines is also investigated.

Chapter 2 highlights the benefit in terms of flux density distribution in the stator core for a SPM machine with a triple three-phase winding arrangement with respect to the three-phase one. Firstly, an analytical model is carried out in order to study the flux density in the stator core for a three-phase distributed winding layout SPM machine. Based on the flux density analysis, which is validated via Finite Element Analysis (FEA), an asymmetrical stator teeth design is proposed for the three-phase machine. At the end, a comparison between the triple three-phase and classical three-phase winding arrangements shows the benefit of the multi-phase approach.

In **chapter 3**, a torque analysis for a three-phase, six-phase and nine-phase distributed winding arrangements is analysed under different current temporal harmonics in order to understand the difference in the stator magneto-motive force behaviour and how it affects the torque. Then, a torque comparison is carried out on a three-phase and dual dual-three-phase distributed winding layouts for an IPM machine V-Shape machine, showing the possibility to reduce the machine volume thanks to the multi-phase re-arrangement.

Chapter 4 proposes an investigation on the possibility to increase the average torque

injecting the third current harmonic on a fractional-slot dual-rotor SPM machine with an Halbach rotor array without over-crossing the peak current;

Chapter 5 studies an analytical model for a triple three-phase SPM machine in order to understand which percentage of Permanent Magnet (PM) on the rotor surface is better than others for injecting current harmonics to keep constant the RMS value. The last analysis shows that it is possible to reduce the PM content in the machine without affecting Joule losses and torque performance.

A current harmonic injection technique, which can be applied on both isotropic (i.e., SPM) and anisotropic (i.e., IPM) machines, is proposed in **chapter 6**. At first stage, the voltage harmonic spectra is investigated for both machine topologies. Based on the analysis, the values for the injection are obtained. At the end, the comparison between the proposed technique, the state-of-art for SPM machine and the optimum obtained via FEA is proposed.

Based on the technique proposed in chapter 6, a sensitivity analysis is carried out in **chapter 7** on a V-shape IPM machine in order to understand which is the best rotor configuration to improve the average torque by injecting the current fifth harmonic with the proposed technique. The analysis shows that designing the machine based on the control with the fifth harmonic injection can give an important reduction of PM content with respect to the machine designed for the classical control with the sinusoidal current, providing similar torque performance.

Chapter 8 proposes an analysis for investigating the optimum direction of magnetisation in order to increase the torque by third current harmonic injection for a synchronous reluctance machine filled with permanent magnets at the bottom flux barriers.

1.4 Scientific Contribution

The main target of this thesis is to identify solutions for improving the torque density in multi-phase machines, increasing it per magnet mass. Therefore, the possibility to reduce the PM content in the machine is also investigated. Part of this thesis studies the electromagnetic behaviour of the flux density distribution in the stator core showing interesting phenomenon.

The key scientific contributions introduced by this Ph.D thesis are here summarised:

- A simplified analytical model to find flux density asymmetries in distributed winding surface permanent magnet machines with the number of slots per pole per phase higher than one and an asymmetrical stator teeth geometry to balance the mentioned asymmetries;
- A model-free current harmonic injection technique in order to increase the torque capability on both isotropic and anisotropic machines without knowing in advance any values for the injection;
- Permanent magnet content reduction on both surface permanent magnet and interior permanent magnet machines by current harmonic injection technique without affecting the torque production.

1.5 List of publications

- Giacomo Sala, **Daniele De Gaetano**, Michele Degano and Chris Gerada, "Asymmetrical Flux Density Distribution in Stator Teeth of Surface Permanent Magnet Machines," 2019 IEEE Workshop on Electrical Machines Design, Control and Diagnosis (WEMDCD), Athens, Greece, 2019, pp. 29-33, doi: 10.1109/WEMDCD.2019.8887831.

- **Daniele De Gaetano**, Dmitry Golovanov, Giacomo Sala, Alessandro Galassini, Michele Degano, Hanafy Mahmoud, Chris Gerada, "Advantages of a Double Three-Phase Winding Layout for a Dual Rotor E-Bike Motor Considering Third Current Harmonic Injection Technique," 2020 IEEE Transportation Electrification Conference & Expo (ITEC), Chicago, IL, USA, 2020, pp. 1159-1164, doi: 10.1109/ITEC48692.2020.9161620.

- Chunyang Gu, Hao Yan, Jiajun Yang, Giacomo Sala, **Daniele De Gaetano**, Xuchen Wang, Alessandro Galassini, Michele Degano, Xin Zhang; Giampaolo Buticchi, "A Multiport Power Conversion System for the More Electric Aircraft," in IEEE Transactions on Transportation Electrification, vol. 6, no. 4, pp. 1707-1720, Dec. 2020, doi: 10.1109/TTE.2020.3019446.

- **Daniele De Gaetano**, Giacomo Sala, Michele Degano, David Gerada, Chris Gerada, "Asymmetrical Stator Geometry Design for Three-Phase Machines with Distributed Winding," IET The 10th International Conference on Power Electronics, Machines and Drives (PEMD 2020), 2021 pp. 497 – 502, doi: 10.1049/icp.2021.1167.

- **Daniele De Gaetano**, Giacomo Sala, Michele Degano, Chris Gerada, "Permanent Magnet Reduction by Current Harmonics Injection for Surface Permanent Magnet Machines," 2021 IEEE Workshop on Electrical Machines Design, Control and Diagnosis (WEMDCD), 2021, pp. 137-142, doi: 10.1109/WEMDCD51469.2021.9425662.

- **Daniele De Gaetano**, Jayakrishnan Harikumaran, Giacomo Sala, Michele Degano, Giampaolo Buticchi and Chris Gerada, "On Torque Improvement by Current Harmonic Injection in Isotropic and Anisotropic Multi-Phase Machines," in IEEE Journal of Emerging and Selected Topics in Industrial Electronics, doi: 10.1109/JESTIE.2021.3105337.

Chapter 2

Flux Density Analysis in the Stator Core of Surface Permanent Magnet Machines with Distributed Windings

For improving efficiency and thermal management of electrical machines, the iron losses computation is a fundamental aspect [40]. It leads strictly to the estimation of the flux density distribution and its behaviour with respect to different harmonic components. In literature, there are several papers which are proposing techniques to minimise the iron losses both analytically and via Finite Element Analysis (FEA) optimisation. In [41], a method for reducing iron losses harmonics due to permanent magnets is proposed. Therefore, the flux density analysis is essential to estimate and minimise iron losses at the design stage [42]-[44]. Other works [45], implement complex subdomain models to predict the flux density

within the stator core always considering symmetrical behaviour [46].

In this chapter, the flux density distribution in different stator teeth has been analysed in detail considering three-phase distributed windings with a single layer and full pitch. Such winding configuration is often chosen in fault-tolerant electrical machines [47], [48].

First, an analytical solution has been implemented to demonstrate analytically the asymmetrical flux density distribution in the stator teeth. It is shown that this phenomenon is depending on the number of slots per pole and per phase in the machine. The flux density asymmetries in the stator core can affect the energy losses and so the efficiency of the machine other than an unbalanced stator core saturation.

Two possible solutions are proposed to balance the flux density asymmetries:

1. *An asymmetrical stator teeth design. Therefore, in this case the flux is balanced changing the stator geometry to keep the same slot area (i.e., same current density) and iron volume (i.e., same weight) of the original machine.*
2. *Passing from a classical three-phase arrangement to a triple three-phase one. In this way, the number per pole and per phase is different with respect to the three-phase winding layout and it permits the flux asymmetries balancing in the stator teeth.*

2.1 Three-phase stator flux density analysis: analytical model

The proposed model is based on a 2D analysis (rotor, or stator, skew have not been considered) with the assumption of radial flux density in the air-gap, no slotting effect and linear materials [49]. Under these hypotheses, the magnetic field in the air-gap can be evaluated

for each angular position (ϑ) in terms of Fourier series as:

$$H(\vartheta) = \sum_{\rho=1}^{\infty} \Re\{(\bar{H}_{S,\rho} + \bar{H}_{PM,\rho})e^{-j\rho\vartheta}\}, \tag{2.1}$$

where $\bar{H}_\rho(\bar{H}_\rho = \bar{H}_{S,\rho}+\bar{H}_{PM,\rho})$ is the ρ^{th} Fourier series component of the spatial distribution of the magnetic field in the air-gap. The ρ^{th} harmonic contribution produced by the stator currents $\bar{H}_{S,\rho}$ can be defined as:

$$\bar{H}_{S,\rho} = \frac{3Nq}{\pi\delta}\frac{K_{a\rho}}{\rho}\bar{i}_\rho^S, \tag{2.2}$$

where N is the number of turns per phase, q the slots per pole and per phase, δ the air-gap thickness and $K_{a\rho}$ is the winding factor for the ρ^{th} field harmonic. The winding factor can be written as:

$$k_{a\rho} = \frac{\sum_{y=1}^{Nc} sin(\rho\frac{\Delta\psi_y}{2})e^{j\rho\psi_y}}{pq}, \tag{2.3}$$

where ψ_y is the angular shift from the magnetic axis of the y-th coil and the magnetic axis of the relative phase and Nc is the coils number and q the number per pole per phase. $\bar{i}_\rho^S$ is the ρ^{th} current space vector defined by the Clarke transformation of the currents for the three-phase winding (U-V-W) considered:

$$\bar{i}_\rho^S = \frac{2}{3}(i_U + i_V e^{j\rho\frac{2\pi}{3}} + i_W e^{j\rho\frac{4\pi}{3}}),\ \rho = 0, 1, ...\infty, \tag{2.4}$$

where j is the unity imaginary number ($j^2 = -1$).

Because the zero sequence current is null, due to the star connection of the three-phase winding layout, it is possible to write the following relationships among the space vectors:

$$\begin{aligned} &\bar{i}_\rho^S = \bar{i}_1^S \quad if\ \rho = 3n+1, \\ &\bar{i}_\rho^S = \bar{i}_1^{S*} \quad if\ \rho = 3n-1, \quad n = 0, 1, 2, ..., \infty. \\ &\bar{i}_\rho^S = 0 \qquad if\ \rho = 3n. \end{aligned} \tag{2.5}$$

Table 2.1: Machines parameters

Slots	Phases	p	q	air-gap	magnet thickness
36	3	2	3	1 [mm]	4 [mm]

It results that the inverse Clarke transformation can be written as:

$$\begin{aligned} i_U &= \frac{i_0}{2} + \Re\{\bar{i}_1\} = \Re\{\bar{i}_1\}, \\ i_V &= \frac{i_0}{2} + \Re\{\bar{i}_1 e^{-j\frac{2\pi}{3}}\} = \Re\{\bar{i}_1 e^{-j\frac{2\pi}{3}}\}, \\ i_W &= \frac{i_0}{2} + \Re\{\bar{i}_1 e^{-j\frac{4\pi}{3}}\} = \Re\{\bar{i}_1 e^{-j\frac{4\pi}{3}}\}. \end{aligned} \tag{2.6}$$

Finally, the rotor magnets contribution, to the ρ^{th} harmonic of field in the air-gap, can be expressed with a good approximation as:

$$\bar{H}_{PM,\rho} = \frac{4B_r\delta_{PM}}{\mu_{PM}\pi\delta}\frac{sin(\rho\Delta_{PM}/2)}{\rho}e^{j\rho\vartheta_r}, \tag{2.7}$$

where B_r is the remanence flux density, δ_{PM} the magnet thickness, μ_{PM} the magnet permeability, Δ_{PM} the magnet angular width, and θ_r the rotor position in electrical radians. Table 2.1 summarises the main machine parameters, where p is the pole pairs number. The air-gap flux density, for the considered SPM machine, when the rotor is aligned with the magnetic axis of phase U ($\theta_r = 0$), is shown in Fig. 2.1.

The figure highlights the two components of the flux: the one produced by the magnets, and the flux generated by the stator currents, when the machine is fed with its rated current ($\bar{i}_\rho^S = ji_q e^{j\vartheta_r}$, with $iq = 683\ A_{pk}$). The total flux density is obtained by the sum of two components. In order to evaluate the flux density in each stator tooth, the proposed model considers that all the flux, under the slot pitch, is crossing the air-gap and flowing through the same tooth. Furthermore, the flux density in the teeth is supposed to be constant in the volume of each tooth.

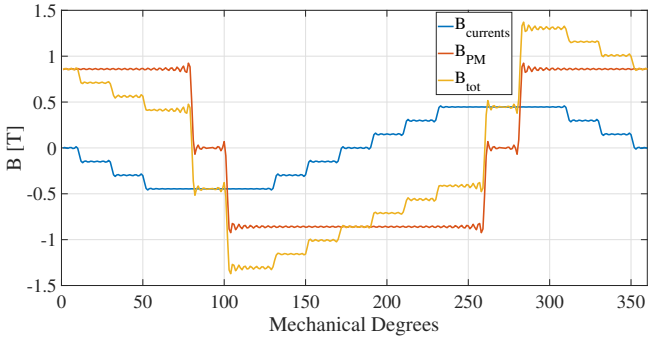

Figure 2.1: Analytical flux density evaluation in the air-gap of a 3 slots per pole and per phase SPM machine. The initial rotor reference position is $\vartheta_r = 0$ and the stator currents corresponding to the rated condition (100 spatial harmonics are considered).

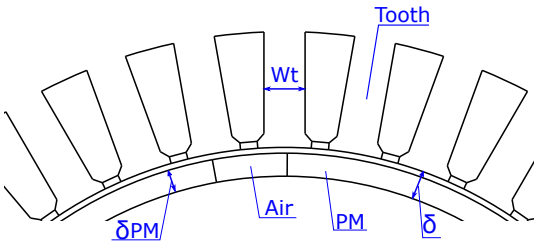

Figure 2.2: Sketch geometry of the proposed SPM machine

From these additional assumptions, the flux of each tooth is evaluated integrating the flux density in the air-gap surface facing the tooth and covering the arch between the centres of the neighbouring slots. The sketch geometry is shown in Fig. 2.2.

Therefore, the analytical evaluation of the teeth flux is provided for each T^{th} tooth by:

$$\Phi_T = \int_{\vartheta_T - \frac{\Delta_{slot}}{2}}^{\vartheta_T + \frac{\Delta_{slot}}{2}} \mu_0 H(\vartheta) L R_g d\vartheta, \tag{2.8}$$

with $\vartheta_T = \frac{2\pi p}{N_{slots}}(T-1)$ the angular position of the centre of the T^{th} tooth (N_{slots} is the overall slot number of the stator), $\Delta_{slot} = \frac{2\pi p}{N_{slots}}$ the angular pitch between two neighbouring slots (or teeth), L the active length of the machine, and R_g the middle radius of the air-gap. Substituting (2.1), with (2.2) and (2.7), in (2.8) it is possible to define the T^{th} tooth flux

in terms of Fourier series as:

$$\Phi_T = \sum_{\rho=1}^{\infty} \Re\{\bar{\Phi}_{T\rho}\}, \tag{2.9}$$

with:

$$\bar{\Phi}_{T\rho} = 2\mu_0 L R_g \frac{sin(\rho\frac{\Delta_{slot}}{2})}{\rho}(\bar{H}_{S,\rho} + \bar{H}_{PM,\rho})e^{-j\rho\vartheta_T} \tag{2.10}$$

Under the assumption of the model, the flux density related to one tooth can be evaluated as:

$$\begin{aligned} B_T =& \frac{\Phi_T}{w_{tooth}} = \frac{2\mu_0 L R_g}{w_{tooth}} \\ & \sum_{\rho=1}^{\infty} \frac{sin(\rho\frac{\Delta_{slot}}{2})}{\rho} \Re\{(\bar{H}_{S,\rho} + \bar{H}_{PM,\rho})e^{-j\rho\vartheta_T}\} \end{aligned} \tag{2.11}$$

Eq. 2.11 can be rewritten in terms of Fourier series as:

$$B_T = \sum_{\rho=1}^{\infty} \Re\{\bar{B}_{T,S\rho} + \bar{B}_{T,PM\rho}\}, \tag{2.12}$$

with the stator contribution:

$$\begin{aligned} \bar{B}_{T,S\rho} =& [\frac{2\mu_0 L R_g}{w_{tooth}} \frac{sin(\rho\frac{\Delta_{slot}}{2})}{\rho} \frac{3Nq}{\pi\delta} \frac{K_{a\rho}}{\rho}]\bar{i}_\rho^S e^{-j\rho\vartheta_T} = \\ =& K_{S\rho}\bar{i}_\rho^S e^{-j\rho\vartheta_T}, \end{aligned} \tag{2.13}$$

and the rotor contribution:

$$\begin{aligned} \bar{B}_{T,PM\rho} =& [\frac{2\mu_0 L R_g}{w_{tooth}} \frac{sin(\rho\frac{\Delta_{slot}}{2})}{\rho} \frac{4B_r\delta_{PM}}{\mu_{PM}\pi\delta} \frac{sin(\rho\Delta_{PM}/2)}{\rho}] \\ & e^{j\rho\vartheta_r} e^{-j\rho\vartheta_T} = K_{PM\rho} e^{j\rho(\vartheta_r - \vartheta_T)}, \end{aligned} \tag{2.14}$$

with $K_{S\rho}$ and $K_{PM\rho}$ constants depending from the harmonic order.

In case of an MTPA current control algorithm the stator contributions can be expressed considering for (2.5) as:

$$\begin{aligned} \bar{B}_{T,S\rho} &= jK_{S\rho} i_q e^{j(\vartheta_r - \rho\vartheta_T)} && if\ \rho = 3n+1, \\ \bar{B}_{T,S\rho} &= -jK_{S\rho} i_q e^{-j(\vartheta_r + \rho\vartheta_T)} && if\ \rho = 3n-1, \\ \bar{B}_{T,S\rho} &= 0 && if\ \rho = 3n. \end{aligned} \tag{2.15}$$

with $n = 0, 2, 4, ..., \infty$.

At steady state operation, with an angular speed of the rotor ω ($\vartheta_r = \omega t$), the flux density in each T^{th} tooth varies in the time according to the following equation:

$$\begin{aligned} B_T = &\sum_{\rho=1}^{\infty} K_{PM\rho} cos(\rho(\omega t - \vartheta_T)) - \\ &- \sum_{n=0}^{\infty} K_{S,[3n+1]} i_q sin(\omega t - [3n+1]\vartheta_T) - \\ &- \sum_{n=2}^{\infty} K_{S,[3n-1]} i_q sin(\omega t + [3n-1]\vartheta_T). \end{aligned} \tag{2.16}$$

From the first term of (2.16) it is possible to note that the magnets generate in each tooth infinite time harmonics (at angular frequency $\rho\omega$). These present the same amplitude in each tooth and they are shifted with a fixed time delay $dt = \frac{\vartheta_T}{\omega}$. Therefore, the behaviour of the teeth is completely symmetrical in time.

Instead, the flux density contribution produced by the currents to each tooth is composed by a sum of sinusoidal terms all at the same angular frequency (ω). In this case, each component presents a time delay, from one tooth to the consecutive one, which depends on the field harmonic order (space harmonic): $dt = \pm\frac{\rho\vartheta_T}{\omega}$.

Therefore, the resulting flux density component is sinusoidal at angular frequency (ω), but it presents a different magnitude and phase depending on the considered tooth. It is worth to note that under the assumption of sinusoidally distributed winding (i.e., sinusoidal flux distribution of the armature field in the air-gap), the latter phenomenon does not appear, and (2.16) can be simplified as:

$$B_T = \sum_{\rho=1}^{\infty} K_{PM\rho} cos(\rho(\omega t - \vartheta_T)) - K_{S,1} sin(\omega t - \vartheta_T). \tag{2.17}$$

This highlights that the asymmetrical distribution of flux density in the stator teeth is due to the higher order harmonics of the armature field.

In Fig. 2.3 the expected waveforms of the flux density produced by the magnets and the stator currents are shown, respectively, for three consecutive teeth when the machine has $q > 1$ (in this case $q = 3$). The corresponding Fourier spectrum is given in Fig. 2.4 in terms of time harmonics with respect to the fundamental, with the current and magnet contributions.

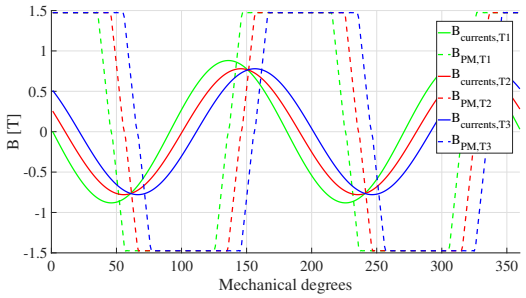

Figure 2.3: Analytical flux density evaluation in the centre of three consecutive stator teeth, as a function of the rotor mechanical position $\vartheta_r/p = 0 : 360$, for 3 slot per pole and per phase $q = 3$. The stator and rotor contributions are considered separately.

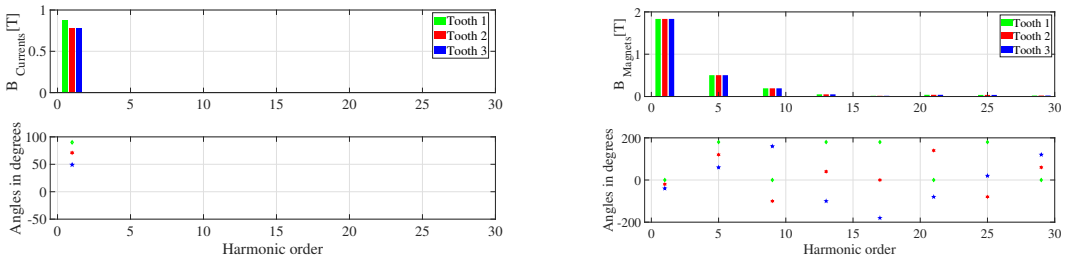

Figure 2.4: Analytical evaluation of the time FFT for the stator (top) and rotor (bottom) contributions to the flux density in three consecutive teeth for a three slot per pole and per phase machine $q = 3$).

While the contribution of each permanent magnet spatial field harmonic generates a different time harmonic, the ones produced by the stator result in flux density components at the fundamental frequency.

The analytical model, allows to decouple the effect of each stator harmonic contribution generated at the air-gap, by (2.13) and (2.15), as shown in Fig. 2.5.

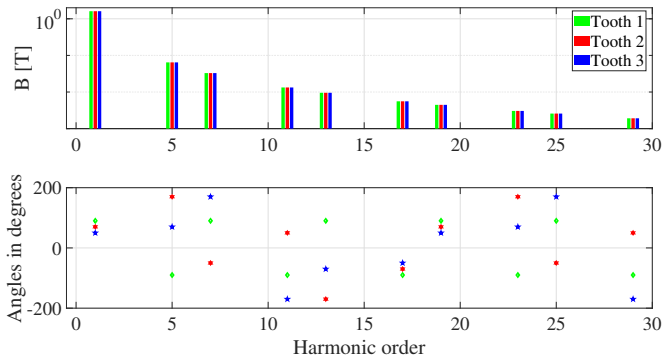

Figure 2.5: Analytical evaluation of the contributions, due to different armature space harmonics generated at the air-gap, to the stator flux density in three consecutive teeth for a machine with 3 slots per pole and per phase $q = 3$. The sum of all the contributions (with same frequency and different phase angles) generates the result provided in Fig. 2.4 (top).

The same analyses are carried out for a machine with one slot per pole and per phase ($q = 1$): in Fig. 2.6, flux density waveforms by currents and magnets are shown, respectively. Fig. 2.7 displays the corresponding Fourier spectra and Fig. 2.8 shows the stator spatial harmonic contributions.

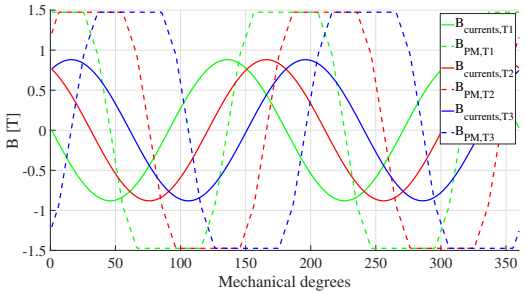

Figure 2.6: Analytical flux density evaluation in the centre of three consecutive stator teeth, as a function of the rotor mechanical position $\vartheta_r/p = 0 : 360$, for 1 slot per pole and per phase $q = 1$. The stator and rotor contributions are considered separately.

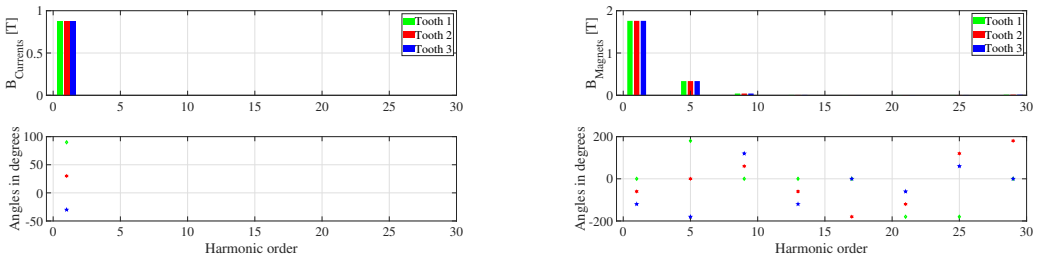

Figure 2.7: Analytical evaluation of the time FFT for the stator (top) and rotor (bottom) contributions to the flux density in three consecutive teeth for a three slot per pole and per phase machine $q = 1$).

As expected from the analytical model, the only case with the harmonic contributions equally shifted among the teeth is for $q = 1$. The angular phase shift of the flux density in one tooth caused by the ρ^{th} space harmonic ($\rho\vartheta_T$) can be rewritten considering that ρ is equal to $3n \pm 1$, with n an even number ($n = 2k$) and $N_{slot} = 6pq$.

Therefore, it is possible to re-write the angular phase shift as follows:

$$\begin{aligned} \rho\vartheta_T &= \rho\frac{2\pi p}{N_{slots}}(T-1) = (3n \pm 1)\frac{2\pi p}{6pq}(T-1) = \\ &= (6k \pm 1)\frac{2\pi}{6q}(T-1) = \\ &= \frac{2\pi k}{q}(T-1) \pm \frac{2\pi}{6q}(T-1), \quad k = 0, 1, 2, ..., \infty. \end{aligned} \tag{2.18}$$

It can be seen that the first term in (2.18) is a multiple of 2π only when $q = 1$, while the second term does not depend from the considered space harmonic. It results that $q = 1$ is the only solution for which the phase shift is not affected by the harmonic order. It is worth to notice that the phenomenon of the asymmetries in the flux density distribution are not present in a saturated machine. Indeed, the iron saturation gives a "natural" balance to the flux density waveforms in which the magnetic dipoles are all oriented so that for increased

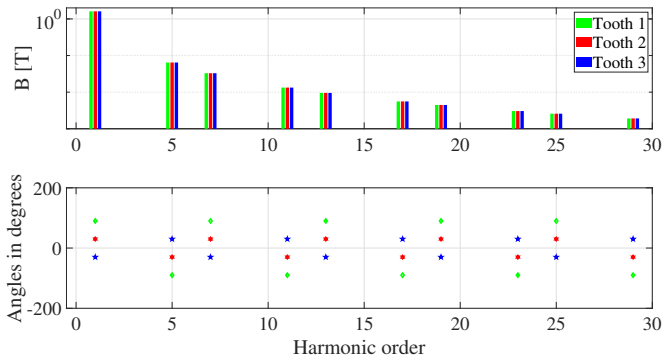

Figure 2.8: Analytical evaluation of the contributions, due to different armature space harmonics generated at the air-gap, to the stator flux density in three consecutive teeth for a machine with 1 slot per pole and per phase $q = 1$. The sum of all the contributions (with same frequency and equal, or opposite, phase angles) generates the result provided in Fig. 2.7 (top).

current values there is not an increment in the flux density amplitude. It means that in saturation working conditions the amplitudes are the same in every tooth of the stator.

2.2 Three-phase stator flux density analysis: FEA validation

In order to validate the analytical model, the obtained results have been compared with the flux density values determined by means of FEA simulations. The comparison is carried out considering only the radial component of the flux density at the centre of each tooth. This is a good approximation for the analysis of asymmetries among different teeth, neglecting local effects. To compare the FEA results with the analytical model, linear materials have been considered [50]. As a case study, two SPM machines, with $q = 3$ and $q = 1$, have been considered. The machine with $q = 1$ presents the same phases and poles of the machine with $q = 3$ but 12 slots instead 36. The two machine geometries are shown in 2.9 and 2.12 respectively.

Firstly, the 36 slots machine (with $q = 3$) is analysed. Fig. 2.10 shows the comparison

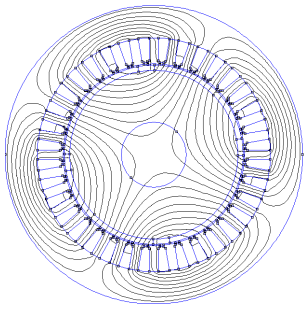

Figure 2.9: SPM machine geometry with $q = 3$.

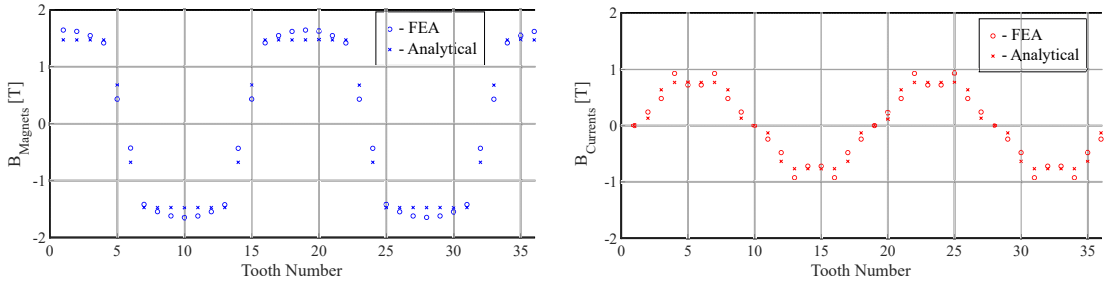

Figure 2.10: Flux density for each tooth when the rotor is aligned with the phase A ($\vartheta_r = 0$) and the stator currents are controlled to generate the rated torque for the machine with $q = 3$.

between FEA and analytical results for the flux density distribution in all the 36 stator teeth. The magnet and current contributions (presented at the left and right, respectively), when the rotor is at its initial position ($\vartheta_r = 0$), are considered separately. It is shown that the analytical model presents a good accuracy, for the considered target, with the maximum error of 56.9% (14th and 15th teeth) in the magnet contribution and by 32.3% (3rd tooth) in the current one.

Fig. 2.13 displays the same analysis proposed in Fig. 2.10 but for the machine with 12 teeth ($q = 1$), getting the maximum error between the analytical and FEA models of 15.4% (3rd tooth) in the magnet contribution and by 6.8% (5th tooth) in the current one. This displacement can be due to the fact that the analytical model works under the assumption of radial flux density at airgap and the proposed machine geometry presents a large magnetic

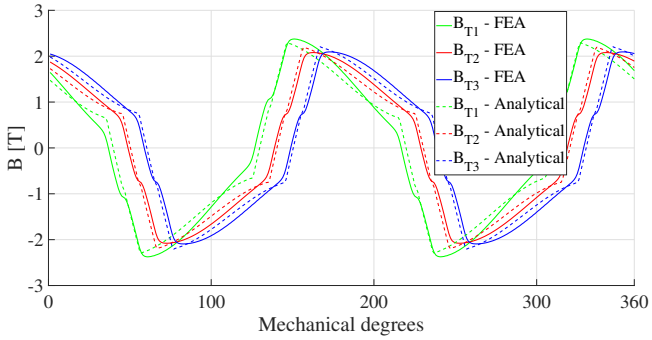

Figure 2.11: Flux density comparison for three consecutive teeth between FEA and analytical approach with $q = 3$.

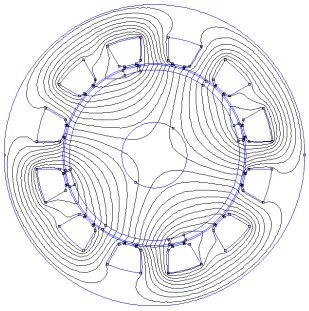

Figure 2.12: SPM machine geometry with $q = 1$.

airgap (5mm), so that there is an important tangential component of the airgap flux density which the analytical model cannot take into the account.

To compare the behaviour for all the rotor positions, Fig. 2.11 and Fig. 2.14 show the distribution of flux density in three consecutive teeth for one mechanical revolution of the rotor ($\vartheta_r = 0 : 360$), for $q = 3$ and $q = 1$, respectively. The results presented are validating the qualitative behaviour expected by the analytical model, i.e., the presence of asymmetries in the flux density distribution among the stator teeth when $q > 1$.

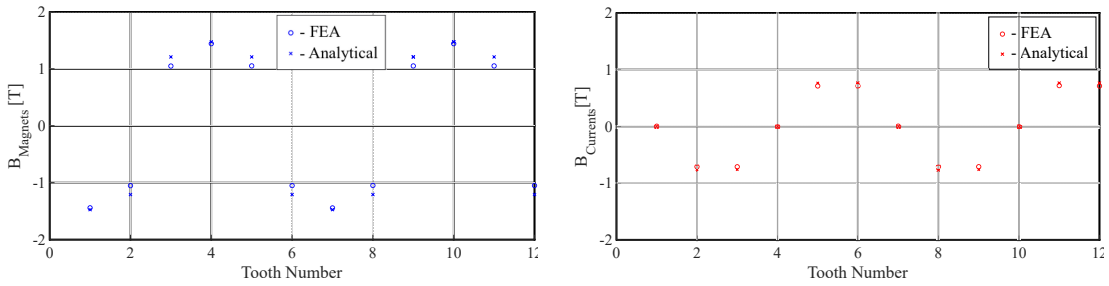

Figure 2.13: Flux density for each tooth when the rotor is aligned with the phase A ($\vartheta_r = 0$) and the stator currents are controlled to generate the rated torque for the machine with $q = 1$.

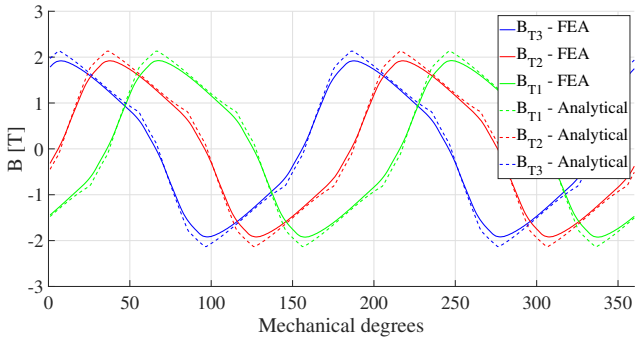

Figure 2.14: Flux density comparison for three consecutive teeth between FEA and analytical approach with $q = 1$.

2.3 Solutions to Balance the stator flux density distribution

2.3.1 Asymmetrical stator teeth design for three-phase machines

For obtaining a symmetrical flux density distribution in the stator teeth, an asymmetrical design can be implemented. The new asymmetrical geometry has been designed maintaining the same overall iron volume and same slot areas with respect to the symmetrical stator (the original one).

In order to keep the same volume of iron, the teeth thicknesses are constrained according to the following relationship:

$$w_{T1opt} + w_{T2opt} + w_{T3opt} = 3w_T. \tag{2.19}$$

Because the overall flux through one tooth does not depend from its thickness, the new flux densities can be evaluated from the equations system:

$$\begin{cases} \Phi_{T1} = B_{T1} w_T L = B_{Topt} w_{T1opt} L \\ \Phi_{T2} = B_{T2} w_T L = B_{Topt} w_{T2opt} L \\ \Phi_{T3} = B_{T3} w_T L = B_{Topt} w_{T3opt} L \end{cases} \tag{2.20}$$

where w_T and w_{Txopt} are the original and new new teeth thicknesses (with x a generic teeth number) and B_{Topt} is the optimal flux density in the new stator teeth geometry (the one reached when B is symmetrically distributed among the teeth). Combining (2.19) and (2.20) it is possible to obtain value of the symmetrical flux density distribution as:

$$B_{Topt} = \frac{B_{T1} w_T + B_{T2} w_T + B_{T3} w_T}{w_{T1opt} + w_{T2opt} + w_{T3opt}} \tag{2.21}$$

Therefore, the new teeth thicknesses are:

$$\begin{cases} w_{T1opt} = w_T + \Delta T_1 = \frac{B_{T1}}{B_{Topt}} w_T \\ w_{T2opt} = w_T + \Delta T_2 = \frac{B_{T2}}{B_{Topt}} w_T \\ w_{T3opt} = w_T + \Delta T_3 = \frac{B_{T3}}{B_{Topt}} w_T \end{cases} \tag{2.22}$$

The obtained geometry presents an important drawback: the teeth thicknesses changing affects the slot areas, increasing some and, more critical, reducing others. In order to achieve a final geometry with the same slot areas, a new geometrical parameters, ϵ_x, is introduced. The value of ϵ_x, for each xth tooth, represents the angular shift of the tooth from its original axis of symmetry. The new asymmetrical geometry is obtained by evaluating the new teeth thicknesses, and adding/subtracting the displacements (ϵ_x) that allow maintaining the same slot areas. These can be derived, for example, imposing that the width of the slots $S1$ and $S2$ are kept equal, considering for a further constraint that the average shift of the teeth is zero. These constraints are presented in the following system of equations:

$$\begin{cases} -\frac{\Delta T_1}{2} + \epsilon_1 - \frac{\Delta T_3}{2} - \epsilon_3 = 0 \\ -\frac{\Delta T_2}{2} + \epsilon_2 - \frac{\Delta T_1}{2} + \epsilon_1 = 0 \\ \epsilon_1 + \epsilon_2 + \epsilon_3 = 0 \end{cases} \tag{2.23}$$

The solution of (2.23) results in the following displacement values, function of the changes in the teeth thicknesses (given by (2.22)):

$$\begin{cases} \epsilon_1 = \frac{\Delta T_3 - \Delta T_2}{6} \\ \epsilon_2 = \frac{2\Delta T_2 + 3\Delta T_1 + \Delta T_3}{6} \\ \epsilon_3 = \frac{-2\Delta T_3 - \Delta T_2 - 3\Delta T_1}{6} \end{cases} \tag{2.24}$$

Fig. 2.15 shows a sketch of the geometrical parameters used to determine the new geometry whereas Fig. 2.16 presents the comparison between the novel asymmetrical design and the initial geometry for the considered machine case study (still considering only the armature contribution to the flux).

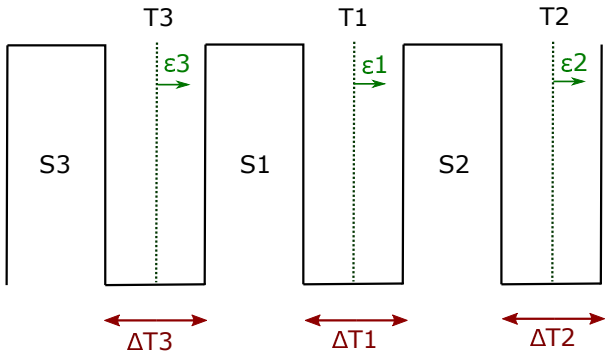

Figure 2.15: Asymmetrical geometry concept

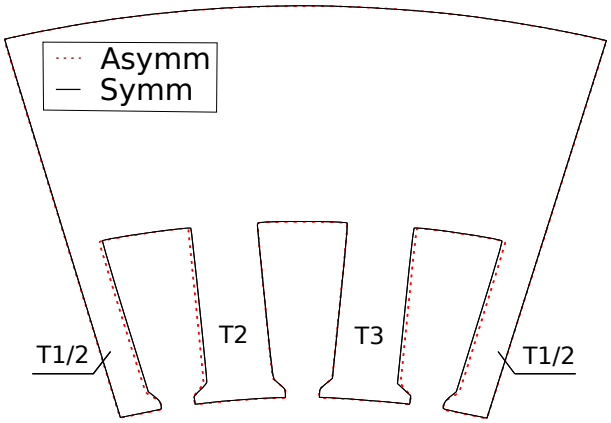

Figure 2.16: Comparison between asymmetrical and symmetrical geometry

2.3.1.1 FEA: comparison between asymmetrical and symmetrical design for a three-phase SPM machine

Finite element analysis simulations have been carried out, computing the flux density in the stator, for a case study of three-phase distributed winding SPM machine. The machine parameters are summarised in table 2.1 and the peak current in the slot is $I = 683A$. Fig. 2.17 shows the flux density distribution by stator current only, replacing PMs with iron, in the yoke for the original symmetrical and new asymmetrical machine geometries. It is possible to see that the asymmetrical geometry does not have any impacts on the yoke flux

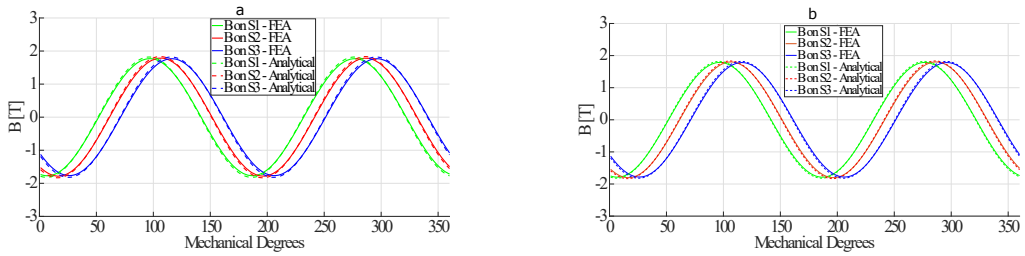

Figure 2.17: Flux density in the back iron by stator current only, replacing PMs with iron : (a) symmetrical geometry - (b) asymmetrical geometry.

density distribution which was already homogenous for the original machine geometry. The flux density in the back iron region above the yth slot Φ_y (between the two consecutive teeth T and $T-1$) is calculated analytically by:

$$\Phi_y = \Phi_{y-1} + \Phi_T. \tag{2.25}$$

The teeth asymmetries are based on the peak of flux densities when the machine works at rated current and with non linear material. The analyses are proposed for the following operating conditions: at rated current and overload condition (125 % of rated current).

A. At rated current working condition

In this current conditions the machine works almost on the B-H curve knee, corresponding to the rated operating condition (Fig. 2.18).

Fig. 2.19 shows the comparison of the flux densities in three consecutive teeth of the two geometries.

It can be noticed that the flux density distribution becomes even for the novel asymmetrical geometry. Given that the iron volume is the same, a simple approach to approximately compare the iron losses for the two geometries can be adopted. In particular, the iron losses

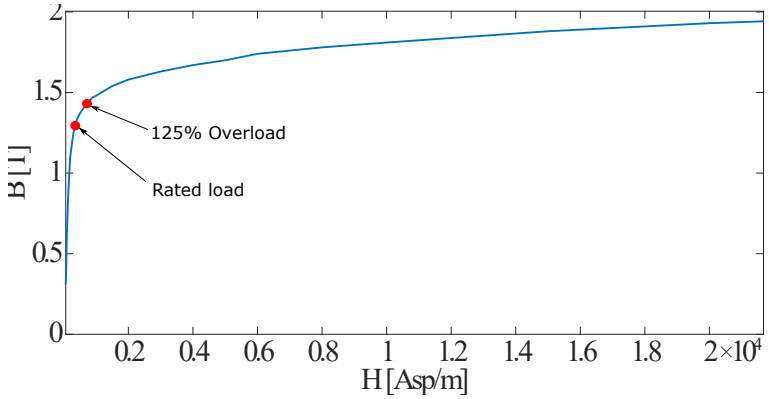

Figure 2.18: B-H curve of the lamination considered: at rated and overload current operating conditions

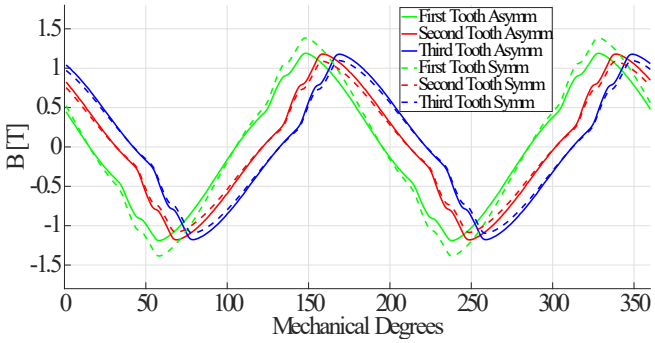

Figure 2.19: Flux density distribution in three consecutive stator at rated current operating condition

can be assumed as proportional to the square value of the flux density in the considered volume ($P_{iron} \simeq B^2$).

Therefore, the comparison on the iron losses for the two designs can be analysed from the value of the term:

$$\frac{\sum B^2_{Asymm} - \sum B^2_{Symm}}{\sum B^2_{Symm}}. \tag{2.26}$$

Table 2.2: Flux densities and torque at rated current

Parameters	Symmetrical	Asymmetrical
$B_{T1,peak}$ [T]	1.38	1.19
$B_{T2,peak}$ [T]	1.09	1.19
$B_{T3,peak}$ [T]	1.09	1.19
$\sum B_T^2$ [T]	4.21	4.18
Average Torque [Nm]	65.00	65.09
Ripple Torque [%]	12.68	12.60

From the simulation results, the evaluated iron losses in the teeth are expected to decrease of 0.71 % by means of an asymmetrical stator design.

In addition, an uniform distribution of flux density in the teeth is not affecting the torque and torque ripple performance (Fig. 2.20).

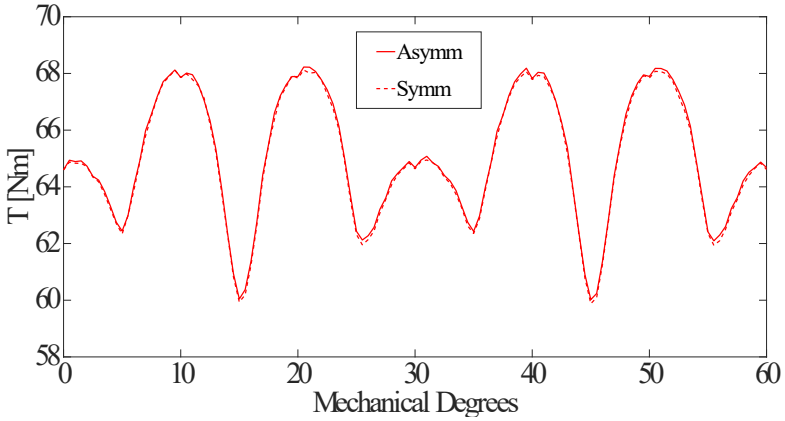

Figure 2.20: Torque ripple at rated working operation with non-linear material

In table 2.2, the comparison between symmetrical and asymmetrical geometry is summarised.

Table 2.3: Flux densities and torque at overload condition

Parameters	Symmetrical	Asymmetrical
$B_{T1,peak}$ [T]	1.58	1.39
$B_{T2,peak}$ [T]	1.25	1.35
$B_{T3,peak}$ [T]	1.26	1.35
$\sum B_T^2$ [T]	5.65	5.68
Average Torque [Nm]	81.13	81.18
Ripple Torque [%]	12.79	12.10

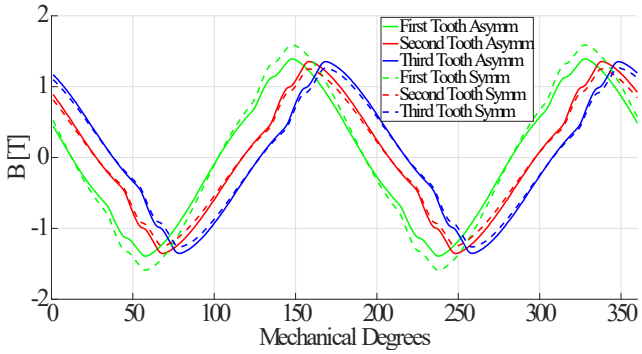

Figure 2.21: Flux density distribution in three consecutive stator at 125% of rated current operating condition

B. At overload working condition

In this operating condition the machine works on the saturation knee (Fig. 2.18), corresponding to an overload of 125%, and the simulations results are shown in Fig. 2.21. The asymmetrical design still presents an almost perfect symmetrical flux density distribution whereas the original one is asymmetrical as demonstrated in the initial analysis. Considering that the machine operates with more flux density than the rated scenario and the working point is not fully saturated, the differences in terms of percentage of iron losses reduction is slightly higher.

Indeed, applying (2.26) the iron losses are 1.24 % less for asymmetrical geometry compared to the original symmetrical one. Also in these working conditions, it is confirmed that an

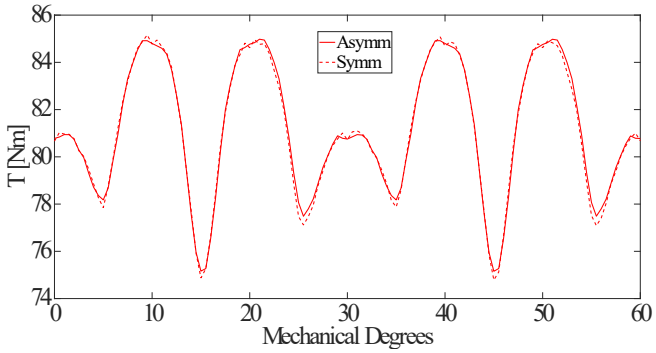

Figure 2.22: Torque ripple at overload working operation with non-linear material

even flux density density distribution in the teeth is not significantly affecting the torque (Fig. 2.22). In table 2.3, the results are summarized. Further analyses on the flux density distribution for higher overload conditions have been conducted showing that the flux density peaks will be more uniform for all teeth. However, the advantages of the proposed geometry are not completely eliminated when the machine saturates, because the asymmetrical layout allows to minimise the drop of magneto-motive force in the most saturated areas, allowing for a slight increase of the average output torque.

2.3.2 Multi phase approach: nine-phase winding arrangement

Passing from a classical three-phase distributed winding layout to a multi-phase one, the flux density in the stator teeth is balanced thanks to the fact that the slots number per pole and phase is $q = 1$. Based on the parameters of the proposed SPM machine (table 2.1), the multi-phase winding layout is a triple three-phase asymmetrical configuration with a shift angle between the phases of the same subsystem of $\frac{2\pi}{3}$ and a shift angle between the two subsystems of $\frac{\pi}{9}$ as it is shown in Fig. 2.23. The analyses is carried out via FEA,

under assumption of linear material. The stator teeth flux density comparison between the three-phase winding layout and the triple three-phase one is shown in Fig. 2.24.

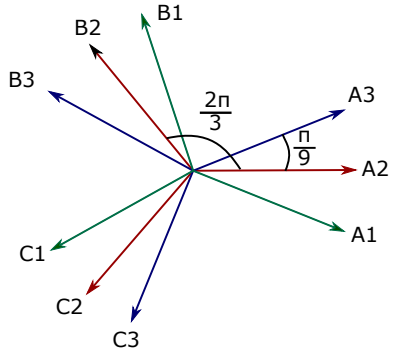

Figure 2.23: Asymmetrical 3x3-phase winding configuration

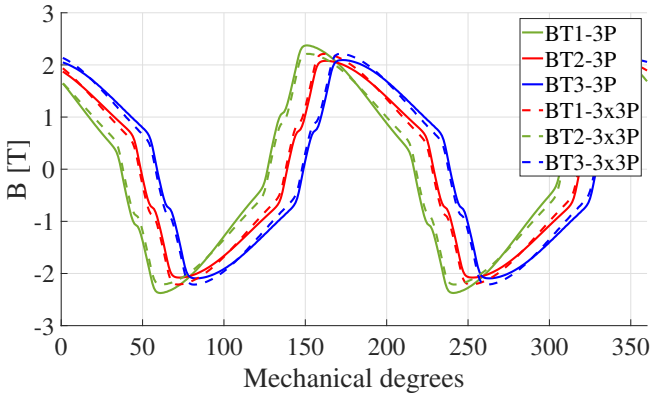

Figure 2.24: Flux density comparison for three consecutive teeth between 3-phase and 3x3-phase winding layouts.

From Fig. 2.24 is clear that the flux density is balanced in every tooth of the machine for the multi-phase configuration and in consequence the iron saturation is the same in each part of the core. Following the same approach proposed in 2.3.1.1, considering the iron losses proportional to the squared of peak flux density in the considered tooth $P_{iron} \simeq B^2$, it is possible to understand if there are benefits in terms of iron losses reduction with the

Table 2.4: Flux densities and torque 3P vs 3x3P

Parameters	3-phase	3x3-phase
$B_{T1,peak}$ [T]	2.375	2.212
$B_{T2,peak}$ [T]	2.067	2.212
$B_{T3,peak}$ [T]	2.094	2.212
$\sum B_T^2$ [T]	14.30	13.48

proposed multi phase approach by:

$$\frac{\sum B_{9P}^2 - \sum B_{3P}^2}{\sum B_{3P}^2}. \tag{2.27}$$

The results are summarised in the table 2.4, which shows that the flux density asymmetries in the stator core does not affect strongly the machine iron losses.

2.4 Conclusion

In this chapter, a detailed investigation of the flux density distribution in the teeth of an SPM machine has been carried out via analytical and FEA. The results highlight that in a three-phase machine with distributed winding the flux density distribution is not symmetrical when the number of slots per pole and per phase is higher than one ($q > 1$). This aspect can be taken into account in the early stage of the machine design, when simplified analytical models are used to predict the initial electrical machine geometrical parameters. In particular, the presented model can be used to predict the effects of these parameters on the asymmetrical distribution of iron losses and saturation, which are related to the tooth flux density. The behaviour, expected by the simplified analytical model, has been validated against FEA results for two examples of SPM machines with different numbers of slots per pole and per phase: $q = 3$ and $q = 1$. It is found that the flux density in different

teeth is asymmetrical for a machine with $q = 3$, while it is symmetrical for a machine with $q = 1$. The proposed analytical model cannot predict in an accurate way the flux density distribution when the machine is working on the B-H curve knee or in the saturation zone.

Based on the flux density analysis in the stator teeth, a novel asymmetrical design approach is proposed. The method aims to improve the efficiency of electrical machines, reducing their energy losses and obtaining the same saturation in each machine stator tooth. The stator can be modified accordingly in order to balance the flux densities and reduce the magneto-motive force drop in the stator iron. The FEA results confirmed that with the new asymmetrical geometry it is possible to reduce slightly the iron losses without affecting the output torque and the torque ripple. From a manufacturing point of view the conventional methodology can be used because the bidimensional sheet does not change in comparison to the traditional one with the same tolerances and constrains on the fittings. However, the geometry modifications are very small so that the differences could be within the sheet cutting tolerances. Moreover, the proposed analytical method for obtaining a balanced flux density in the stator teeth, proposing an asymmetrical geometry, calculates the optimum parameters for a selected operation point of the B-H curve. It means that if the machine current changes for any reasons, the stator flux density balancing cannot be guaranteed.

Finally, the multi phase approach is proposed in order to balance the flux density asymmetries in the stator teeth which deals with a homogenous saturation in every parts of the core. It can be obtained without modifying the machine geometry.

Chapter 3

Torque Analysis for Three and Multi Three-Phase Distributed Windings

This chapter highlights the advantages of the multi phase concept in terms of ripple and average torque. Indeed, the torque is due by an interaction between the Magneto-Motive Force generated by stator (MMF_S) (i.e., by the current flowing in the phases) and the MMF generated by rotor (MMF_R). In addition, the space harmonic spectra is analysed for different temporal harmonic of currents for understanding its behaviour for different phase configurations.

3.1 Magneto-motive force analysis for three and multi three-phase windings

In this chapter, it is reported the MMFs generated by a symmetrical multi phase system composed by m phases which are fed by a symmetrical set of currents $\sum_{x=1}^{m} i_x = 0$ and shifted each other by an angle of $\frac{2\pi p}{m}$ with p the pole pairs number. The MMFs can be calculated as in 3.1:

$$MMF_S(\vec{i}, \lambda) = \vec{N}(\lambda)^T \vec{i}, \tag{3.1}$$

where $\vec{N}$ is a vector which represents the winding functions for each phase and λ is the spatial coordinate in the static reference frame. The winding function and current vectors are expressed in 3.2 and 3.3 respectively.

$$\vec{N}(\lambda) = \begin{bmatrix} \vdots \\ \sum_{\rho=0}^{\infty} N_\rho cos(\rho p\lambda - \frac{2\pi p\rho}{m} x - \lambda)] \\ \vdots \end{bmatrix} \tag{3.2}$$

$$\vec{i}(\lambda) = \begin{bmatrix} \vdots \\ \sum_{\tau=0}^{\infty} I_\tau cos(\tau\omega_{el} t - \frac{2\pi p\rho}{m} x - \psi)] \\ \vdots \end{bmatrix} \tag{3.3}$$

Substituting 3.2 and 3.3 in 3.1:

$$\begin{aligned} MMF_S(\vec{i}, \lambda) = \sum_{x=1}^{m} \sum_{\rho=0}^{\infty} \sum_{\tau=0}^{\infty} N_\rho I_\tau \{ cos(np\lambda - \frac{2\pi p\rho}{m} x - \lambda) \\ cos(q\omega_{el} t - \frac{2\pi p\rho}{m} x - \lambda)\} \end{aligned} \tag{3.4}$$

Using the Eulero's formula (3.5):

$$cos(A)cos(B) = \frac{cos(A+B) + cos(A-B)}{2} \tag{3.5}$$

the 3.4 can be rearranged in the following way:

$$\begin{aligned} MMF_S(\vec{i},\lambda) = &\sum_{x=1}^{m}\sum_{\rho=0}^{\infty}\sum_{\tau=0}^{\infty}\frac{N_\rho I_\tau}{2}\{ \\ &cos(np\lambda+\omega_{el}t\tau-\frac{2\pi p\rho}{m}x-\frac{2\pi p\tau}{m}x-\lambda-\psi)+ \\ &cos(np\lambda+\omega_{el}t\tau-\frac{2\pi p\rho}{m}x+\frac{2\pi p\tau}{m}x-\lambda+\psi)\} \end{aligned} \tag{3.6}$$

$$\begin{aligned} MMF_S(\vec{i},\lambda) = &\sum_{x=1}^{m}\sum_{\rho=0}^{\infty}\sum_{\tau=0}^{\infty}\frac{N_\rho I_\tau}{2}\{ \\ &cos(np\lambda+\omega_{el}t\tau-\frac{2\pi p(h+\tau)}{m}x-\lambda-\psi)+ \\ &cos(np\lambda-\omega_{el}t\tau-\frac{2\pi p(h-\tau)}{m}x-\lambda-\psi)\} \end{aligned} \tag{3.7}$$

$$\begin{aligned} MMF_S(\vec{i},\lambda) = &\sum_{\rho=0}^{\infty}\sum_{\tau=0}^{\infty}\frac{N_\rho I_\tau}{2}Re\{ \\ &e^{(np\lambda+\omega_{el}t\tau+\lambda_\rho-\psi)}\sum_{x=1}^{m}e^{-j\frac{2\pi p(\rho+\tau)}{m}x}+ \\ &e^{(np\lambda-\omega_{el}t\tau-\lambda_\rho+\psi)}\sum_{x=1}^{m}e^{-j\frac{2\pi p(\rho-\tau)}{m}x}\} \end{aligned} \tag{3.8}$$

From the previous equations, it is possible to notice that for each current temporal harmonic τ there is a spectra of spatial harmonics ρ. With this formulations, it is possible to calculate analytically which harmonics order will be present in different winding configurations (three or multi-phase) for different injected temporal current harmonic components. Some spatial harmonics present the same rotating direction of the fundamental component (direct) while others the opposite direction (inverse).

In Table 3.1 are summarized the inverse and direct MMFs spatial harmonics until the 19^{th} and the current temporal harmonics until the 13^{th} for a classical three-phase system.

The six-phase arrangement is obtained as a sum of two 3-phase subsystems, with a shift of

Table 3.1: Magneto-motive force spatial harmonics spectrum generated by different temporal current harmonics for a three-phase system

-	$\tau=1$	$\tau=3$	$\tau=5$	$\tau=7$	$\tau=9$	$\tau=11$	$\tau=13$
$\rho=1$	$\omega_{el}t$	0	$-5\omega_{el}t$	$7\omega_{el}t$	0	$-11\omega_{el}t$	$13\omega_{el}t$
$\rho=3$	0	$3\omega_{el}t$ and $-3\omega_{el}t$	0	0	$9\omega_{el}t$ and $-9\omega_{el}t$	0	0
$\rho=5$	$-\omega_{el}t$	0	$5\omega_{el}t$	$-7\omega_{el}t$	0	$11\omega_{el}t$	$-13\omega_{el}t$
$\rho=7$	$\omega_{el}t$	0	$-5\omega_{el}t$	$7\omega_{el}t$	0	$-11\omega_{el}t$	$13\omega_{el}t$
$\rho=9$	0	$3\omega_{el}t$ and $-3\omega_{el}t$	0	0	$9\omega_{el}t$ and $-9\omega_{el}t$	0	0
$\rho=11$	$-\omega_{el}t$	0	$5\omega_{el}t$	$-7\omega_{el}t$	0	$11\omega_{el}t$	$-13\omega_{el}t$
$\rho=13$	$\omega_{el}t$	0	$-5\omega_{el}t$	$7\omega_{el}t$	0	$-11\omega_{el}t$	$13\omega_{el}t$
$\rho=15$	0	$3\omega_{el}t$ and $-3\omega_{el}t$	0	0	$9\omega_{el}t$ and $-9\omega_{el}t$	0	0
$\rho=17$	$-\omega_{el}t$	0	$5\omega_{el}t$	$-7\omega_{el}t$	0	$11\omega_{el}t$	$-13\omega_{el}t$
$\rho=19$	$\omega_{el}t$	0	$-5\omega_{el}t$	$7\omega_{el}t$	0	$-11\omega_{el}t$	$13\omega_{el}t$

$\frac{\pi}{6}$ radians between them:

$$\vec{i_1}(\lambda) = \begin{bmatrix} \vdots \\ \sum_{\tau=0}^{\infty} I_\tau cos(\tau\omega_{el}t - \frac{2\pi p\rho}{m}x - \psi)] \\ \vdots \end{bmatrix} \tag{3.9}$$

$$\vec{i_2}(\lambda) = \begin{bmatrix} \vdots \\ \sum_{\tau=0}^{\infty} I_\tau cos(\tau\omega_{el}t - \frac{2\pi p\rho}{m}x + \frac{\pi}{6} - \psi)] \\ \vdots \end{bmatrix} \tag{3.10}$$

Therefore, the (3.8) can be re-written as following:

$$\begin{aligned} MMF_S(\vec{i},\lambda) = &\sum_{\rho=0}^{\infty}\sum_{\tau=0}^{\infty}\frac{N_\rho I_\tau}{2}Re\{ \\ &e^{(np\lambda+\omega_{el}t\tau+\lambda_\rho-\psi)}\sum_{x=1}^{3}e^{-j\frac{2\pi p(\rho+\tau)}{3}x} + \sum_{x=1}^{3}e^{-j(\frac{2\pi p(\rho+\tau)}{3}+\frac{\pi}{6})x} \\ &e^{(np\lambda-\omega_{el}t\tau-\lambda_\rho+\psi)}\sum_{x=1}^{3}e^{-j\frac{2\pi p(\rho-\tau)}{3}x} + \sum_{x=1}^{3}e^{-j(\frac{2\pi p(\rho-\tau)}{3}+\frac{\pi}{6})x}\} \end{aligned} \tag{3.11}$$

Table 3.2: Magneto-motive force spatial harmonics spectra generated by different temporal current harmonics for a dual three-phase system

-	$\tau = 1$	$\tau = 3$	$\tau = 5$	$\tau = 7$	$\tau = 9$	$\tau = 11$	$\tau = 13$
$\rho = 1$	$\omega_{el}t$	0	0	0	0	$-11\omega_{el}t$	$13\omega_{el}t$
$\rho = 3$	0	$3\omega_{el}t$	0	0	$-9\omega_{el}t$	0	0
$\rho = 5$	0	0	$5\omega_{el}t$	$-7\omega_{el}t$	0	0	0
$\rho = 7$	0	0	$-5\omega_{el}t$	$7\omega_{el}t$	0	0	0
$\rho = 9$	0	$-3\omega_{el}t$	0	0	$9\omega elt$	0	0
$\rho = 11$	$-\omega_{el}t$	0	0	0	0	$11\omega_{el}t$	$-13\omega_{el}t$
$\rho = 13$	$\omega_{el}t$	0	0	0	0	$-11\omega_{el}t$	$13\omega_{el}t$
$\rho = 15$	0	$3\omega_{el}t$	0	0	$-9\omega_{el}t$	0	0
$\rho = 17$	$-\omega_{el}t$	0	$5\omega_{el}t$	$-7\omega_{el}t$	0	0	0
$\rho = 19$	$\omega_{el}t$	0	$-5\omega_{el}t$	$7\omega_{el}t$	0	0	0

The harmonic spectra for this configuration is shown in Table 3.2.

The MMFs harmonic spectra for a triple three-phase system is displayed in Table 3.3.

Analysing the proposed results, it is possible to notice that the MMFs presents more spatial components when the machine is arranged with the classical three-phase winding layout with respect to the multi-phase ones for each current temporal harmonic. In particular, higher is the number of phases, lower are the spatial components in the harmonic spectra. This behaviour has repercussions on the ripple torque as it will be shown in the next section.

Table 3.3: Magneto-motive force spatial harmonics generated by different temporal current harmonics for a nine-phase system

-	$\tau = 1$	$\tau = 3$	$\tau = 5$	$\tau = 7$	$\tau = 9$	$\tau = 11$	$\tau = 13$
$\rho = 1$	$\omega_{el}t$	0	0	0	0	0	0
$\rho = 3$	0	$3\omega_{el}t$	0	0	0	0	0
$\rho = 5$	0	0	$5\omega_{el}t$	0	0	0	$-13\omega_{el}t$
$\rho = 7$	0	0	0	$7\omega_{el}t$	0	$-11\omega_{el}t$	0
$\rho = 9$	0	0	0	0	$9\omega_{el}t$ and $-9\omega_{el}t$	0	0
$\rho = 11$	0	0	0	$-7\omega_{el}t$	0	$11\omega_{el}t$	0
$\rho = 13$	0	0	$-5\omega_{el}t$	0	0	0	$13\omega_{el}t$
$\rho = 15$	0	$-3\omega_{el}t$	0	0	0	0	0
$\rho = 17$	$-\omega_{el}t$	0	0	0	0	0	0
$\rho = 19$	$\omega_{el}t$	0	0	0	0	0	0

3.2 Torque Ripple Analysis

The torque of an electrical machine is produced by the interaction between the magneto-motive force spatial harmonics of stator and rotor. When the same spatial harmonic presents the same speed, the harmonic interaction generates DC torque (average) whereas if the speed is different the interaction generates an AC torque (ripple).

A general torque relation can be written as:

$$T = -\frac{\partial W}{\partial \Delta}, \tag{3.12}$$

where W is the magnetic field energy at the air-gap and Δ is the periphery angle in radians, circumscribed by the rotor with respect to the stator. Under hypothesis of an uniform air-gap the torque can be written as:

$$T = -\frac{l\delta}{2\mu_0}\frac{\partial}{\partial \Delta}\int_0^{2\pi}[B(\lambda, t)]^2 d\lambda. \tag{3.13}$$

The magnetic flux density can be written as:

$$B(\lambda, t) = \frac{\mu_0}{\delta} F(\lambda, t) \tag{3.14}$$

where $F(\lambda, t) = MMF_S(\lambda, t) + MMF_R(\lambda, t)$ is the magneto-motive force at the air-gap given by the sum of stator and rotor contributions.

Substituting 3.14 in 3.13, the torque can be re-written as:

$$T = -\frac{l\delta}{2\mu_0} \frac{\partial}{\partial \Delta} \int_0^{2\pi} [\frac{\mu_0}{\delta}(MMF_S(\lambda, t) + MMF_R(\lambda, t))]^2 d\lambda \tag{3.15}$$

Based on the rotor layout, different MMF_R amplitudes and spatial spectra are generated. The hypothesis is that a generic rotor generates the following MMF_R spatial components: 1^{st} 3^{rd}, 5^{th}, 7^{th}, 9^{th}, 11^{th}, 13^{th} 15^{th} 17^{th} 19^{th}. In the following part of this section, the three-phase, dual three-phase and triple three-phase winding arrangements supplied with a fundamental current only, taking into the account the spatial harmonics until the 19^{th}, are analysed. The analysis shows which harmonics interaction generates DC torque and which AC torque without to take into the account their amplitudes.

In the classical three-phase winding configuration, supplied with the only fundamental current component, the AC torque presents the sixth, twelfth and eighteenth harmonics as shown below:

- 1^{st} rotor harmonic + 1^{st} stator harmonic $\rightarrow \omega_{el}t$ - $\omega_{el}t \rightarrow T_1$ (Constant)

- 5^{th} rotor harmonic + 5^{st} stator harmonic $\rightarrow 5\omega_{el}t + \omega_{el}t \rightarrow T_6$

- 7^{th} rotor harmonic + 7^{st} stator harmonic $\rightarrow 7\omega_{el}t$ - $\omega_{el}t \rightarrow T_6$

- 11^{th} rotor harmonic + 11^{st} stator harmonic $\rightarrow 11\omega_{el}t + \omega_{el}t \rightarrow T_{12}$

- 13^{th} rotor harmonic + 13^{st} stator harmonic $\rightarrow 13\omega_{el}t$ - $\omega_{el}t \rightarrow T_{12}$

- 17^{th} rotor harmonic + 17^{st} stator harmonic $\rightarrow 17\omega_{el}t + \omega_{el}t \rightarrow T_{18}$

- 19^{th} rotor harmonic + 19^{st} stator harmonic $\rightarrow 19\omega_{el}t$ - $\omega_{el}t \rightarrow T_{18}$

In contrast, the dual three-phase configuration, in the same current conditions, does not present the sixth harmonic of torque because it does not generates the fifth and seventh magneto-motive force harmonics by stator. Therefore, the torque components are:

- 1^{st} rotor harmonic + 1^{st} stator harmonic $\rightarrow \omega_{el}t$ - $\omega_{el}t \rightarrow T_1$ (Constant)

- 11^{th} rotor harmonic + 11^{st} stator harmonic $\rightarrow 11\omega_{el}t + \omega_{el}t \rightarrow T_{12}$

- 13^{th} rotor harmonic + 13^{st} stator harmonic $\rightarrow 13\omega_{el}t$ - $\omega_{el}t \rightarrow T_{12}$

- 17^{th} rotor harmonic + 17^{st} stator harmonic $\rightarrow 17\omega_{el}t + \omega_{el}t \rightarrow T_{18}$

- 19^{th} rotor harmonic + 19^{st} stator harmonic $\rightarrow 19\omega_{el}t$ - $\omega_{el}t \rightarrow T_{18}$

Finally, the nine phase (i.e., triple three-phase) configuration is investigated. From the following analysis, it is clear that only the eighteenth AC torque component is present due to the MMF_s and MMF_R interaction of the seventeen and nineteen harmonics.

- 1^{st} rotor harmonic + 1^{st} stator harmonic $\rightarrow \omega_{el}t$ - $\omega_{el}t \rightarrow T_1$ (Constant)

- 17^{th} rotor harmonic + 17^{st} stator harmonic $\rightarrow 17\omega_{el}t + \omega_{el}t \rightarrow T_{18}$

- 19^{th} rotor harmonic + 19^{st} stator harmonic $\rightarrow 19\omega_{el}t$ - $\omega_{el}t \rightarrow T_{18}$

3.3 Advantages of multi-phase systems in terms of improved torque performance

This section presents a case study of machine analysis, aiming at highlighting the enhancement in the performance that can be reached transitioning from a three-phase system to a multiple three-phase one. The electrical machine adopted in this system is a 4 pole pairs IPM machine with a V-Shape rotor layout, as shown in Fig. 3.1. The main advantages of this machine are high torque density and an extended power range capability over the base speed (namely flux weakening region). A summary of the machine parameters is given in Table 3.4. The following analysis is mainly focused on torque and efficiency performance considering two different winding layouts: a conventional three-phase distributed winding and a dual three-phase one.

In order to simulate the machine with a FEA software, a work of reverse engineering is adopted, measuring the machine parameters from the prototype available in the electrical

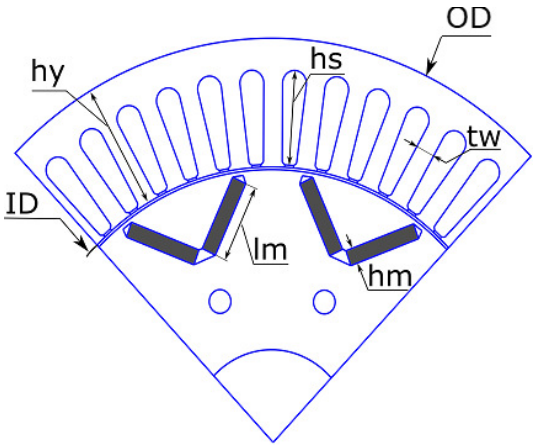

Figure 3.1: V-shape IPM machine sketch.

machines laboratory. In particular, the geometrical parameters are measured by a caliper and the magnet flux by a flux meter. In order to validate the FEA model obtained from the measured parameters, the obtained BEMF is compared with the experimental one, showing good accuracy (Fig. 3.2).

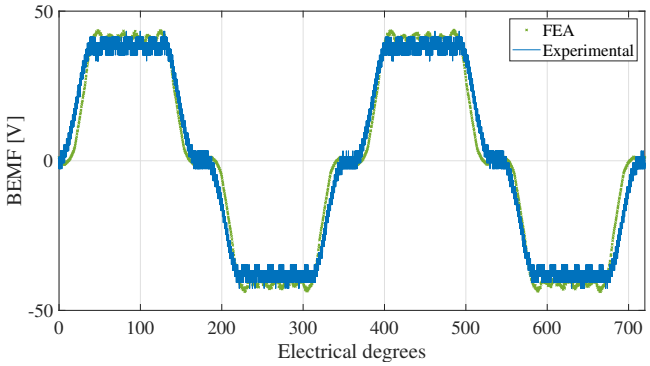

Figure 3.2: Back Electro-Motive Force (BEMF) comparison between finite element and experimental analyses at 1500 rpm for the proposed V-Shape IPM machine.

The experimental BEMF has been obtained to drive the IPM machine at 1500 rpm by an induction machine coupled with it.

Table 3.4: Machine parameters

Parameters	Values	Units
Pole pairs (p)	4	-
Slots number (Q)	48	-
Winding turns (nc)	8	-
Length steak (L_{stk})	110.0	mm
Outer stator diameter (OD)	203.0	mm
Inner stator diameter (ID)	138.0	mm
Slot height (h_s)	25.07	mm
Back iron height (h_y)	33.1	mm
Tooth width (t_w)	5.2	mm
Airgap (g)	0.7	mm
Magnet length (l_m)	20.0	mm
Magnet height (h_m)	4.0	mm

The IPM machine prototype under study presents a skewed rotor of a quarter slot (1.875 mechanical degrees). In order to take this aspect under consideration, two different 2D FEA simulations are carried out. The first one is set with the rotor shifted by -1.875 mechanical degrees with respect to the phase A whereas the second one with a shift of +1.875 mechanical degrees. The final BEMF waveform is obtained by the combination of these two waveforms.

3.3.1 Torque analysis

A multi-phase design can give significant benefits in terms of ripple and average torque. Indeed, the control strategy of a multi-phase machine can be extended to the control of some high order space harmonics of the airgap magnetic field [**?**]. In addition, the winding factor is higher compared to a three-phase winding [51], leading to a higher average torque.

In this section, both torque and torque ripple have been carried out by means of finite element analysis simulations, maintaining the same machine's overall volume and supply conditions. In Fig. 3.3 the torque ripple resulting from a different winding arrangement is shown for three-phase and dual three-phase distribution, respectively. The results highlight

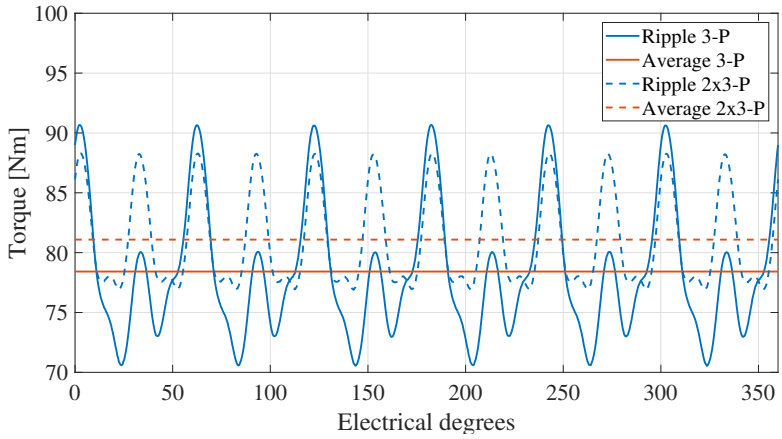

Figure 3.3: IPM machine torque comparison between three-phase and dual three-phase winding arrangements.

that the dual three-phase machine features an average torque of 81.1 Nm with respect to the 78.4 Nm of the three-phase machine, with an overall increment of +3.40%. The multi-three-phase layout reduces the torque ripple as well, confirming the analysis carried out in section 3.2. In the three-phase winding layout case the peak to peak torque ripple is 25.58%, whereas it is 13.65% for the dual three-phase one, leading to an overall reduction of the oscillations by 11.93%, with respect to the three-phase machine.

3.3.2 Losses analysis

In literature, many researchers have been working on the estimation of the iron losses with analytical and FEA models. In [52], an accurate prediction of iron losses for various frequen-

cies and magnetic flux densities, considering the influence of higher order time harmonics and minor loops, is presented. In [53], an improved model of the iron losses for an induction machine based on a comparison of different equations has been developed. The influence of the pulse width modulation (PWM) generated by inverter on machine iron losses is also described in [54]. In order to have a preliminary indication of the iron losses in the machine, the classical Steinmetz method is considered with the hypothesis of sinusoidal flux in the iron. This is used as a quantitative method for a comparative estimation of the iron losses expressed with the following equation:

$$P_{iron} = B_{peak}^2(k_{hy}f_p + k_{ed}f_p^{\alpha}) \tag{3.16}$$

where B_{peak} is the maximum value of flux density in the iron, k_{hy} and k_{ed} are the hysteresis and eddy current coefficients, respectively, f_p is the fundamental frequency and α is the Steinmetz coefficient.

However, considering a unique value of B_{peak} in the stator core does not permit to consider the asymmetrical flux density behaviour. In fact, for a three-phase machine presenting a number of slots/poles per phase $q > 1$, the flux density is not symmetrical due to high harmonic order fields generated by currents as shown in chapter 2 . In this case, another advantage introduced by the dual three-phase winding is that the number of slots/poles per phase is $q = 1$ so that the flux density results symmetrical in all stator core parts. The approach proposed takes into the account these asymmetries allowing for a better comparison between the two considered winding layouts. The iron losses in the two consecutive teeth and on two consecutive yokes at the top of each area are calculated as follows:

$$\begin{cases} P_{tooth1} = k_t P_{spec,iron}(\frac{B_{t1}}{B_{ref}})^2(k_{hy}(\frac{f_p}{f}) + k_{ed}(\frac{f_p}{f})^{\alpha})w_t \\ P_{tooth2} = k_t P_{spec,iron}(\frac{B_{t2}}{B_{ref}})^2(k_{hy}(\frac{f_p}{f}) + k_{ed}(\frac{f_p}{f})^{\alpha})w_t \\ P_{yoke1} = k_y P_{spec,iron}(\frac{B_{y1}}{B_{ref}})^2(k_{hy}(\frac{f_p}{f}) + k_{ed}(\frac{f_p}{f})^{\alpha})w_y \\ P_{yoke2} = k_y P_{spec,iron}(\frac{B_{y2}}{B_{ref}})^2(k_{hy}(\frac{f_p}{f}) + k_{ed}(\frac{f_p}{f})^{\alpha})w_y \end{cases} \tag{3.17}$$

where $P_{spec,iron}$ takes into the account the specific iron losses in the core, while k_t, k_y, B_t, B_y, w_t and w_y are the correction coefficients, peak flux density values and weights related to the teeth and the volumes of back iron around the slots, respectively; f is the reference frequency (50 Hz) and B_{ref} is the reference flux density (1 T) for the iron losses calculation.

The weight of a single tooth w_t is calculated as:

$$w_t = \gamma_{iron} h_s t_w L_{stk}, \tag{3.18}$$

where $\gamma_{iron} = 7800 kg/m^3$ is the specific weight of the used iron.

The weight of one part of the considered back iron w_y is calculated as:

$$w_y = \gamma_{iron} \pi (OD - h_{bi}) h_{bi} L_{stk}, \tag{3.19}$$

where $h_{bi} = OD/2 - ID/2 - h_s$.

Table 3.5 lists the parameters used for the FEA simulations.

Finally, it is possible to obtain the total iron losses in the stator by applying the following equation:

$$P_{iron,stator} = \frac{Qs}{2}(P_{tooth1} + P_{tooth2} + P_{yoke1} + P_{yoke2}), \tag{3.20}$$

where Qs is the total number of teeth of the machine.

Table 3.6 summaries the results obtained from the comparison of the two different winding arrangements. It is worth to highlight that, albeit the local saturation in the teeth of the dual three-phase machine is more balanced, the overall stator iron losses are not significantly affected by the winding configuration.

Table 3.5: Simulation parameters used for the iron losses analysis

Parameters	Value
$P_{spec,iron}$ [W/kg]	2.30
k_{hy}	0.70
k_{ed}	0.30
$f[Hz]$	50
$B_{ref}[T]$	1
$f_p[Hz]$	100
α	2
k_t	2
k_y	1.5
w_t	0.12
w_y	0.08

3.3.3 Efficiency

The mechanical and rotor losses are neglected for simplicity in this qualitative evaluation exercise, as their contribution will only add an equal offset in the quantities of both analysed machines. The Joule losses have been calculated implementing the classical equation, considering the DC component only due to the low frequency of the system, function of the resistance R and phase current I_{RMS} squared. Therefore, after the mentioned hypothesis, the efficiency can be calculated as:

$$\eta = \frac{T_{avg}\omega_m}{T_{avg}\omega_m + P_{iron,stator} + P_j}, \tag{3.21}$$

where T_{avg} is the average torque and ω_m is the rotor mechanical pulsation corresponding to the machine rated speed.

Table 3.6: Iron losses comparison results

Parameters	3-phase	2x3-phase
B_{t1} [T]	1.77	1.77
B_{t2} [T]	1.75	1.77
B_{y1} [T]	1.94	1.88
B_{y2} [T]	1.84	1.88
$P_{iron,stator}$ [W]	337	338

Table 3.7: Winding configurations comparative analysis

Parameters	3-phase	2x3-phase	Units
I_{peak}	71.25	71.25	A
P_j	39.10	39.10	W
$P_{iron,stator}$	337	338	W
P_{tot}	365	364	W
ω_m	157.08	157.08	rad/s
T_{avg}	78.4	81.1	Nm
P_{out}	12.32	12.74	kW
η	97.12%	97.22%	-

3.3.4 Results comparison

In this subsection, a summary of the compared results between three-phase and dual three-phase systems is given, as reported in Table 3.7. It is worth to highlight that for the same current loading in the machine slots, the mechanical output power is higher with a multi-phase configuration (+3.4%), and consequently showing an improved torque capability. If the application is demanding a minimization of the volume, the machine can produce the same torque with the same current load and reduced volume.

Indeed, the torque is proportional to the stack length of the machine, consequently the active stack length for the multi-phase machine can be reduced from $l_{3P} = 110.0mm$ (the active stack length of the three-phase machine) to $l_{2x3P} = 106.3mm$. This can lead to a weight reduction from 32.3 kg to 31.2 kg if a multi-phase winding is adopted. Therefore, for the same phase current and output torque, the multi-phase machine will result 1.10 kg lighter (about 3.4%). Furthermore, also the efficiency results to be slightly increased (about 0.10%) compared to the three-phase winding solution.

3.4 Conclusion

In this chapter, analytical MMF_s and torque ripple investigation, considering a generic rotor which produces the only odd harmonics until the 19^{th}, are carried out for different distributed winding arrangements (three-phase, dual three-phase and triple three-phase). From the analysis, it is clear that the multi phase approach gives benefits in terms of torque ripple with respect to the classical three-phase one due to the fact that some magneto-motive force non-fundamental spatial harmonics are not generated. In addition, the multi-phase approach gives better performance in terms of average torque also. It is shown for an IPM machine with a V-shape rotor configuration which passing from the classical three-phase system to the dual three-phase one presents an improved torque by 3.40% thanks to an improved fundamental winding factor which passes from 0.9659 to 1. For the proposed machine, the torque ripple is lower by 11.93% for the multi-phase system with respect to the three-phase one.

Alternatively, keeping the same average torque and passing from a three-phase arrangement to a dual three-phase one, it is possible to reduce the machine overall volume (i.e., machine weight) or the input RMS current (i.e, machine Joule losses).

The main drawback of the multi-phase machines is the increased amount of power electronic components in the electric drive. It means that the system presents higher fault probability. Indeed, the intrinsic benefit in terms of fault-tolerance due to the multi-phase winding layouts clashes with the sensibility of the electronic components which present statistically higher probability to have failures with respect to the electromechanical devices. However, with suitable control algorithms, the drive probability fault can be often reduced (e.g., open phase faults with fault tolerant control algorithms).

Chapter 4

Harmonic Injection Technique to Keep the Peak Current Constant for Surface Permanent Magnet Machines

In this chapter, the multi-phase approach and current harmonic injection technique are proposed for a dual rotor SPM machine. In particular, the study focuses on how the third current harmonic injection technique, at peak current constant, can influence the performance of a dual rotor machine with fractional slots and Halbach array for E-Bike [55] which was originally designed with a classical three-phase winding arrangement.

4.1 Preliminary analyses and current harmonic injection equations

4.1.1 Dual rotor machine characteristics

The dual rotor machine under investigation presents a Halbach configuration rotor and a stator with Fractional Slots Concentrated Windings (FSCW). The main machine parameters are: 24 slots, 14 pole pairs and a fundamental frequency of 2100 Hz. The geometry is shown in Fig. 4.1. The multi phase winding layout is designed in order to allow a phase shift current control for improving the torque capability.

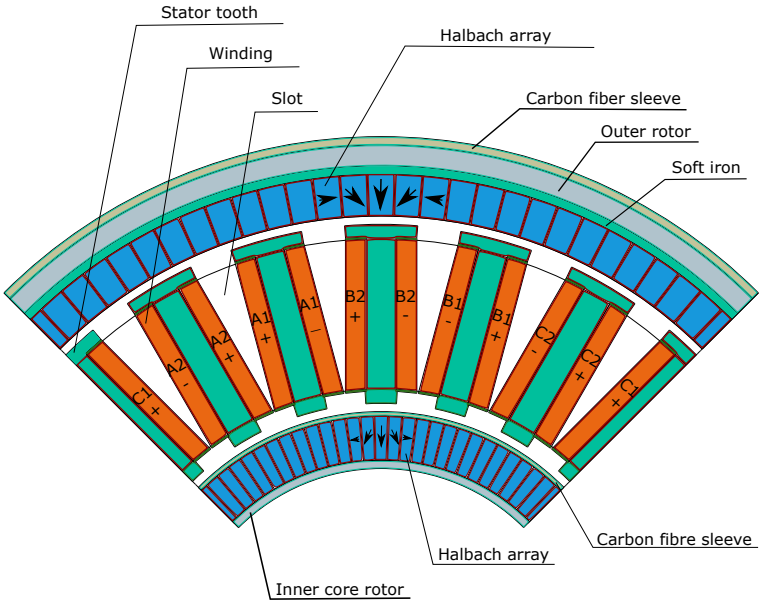

Figure 4.1: Dual rotor machine sketch and winding configuration.

4.1.2 BEMF at base angular speed

In this work, the asymmetrical dual three-phase solution with a shift of 30 electrical degrees between the two different sets is adopted. This solution increases the machine torque capability, provided that the currents of both sets are controlled properly.

In Fig. 4.2, a BEMFs comparison, carried out by means of Finite Element Analysis, between three-phase and multi-phase configurations with linear material is given. The choice to set linear materials for the simulation is due to get the BEMF waveforms generated by PM oriented with a Halbach layout avoiding the saturation effects.

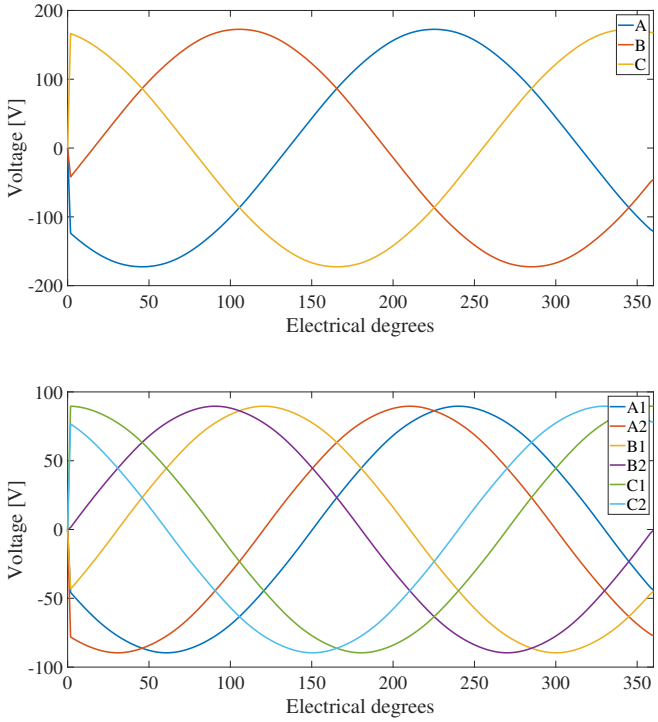

Figure 4.2: SPM dual rotor: back electro-motive forces for 3-phase and 2x3-phase with linear material by FEA.

In order to have a complete BEMFs analysis, the waveforms with non-linear material are carried out and proposed in Fig. 4.2 for both winding configurations.

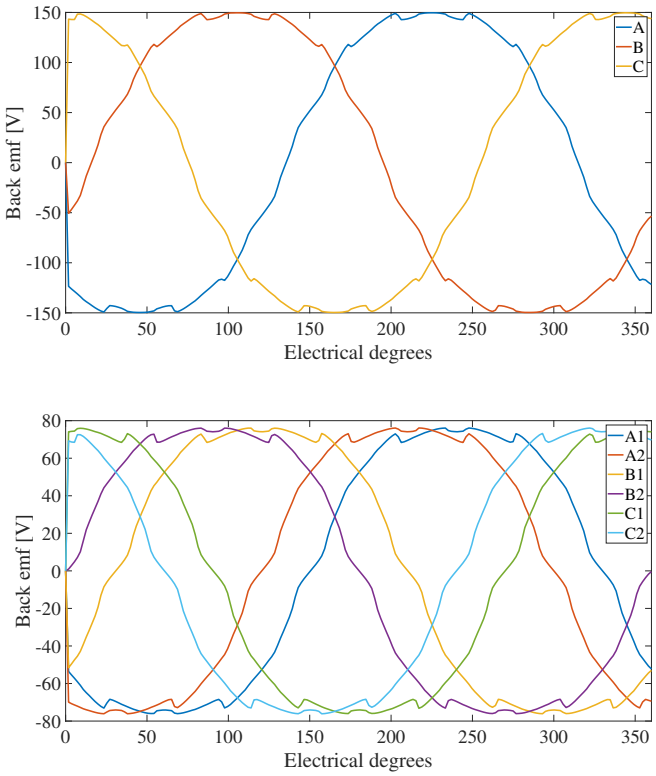

Figure 4.3: SPM dual rotor: back electro-motive forces for 3-phase and 2x3-phase with no-linear material by FEA.

From the results, It is possible to see that in non-linear material configuration the BEMFs are not perfectly sinusoidal due to the core saturation.

The linear BEMFs are taking into the account for the calculation of the third harmonic amplitude for the injection whereas the torque comparison with and without injection will be presented for the no-linear material.

The BEMFs for dual three-phase system shows the 30 electrical degrees shift between the same phase for the two different set of windings. In this motor, the Maximum Torque Per Ampere (MTPA) is achieved when the phase currents are aligned with the respective BEMFs because the d-axis reactance is equal to the q-axis one ($X_d = X_q$). This corresponds to have both the three-phase subsystems operating with only their quadrature component of the currents. Thus, the currents have to be injected without shift with respect to the their own phase BEMF. Fig. 4.4 shows the current vector diagram for this configuration.

It is worth noticing that for the dual three-phase configuration, the BEMF amplitude is half compared to three-phase one for the same number of turns per coil.

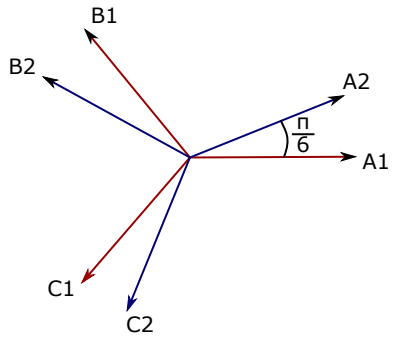

Figure 4.4: Asymmetrical 2x3-phase winding configuration.

4.1.3 Third current harmonic injection

The third current harmonic generated by the inverter can be used to improve the average torque output. The proposed dual rotor with Halbach permanent magnet array presents a sinusoidal BEMFs (theoretically, considering linear material) so that the third harmonic component is not present as shown in Fig. 4.5.

In [26], it is shown how to increase the torque performance by injecting the third harmonic

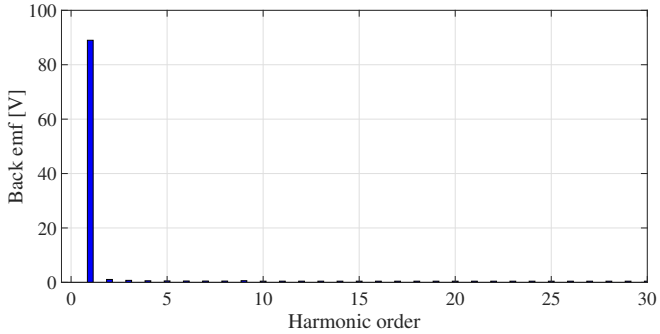

Figure 4.5: One phase FFT back electro-motive force of the dual three-phase arrangement considering linear material.

without the third harmonic BEMF presence and working on the inverter only. The third current harmonic injection allows to reduce the current peak by 15%, with respect to the fundamental only. Thus, it is possible to increase the current value, without exceeding the inverter current limit (Fig. 4.6). In this way, the peak current is constant but its RMS value is higher, therefore it leads to higher thermal loading.

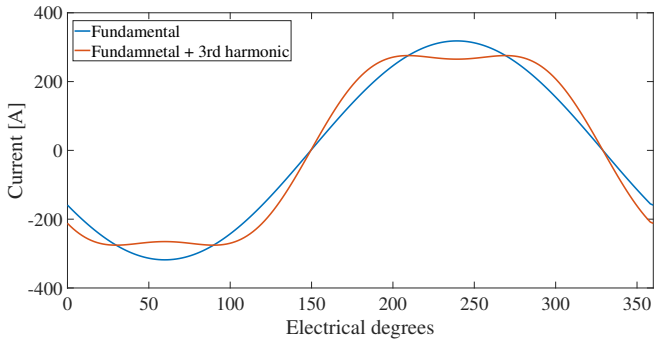

Figure 4.6: SPM dual rotor: phase current waveforms with and without 3rd current harmonic injection.

To have a more general understanding of the injection technique, the evaluation of the machine behaviour is carried out neglecting the non-linear behaviour of the ferromagnetic

materials.

4.1.4 Equations

This subsection shows the main equations for the third harmonic injection for a dual three-phase machine. The equations are derived in [26] and reported below.

The machine fundamental current is expressed as:

$$i_\theta = I_p sin(p\theta), \tag{4.1}$$

considering the third harmonic injection the current becomes:

$$i_\theta = I_{new}[sin(p\theta) + A_3 sin(3p\theta)], \tag{4.2}$$

where I_p is the peak phase current, I_{new} is the new peak phase current of the first harmonic component once the third harmonic is injected and A_3 is the amplitude of the third harmonic with respect to the fundamental one. The peak current can be calculated equating to zero the derivative of $i(\theta)$ with respect to θ:

$$\frac{di_\theta}{d\theta} = I_p p[cos(p\theta) + 3A_3 cos(3p\theta)] = 0, \tag{4.3}$$

The optimum current amplitude can be obtained in two conditions:

$$\begin{cases} cos(p\theta) = 0, 0 < A_3 \leq \frac{1}{9} \\ cos(p\theta) = \sqrt{\frac{9A_3 - 1}{12A_3}}, A_3 > \frac{1}{9} \end{cases} \tag{4.4}$$

The phase current can be explicit:

$$\begin{cases} I_p = I_{new}(1 - A_3), 0 < A_3 \leq \frac{1}{9} \\ I_p = I_{new} 8A_3 (\frac{1+3A_3}{12A_3})^{1.5}, A_3 > \frac{1}{9} \end{cases} \tag{4.5}$$

The new current $I_{new}(\theta)$ can be calculated as:

$$\begin{cases} I_{new} = \frac{I_p}{1-A_3}, 0 < A_3 \leq \frac{1}{9} \\ I_{new} = \frac{1}{8A_3}(\frac{1+3A_3}{12A_3})^{-1.5} I_p, A_3 > \frac{1}{9} \end{cases} \tag{4.6}$$

The torque for a general dual-three phase machine, once the third current harmonic is injected, can be written as:

$$T = 6RlN[B_1 k_{w1} i_{new} + A_3 B_3 k_{w3} i_{new}], \tag{4.7}$$

with m phases number, R inner stator radius, l active machine stack length, N turns number per phase, B_1 and B_3 the flux density amplitudes for the first and third harmonic, respectively. k_{w1} and k_{w3} are the winding factors for the first and third harmonic, respectively.

1) For the case $0 < A_3 \leq \frac{1}{9}$ the torque (4.7) can be re-arranged in the following way:

$$T = 6RlN\frac{I_p}{1-A_3}[B_1 k_{w1} + A_3 B_3 k_{w3}], \tag{4.8}$$

the maximum torque value is determined when the third harmonic current amplitude, with respect to the fundamental one, is:

$$A_3 = \frac{1}{9}, \tag{4.9}$$

Therefore, the new current becomes:

$$I_{new} = I_p \frac{9}{8}. \tag{4.10}$$

2) For the case $A_3 > \frac{1}{9}$ it is possible to get the best amplitude coefficient in order to increase the torque (4.7) applying Lagrange:

$$\frac{dL(I_{new}, A_3)}{dI_{new}} = 0; \frac{dL(I_{new}, A_3)}{dA_3} = 0. \tag{4.11}$$

The new current and amplitude third harmonic coefficient with respect to the fundamental one for $A_3 > \frac{1}{9}$ are:

$$A_3 = \frac{1}{6 - 3\frac{E_3}{E_1}}. \tag{4.12}$$

$$I_{new} = \frac{6 - 3\frac{B_3}{B_1}\frac{kw_3}{kw_1}}{8}\left(\frac{3 - \frac{B_3}{B_1}\frac{kw_3}{kw_1}}{4}\right)^{-1.5} I_p. \tag{4.13}$$

where E_1 and E_3 are the first and the third harmonic BEMF amplitudes, respectively.

In the proposed case of study, the BEMFs ratio $\frac{E_3}{E_1}$ is almost zero.

Therefore, the optimum amplitude of third harmonic component of current is $\frac{1}{6}$ with respect to the fundamental one. This amplitude is applied also for the three-phase machine analyses.

4.2 Finite Element Analyses

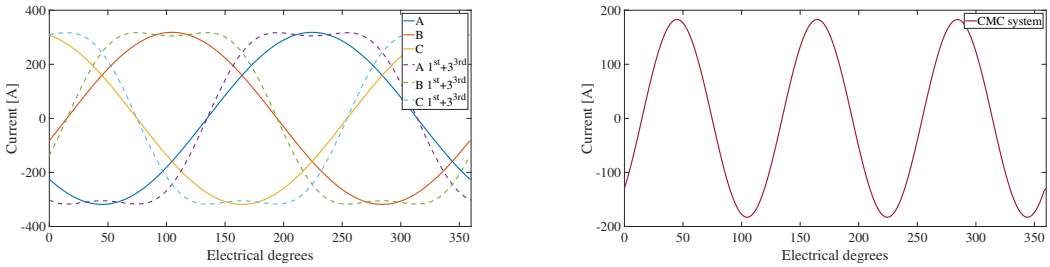

Figure 4.7: SPM dual rotor: phase currents for the three-phase arrangement with and without injection and its Common Mode Current (CMC).

In this section, a comparison of the machine performance between three-phase and dual three-phase, with and without third current harmonic injection, is carried out by means of FEA simulations. While subsection 4.1 is based on the assumption of linear material behaviour, the FEA results section takes into the account the non-linearities of the ferromagnetic materials (i.e., the iron saturation).

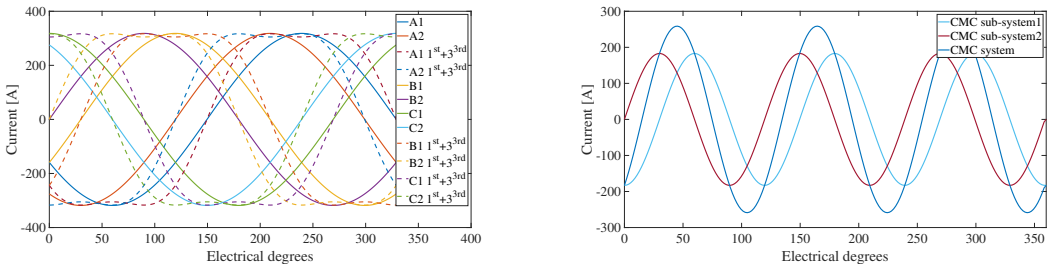

Figure 4.8: SPM dual rotor: phase currents for the dual three-phase arrangement with and without injection and its Common Mode Current (CMC).

The optimum amplitude of the third current harmonic for the proposed machine, considering non-saturation in the material, is 1/6 of the fundamental because the third harmonic BEMF is not present (see equation (4.12)).

The phase current waveforms, with and without harmonic injection, are displayed in Fig. 4.7 and Fig. 4.8, where also the common mode currents (CMC) of both three-phase and dual three-phase systems are highlighted, respectively.

4.2.1 Analysis with only fundamental current component

1. Torque

In Fig. 4.9, the torque is shown for both three-phase and dual three-phase systems. The average torque is higher for the multi-phase solution due to an improved winding factor as mentioned in chapter 3-section 3.3.1, already.

The dual three-phase system gives an important benefit also in terms of torque ripple which decreases from 4.5 % to 0.84 %. Indeed, the dual three-phase arrangement does not generate the torque sixth harmonic component and the first harmonic component higher than the

fundamental is the twelfth.

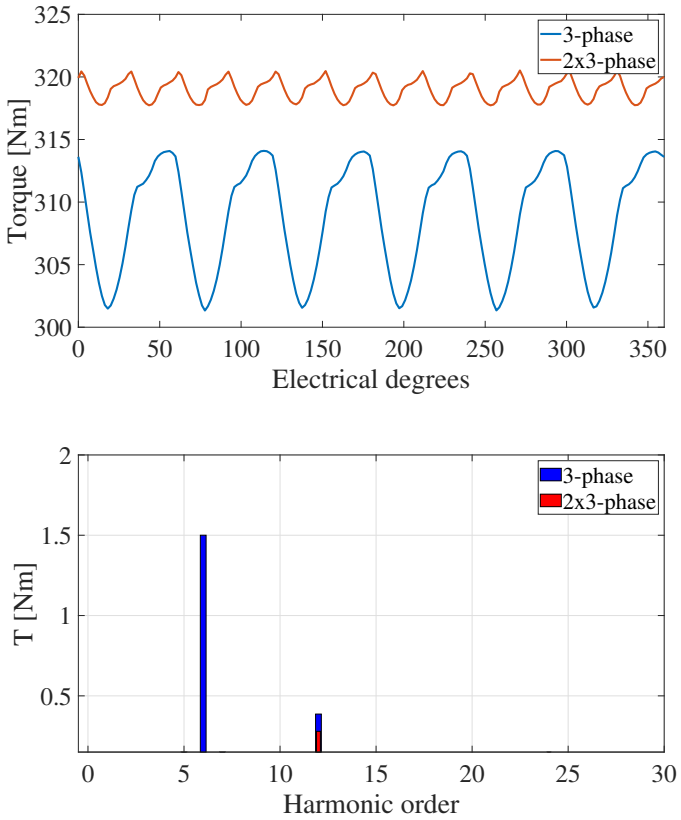

Figure 4.9: SPM dual rotor: torque ripple waveforms for 3-phase and 2x3-phase arrangement and corresponding FFT.

2. Efficiency

For the same configurations, the efficiency is calculated at the base angular speed ω_m with

the following formula:

$$\eta = \frac{Poutput}{Poutput + Losses}100 = \frac{T\omega_m}{T\omega_m + Losses}100, \tag{4.14}$$

where T is the average torque and ω_m is the angular base speed in expressed rad/s. Table 4.2 summarises the losses and machine efficiency obtained from the FEA results. The losses are similar for the two systems so that the efficiency results higher for dual three-phase configuration due to an higher output power.

4.2.2 Analysis with third current temporal harmonic component

1. Torque

Fig. 4.10 shows the torque for both systems when the third current harmonic injection is applied. Both configurations present a higher torque compared to the control technique without third current harmonic injection due to higher current flowing into the machine. In this operating condition, the ripple is slightly higher compared to the solution without third current harmonic injection. Actually, the ripple is higher by 0.51 % for the three-phase arrangement whereas by 0.30 % for the dual three-phase one. This phenomenon is due to the fact that the three-phase MMFs harmonic spectra presents more components than the dual three-phase one. This is true even more in presence of third current harmonic injection (Table 3.1 and Table 3.2). While, the average torque presents a similar improvement for both winding solutions.

2. Efficiency

The Joule losses AC component is taken into the account for a better understanding of the third harmonic injection impact in the machine. The iron losses are slightly higher with respect to the solution without third current injection whereas the Joule losses are increased

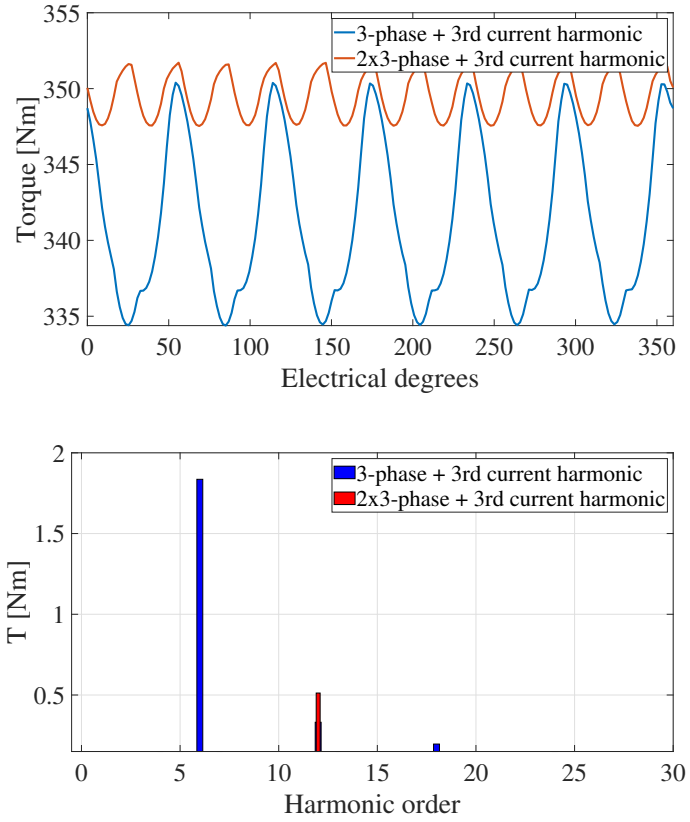

Figure 4.10: SPM dual rotor: torque ripple waveforms for 3-phase and 2x3-phase arrangement with harmonic injection and corresponding FFT.

significantly. In large part, it is due to the fact that more current is fed to the machine (Table 4.2). However, the efficiency results similar due to the higher output torque and considering the hypothesis that the machine is continuing to work at rated speed. This can be a good solution when an overload drive capability is required without exceeding the inverter current limit.

Table 4.1: Torque ripple and current

Parameters	3-phase	2x3-phase
Input RMS current [A]	224.55	224.55
Input peak current [A]	318.18	318.18
Average torque [Nm]	307.85	319.05
Torque ripple [%]	4.16	0.84
	3-phase + 3rd	2x3-phase + 3rd
Input RMS current [A]	262.65	262.65
Input peak current [A]	318.18	318.18
Average torque [Nm]	342.4	349.6
Torque ripple [%]	4.67	1.14

Table 4.2: Performance comparison between 3-phase and 2x3-phase arrangement with and without current harmonic injection

Parameters	3-phase	2x3-phase
Iron losses [W]	1427	1420
Joule losses [W]	3857	3857
Average torque [Nm]	307.85	319.05
Efficiency [%]	98.21	98.60
	3-phase + 3rd	2x3-phase + 3rd
Iron losses [W]	1460	1476
Joule losses [W]	5358	5358
Average torque [Nm]	342.4	349.6
Efficiency [%]	97.94	97.97

4.2.3 Torque comparison for the three-phase and dual three-phase systems with and without injection

The torque improvements due to the third current harmonic injection which are studied in the previous section 4.2.2 are summarised in this one, proposing the comparison of the two different winding layouts and studying them with and without injection. The torques with and without injection for the three-phase machine is shown in Fig. 4.11 whereas in Fig. 4.12 for the dual three-phase system. Analysing the mentioned Figs., it is possible to see a torque increment by 1.22% passing from 307.85 Nm to 342.4 Nm for the three-phase machine and by 9.57% passing from 319.05 Nm to 349.6 Nm for the dual three-phase one. Regarding the torque ripple, both configurations show that the current harmonic injection does not affect strongly this value, showing an increment due to the injection by 0.55% passing from 4.09% to 4.64% for the three-phase machine and by 0.34% passing from 0.80% to 1.14% for the dual three-phase one.

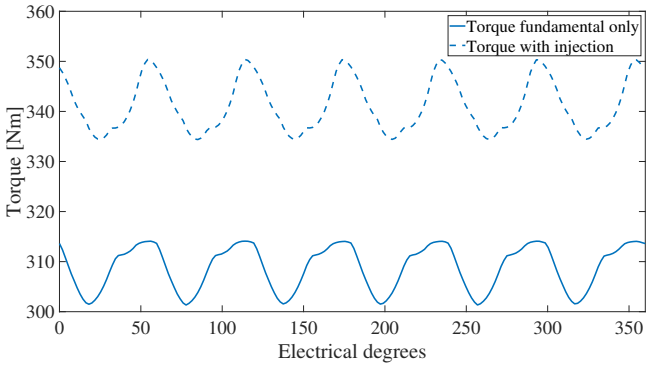

Figure 4.11: SPM dual rotor: torque comparison for the three-phase machine with and without 3rd current harmonic injection.

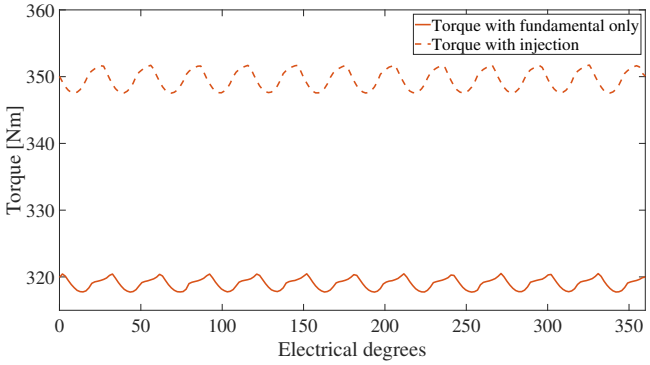

Figure 4.12: SPM dual rotor: torque comparison for the three-phase machine with and without 3rd current harmonic injection.

4.3 Conclusion

This chapter 4 analyses the torque performance and efficiency of a dual rotor E-bike machine in a three-phase and dual three-phase winding configurations with and without third harmonic injection. The aim is to identify ways of improving the torque capability. The finite element analyses show that the multi-phase system gives significant benefits in terms of both average torque and torque ripple. Actually, the average torque improves by 3.64% whereas the torque ripple decreses by 3.32%. For the proposed dual rotor machine, the third harmonic current injection can increase the average torque. In this way, it is possible to feed the machine with more current without exceeding the inverter current limit. In this operating condition, the output torque is improved. Actually, the three-phase system increases the output torque by 11.22% with third harmonic injection with respect to the solution with only fundamental current component whereas the same comparison for the dual three-phase arrangement shows that it presents an improved output torque by 9.57%. Considering the significant torque increment that the third current harmonic injection at constant peak current gives to the machine, it is plausible to imagine its applicability when the E-bike requires more torque whereas the machine should work without third current

harmonic in large part of the time to reduce the Joule losses. When the third current harmonic component is injected into the machine, it presents the common mode currents (CMC). This requires the availability of the neutral points.

Chapter 5

Permanent Magnet Reduction by Harmonics Injection Technique to Keep the RMS Constant for Multi-Phase SPM Machines with Distributed Winding

The surface permanent magnet machines are commonly used in the applications where high torque per volume is required such as aerospace, automotive and transport applications [56], [57]. For high power/torque performance, it is well known that the use of rare earth materials, such as NdFeB and SmCo, is considered the state of the art, thanks to their high magnetic coercivity and excellent temperature behaviour. However, because their high costs, it is mandatory to reduce their use in many applications.

In literature, many authors presented possible alternatives to the rare earth, including different permanent magnet topologies [58], [59]. In [60], a possible solution to replace the rare earth with ferrite for an interior permanent magnet machine is evaluated. A comparison between rare earth and rare earth-free solutions is investigated in [61]. An hybrid PM material is designed and analysed in [62].

The idea is to reduce the PM content in the machine by injecting the odd harmonics from the first to the thirteenth in a triple three-phase machine. A similar approach has been used in [32], where a nine-phase SPM machine is studied via FEA for different PM span to increase the torque performance by harmonic injection. However, the investigation is based on the injection until the seventh harmonic. The analysis is organised as follows: First, the flux density at the air-gap and back electromotive force, as a function of the PM percentage on the rotor, are carried out in a triple three-phase SPM machine for different spatial harmonics. Then, the equations for deriving the injection current amplitudes of each temporal harmonics are presented. The technique is proposed to improve the average torque, keeping the RMS constant. In the same section, the torque comparison between the machine with and without harmonics injection is carried out as a function of the rotor surface PM percentage. The analytical model results are validated via FEA. The comparison in terms of phase voltage, phase current and torque is carried out for two triple three-phase SPM machines with different PM content.

5.1 Analytical model

A simple analytical derivation is here derived for the evaluation of the machine flux density, BEMF and torque. A set of equations is also included to define the current amplitudes to maximise the torque for the same RMS value. The model works under the assumptions of linear materials and radial flux density at the airgap. The analytical model takes into the

account all odd harmonics from the fundamental to the 13^{th}. The harmonics with orders above 13th have not been considered because it has been seen that their amplitudes are low and do not have a significant impact on the torque improvement. The torque increment by current harmonic injection for SPM machines is based on the BEMF amplitudes; the higher is the ratio between the considered harmonic and the fundamental, the higher is the torque increment.

5.1.1 Flux Density and Back Electro-Motive Force

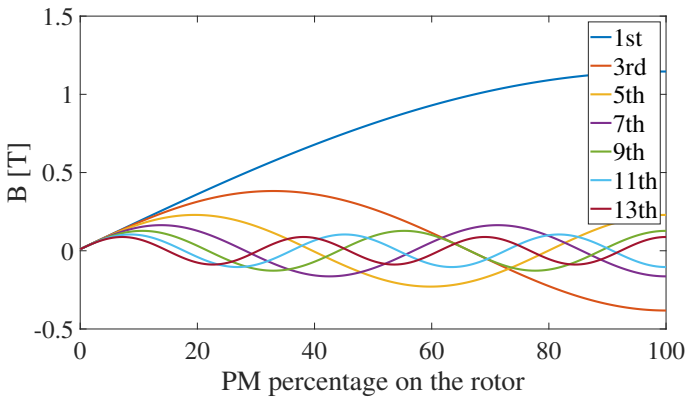

Figure 5.1: Analytical flux density evaluation at the air-gap with respect to the magnets span on the rotor surface of a SPM machine.

An electrical machine generates the torque through the interaction between rotor and stator magnetic fields. For a SPM machine, the rotor magnetic field contribution is due to the permanent magnets. The magnetic field at the air-gap generated by the rotor, in an SPM machine for ρ^{th} spatial harmonics, can be written as:

$$\bar{H}_{PM,\rho} = \frac{4B_r\delta_{PM}}{\mu_{PM}\pi\delta}\frac{sin(\rho\Delta_{PM}/2)}{\rho}e^{j\rho\vartheta_r}, \tag{5.1}$$

where B_r is the remanence flux density, δ_{PM} the magnet thickness, μ_{PM} the magnet permeability, Δ_{PM} the permanent magnet span on the rotor surface, δ the magnetic air-gap

and θ_r the rotor position in electrical radians. Considering the air magnetic permeability μ_0, it is possible to get the flux density at the air-gap from (5.1) as:

$$\bar{B}_{PM,\rho} = \mu_0 \bar{H}_{PM,\rho}. \tag{5.2}$$

When the machine rotates with a generic speed, the flux generated by the PMs is linked to the stator windings. In no load conditions (i.e., no-current in the machine), it is possible to estimate the variation of the flux in the time by means BEMF e_ρ.

The BEMF amplitude can be expressed also as a function of the machine geometrical parameters as:

$$\bar{e}_\rho = 2Rlnc\omega_m B_{PM,\rho} k_{w,\rho}, \tag{5.3}$$

where R is the stator inner radius, l is the stack length, nc is the turns per phase number, ω_m is the mechanical pulsation and $k_{w,\rho}$ is the winding factor.
The winding factor can be written as:

$$k_{w,\rho} = \frac{\sum_{y=1}^{Nc} sin(\rho \frac{\Delta\psi_y}{2}) e^{j\rho\psi_y}}{pq}, \tag{5.4}$$

where ψ_y is the angular shift from the magnetic axis of the y-th coil and the magnetic axis of the relative phase, Nc is the coils number and q the number per pole per phase.
Fig. 5.1 shows the flux density at the air-gap with respect to the PM span on the rotor Δ_{PM} for the following spatial harmonics: 1^{st}, 3^{rd}, 5^{th}, 7^{th}, 9^{th}, 11^{th}, 13^{th}. The values used for the computation of the parameters are summarised in Table 5.1.

The BEMF evaluation is shown in Fig. 5.2. It is worth to notice that the BEMF has different signs, for some harmonics, with respect to the airgap flux density. Indeed, the winding factor, for the proposed triple three-phase machine arrangement, alternates the values 1 and -1 for the different considered harmonics.

From Fig. 5.2, it is clear that the BEMF ratio, between a generic spatial harmonic and the fundamental one, changes with the PM span Δ_{PM}. For maximising the torque increment

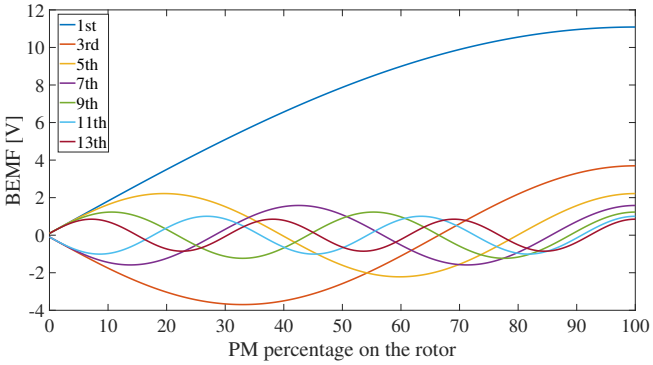

Figure 5.2: Analytical BEMF evaluation with respect to the magnets span on the rotor surface of a SPM machine.

by current harmonic injection is important to choose the maximum ratio between the harmonics that are selected for the injection and the fundamental one. Therefore, each rotor configuration has a different optimal harmonic for increasing the torque by injection.

5.1.2 Equations for current harmonics injection

It has been shown how the machine average torque can be increased by injecting current temporal harmonics higher than the fundamental, creating an interaction with the spatial harmonics of higher order, generated by rotor PMs [26]- [27].

The analytical calculation of the optimum third harmonic current amplitude to maximise the torque, keeping constant the RMS current, is derived as:

$$a_3 = \frac{e_3}{e_1}, \tag{5.5}$$

$$I^* = \frac{1}{\sqrt{1 + (\frac{e_3}{e_1})^2}} I_p, \tag{5.6}$$

where a_3 is the optimum third harmonic amplitude with respect to the fundamental, which is calculated as the ratio between the 3^{rd} and the 1^{st} BEMF harmonics. In equation (5.6)

Table 5.1: Machine parameters

Parameters	Values	Units
B_r	1.2	T
δ_{PM}	3	mm
μ_0	$4\pi * 10^{-7}$	H/m
μ_r	1	H/m
μ_{PM}	$4\pi * 10^{-7}$	H/m
δ	4	mm
g	1	mm
ω_m	157.07	rad/s
R	70	mm
l	220	mm
p	2	-
N	1	-

the I^* is the new phase current considering the injection and I_p is the phase current without injection.

In this work, the analytical equation for the current harmonic injection, keeping the same RMS, is generalised for infinite harmonics. The optimum injection current amplitude and the phase current (I^*) equations can be expressed for a generic harmonic order as:

$$a_i = \frac{e_i}{e_1}, i = 3, 5, 7, ..., \infty \tag{5.7}$$

$$I^* = \frac{I_p}{\sqrt{1 + \sum_{i=3}^{\infty} a_i^2}}, \tag{5.8}$$

Therefore, the amplitude current of each harmonics is:

$$I_1 = I^* \tag{5.9}$$

$$I_i = I^* a_i, i = 3, 5, 7, ..., \infty \tag{5.10}$$

If the torque is expressed as a function of the BEMF, it is possible to know its correlation with the Δ_{PM} variation.

The electromagnetic torque for a triple three-phase system without current harmonics injection can be written as:

$$T = \frac{9}{2}\frac{I_p e_1}{\omega_m}. \tag{5.11}$$

When the harmonics are injected, the torque can be calculated considering each contribution independently:

$$T_1 = \frac{9}{2}\frac{I_1 e_1}{\omega_m} \tag{5.12}$$

$$T_i = \frac{9}{2}\frac{I_i e_i}{\omega_m}, i = 3, 5, 7, ..., \infty \tag{5.13}$$

By combining each torque contribution, the total torque can be defined as:

$$T_{new} = T_1 + \sum_{i=3}^{\infty} T_i \tag{5.14}$$

The temporal harmonics for the current injection technique are the ones of odd order z = 2k + 1, where k = 1, 2, 3,..., ∞. In this case, the maximum order considered is 13^{th}, neglecting the higher order harmonics.

Fig. 5.3 shows the trend of torque as a function of Δ_{PM} for both fundamental only and with the injection of all considered harmonics. The phase current amplitude is $I_p = 683.7A$. It is worth to notice that the torque increment, given by the injection, is higher for all PM span Δ_{PM}. In Table 5.2, a summary of the torque increment with respect to supplying the machine with fundamental only is reported. The results are obtained analysing different points of Fig. 5.3. Even if for some cases the potential torque increment is considerable, for example when Δ_{PM} is 20% and 40% the torque can be +52.7% and +16.9% higher, these are not considered to be applicable in industrial applications. Fortunately, good torque improvements can be obtained also for high PM rotor covering. Moreover, thanks to the harmonics injection technique, it is also possible to deliver a specific torque value with a reduced amount of PMs.

Table 5.3 shows the PM reduction for different PM span percentage for a fixed torque. It is possible to get these values from Fig. 5.3 directly moving on the x axis.

Table 5.2: Torque increment by current injection

Δ_{PM}	Torque increment
20%	+52.7%
40%	+16.9%
60%	+4.9%
80%	+3.6%
100%	+9.4%

Table 5.3: PM reduction by current injection

T average	PM reduction
67 Nm	−11%
128 Nm	−10%
175 Nm	−6%
207 Nm	−6%
217 Nm	−19%

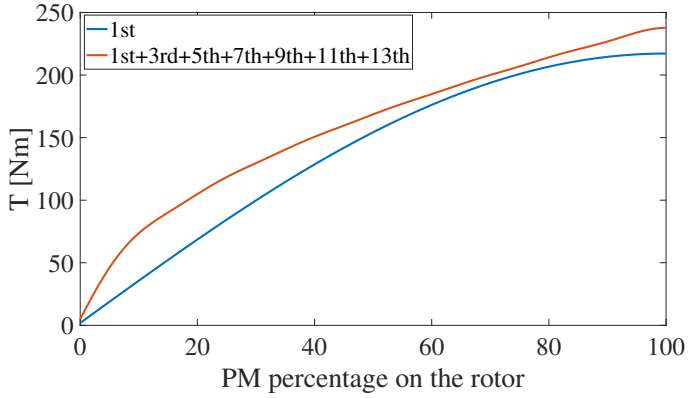

Figure 5.3: Analytical torque evaluation with and without harmonics injection with respect to the magnets span on the surface rotor of a SPM machine.

In order to have a complete understanding of the machine behaviour under the harmonics injection technique, for the same RMS current, additional analyses to investigate its influence are carried out on both current and voltage phase (section 5.2.2).

5.2 Finite Element Validation

Based on the findings shown in the previous section, the following analysis aims at demonstrating the benefits of the current injection with different harmonic components. In order to validate the analytical model, a FEA is carried out for two machines, named M1 and M2, with the same geometry and two different permanent magnet span. The Δ_{PM} in M1 is 82% while in M2 88%, which corresponds to a reduction of PM volume of 6% in M1 with respect to M2. First M1 is analysed with and without harmonics injection to show the torque increment while keeping the same RMS current. Then, this is compared against the torque performance of M2, which has higher content of PM, supplying with only the fundamental current component.

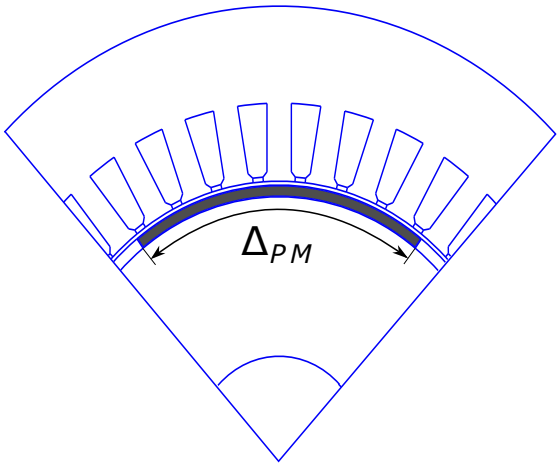

Figure 5.4: Sketch of the SPM machine under analysis.

The analyses are carried out considering linear materials. The proposed SPM machine geometry is shown in Fig. 5.4, highlighting the parameter Δ_{PM}.

5.2.1 Torque analysis

Fig. 5.5 shows the torque comparison derived by means of FEA and with the analytical formulation. Fig. 5.5(a) presents the FEA results only. For M1, it is possible to notice that the harmonics injection permits an average torque increment by 3.2% with respect to the case of fundamental current only. This is slightly higher, by 1%, with respect to the torque delivered by M2 without harmonic injection, even if the permanent magnet content is reduced by 6%. The same analysis has been carried out using the analytical model. The results are shown in Fig. 5.5(b). In this case, for M1, thanks to the harmonic injection, there is an improved torque by 3.7%. It is higher for M1, when the considered harmonics are injected, compared to M2 without injection, in accordance to the trends resulting from the FEA (5.5(a)). The increment in this case is by 1.4 %. For a clearer understanding of torque increments due to the injections, their averages are plotted separately with respect

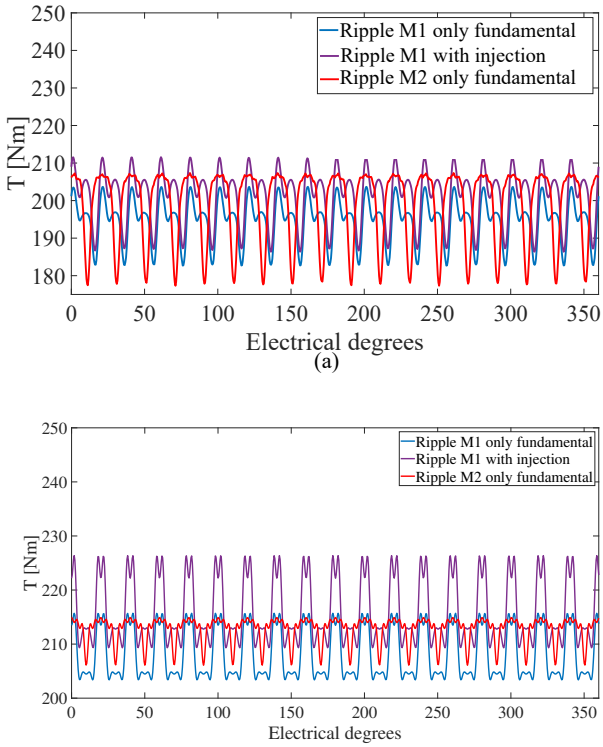

Figure 5.5: (a) FE torque comparison between the machine 1 with and without harmonics injection and the machine 2 with only the fundamental.- (b) Analytical torque comparison between the machine 1 with and without harmonics injection and the machine 2 with only the fundamental.

to the ripple in Fig. 5.6(a) and 5.6(b). It is worth to notice that the average torque values estimated analytically are slightly higher compared to the FEA ones.

It can be due to the fact that the proposed analytical model does not take into the account the slotting effect and the airgap flux density is assumed radial.

From Fig. 5.5(a), it can be highlighted that the current harmonic injection is slightly affecting the torque ripple. For M1, when the harmonics are injected, the ripple is increasing from 10.8% to 12.2%. However, with respect to machine M2 there is a reduction of 1.8%, from 14% to 12.2%. Focusing on the analytical model results (5.5(b)), it is possible to see

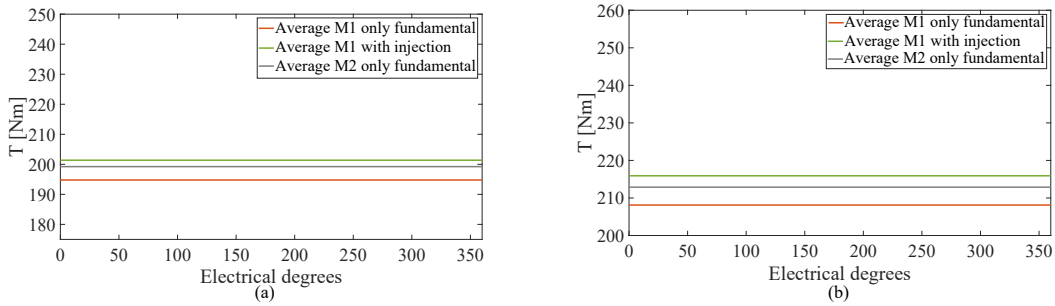

Figure 5.6: (a) FE torque comparison between the machine 1 with and without harmonics injection and the machine 2 with only the fundamental.- (b) Analytical torque comparison between the machine 1 with and without harmonics injection and the machine 2 with only the fundamental.

that the machine M1 presents a ripple without injection by 5.9% and with injection by 7.9% whereas the machine M2, studied only without injection, a ripple by 4.1%.

This is also showing that the combination of permanent magnet span and current harmonic injection can be refined in order to minimise the torque ripple in the machine. It is different with respect to other torque ripple minimisation techniques reported in literature, where the injection of harmonics is not used to increase the torque but to eliminate some harmonic components to reduce its ripple [63].

5.2.2 Current and voltage validation

From a physical point of view, it is not always obvious to understand how the injection of currents, with higher order harmonic with respect to the fundamental, can affect the peak currents and voltages. In this subsection, these aspects are investigated for both machines configurations, M1 and M2. The expression of the currents which flow into the machine windings, with and without current harmonics injection technique, can be represented as

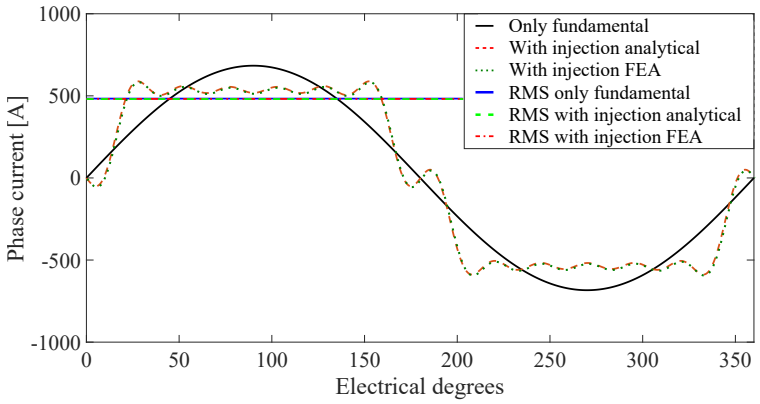

Figure 5.7: Phase current comparison between the machine 1 with and without harmonics injection and the machine 2 with only the fundamental for both analytical and FEA.

follows:

$$i(t) = I_p sin(\omega t), \tag{5.15}$$

$$i(t) = \sum_{i=1}^{13} I_i sin(i\omega t), \tag{5.16}$$

with $i = 1, 3, 5, 7, 9, 11, 13$.

The phase current calculated both analytically and by means of FEA is compared in Fig. 5.7. From the graph, it is difficult to appreciate any difference. The RMS current values are the same with and without harmonic injection. More in detail, the FEA shows that the peak current, with harmonics injection is 16.3% lower with respect to the fundamental peak without current injection. The same waveform from the analytical model is plotted, highlighted in dashed line, showing a good match with the FEA results. This means that even in case of harmonic injection, for the case under study, the inverter switches do not need to be oversized, thanks to the lower peak current.

The phase current with the harmonics injection is based on the BEMF ratios. The BEMF amplitudes comparison is shown in Fig. 5.8 between analytical and FEA for M1.

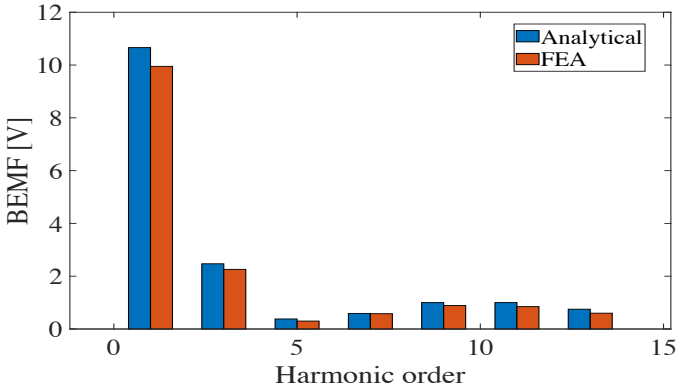

Figure 5.8: BEMF comparison between analytical model and FE analysis for the machine with the 82% of PM span (M1).

The analytical voltage for the phase x (A2) is calculated as:

$$v_x = ri_x + L_x \frac{di_x}{dt} + \sum_{y=1, y \neq x}^{9} M_{xy} \frac{di_y}{dt} + e_x, \tag{5.17}$$

where r is the phase resistance, L_x is the auto-inductance for the phase x (A2), Mxy are the mutual-inductances for the phase x (A2) due to the other stator phases y and e_x is the BEMF for the phase x. The phase resistance and the inductances values, with $nc = 1$, are shown in table 5.4 for the phase x (A2).

The phase voltage waveforms, for both analytical model and FEA, are shown in Fig. 5.9(a) and Fig. 5.9(b), respectively. Both analyses show that the injection, for the proposed PM span Δ_{PM} configuration, does not increase the peak voltage significantly. Indeed, for the FEA, the peak voltage for M1 with the injection is higher by 8.3% compared to M1 and by 5.5% with respect to M2 without injection. The analytical model presents a peak voltage, for M1 with injection, higher by 6.8% with respect to both M1 and M2 without injection.

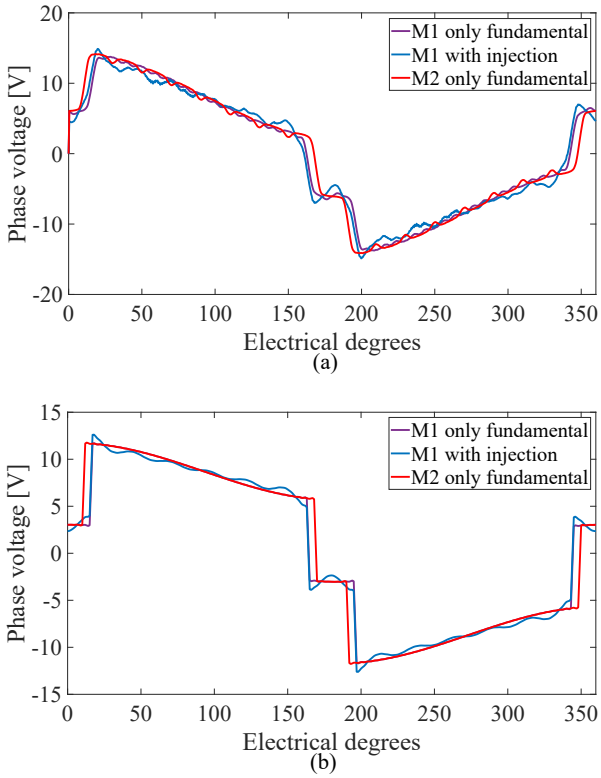

Figure 5.9: (a) FE phase voltage comparison between the machine 1 with and without harmonics injection and the machine 2 with only the fundamental.- (b) Analytical phase voltage comparison between the machine 1 with and without harmonics injection and the machine 2 with only the fundamental. For the analytical voltage calculation 1000 spatial harmonics are taken into the account

5.2.3 Results analyses summary

A summary results for both analytical and FEA are shown in Table 5.5. It is possible to notice that there is a slight displacement between the analytical and FEA torque analyses. This could be due to the fact that the magnetic air-gap δ is enough large for the considered machine ($4mm$). Therefore, the flux density at the air-gap is not total radial but it presents a not negligible tangential component and the proposed analytical model cannot take into the account that. However, the simplified analytical model results can be considered acceptable

Table 5.4: Phase resistance and inductances values for the phase x (A2)

Parameters	Values	Units
r	2.6410^{-4}	Ω
Lx	9.1510^{-6}	H
$Mx1$	5.5210^{-6}	H
$Mx3$	5.5210^{-6}	H
$Mx4$	-7.8810^{-7}	H
$Mx5$	-2.3610^{-6}	H
$Mx6$	-3.9410^{-6}	H
$Mx7$	-3.9410^{-6}	H
$Mx8$	-2.3610^{-6}	H
$Mx9$	-7.8810^{-7}	H

for understanding the main phenomenon of the machine under harmonics injection and which PM span configuration could be more suitable for the proposed harmonics injection technique linked with a possible PM reduction. Actually, for the case under study, the 6% of PM reduction is translated in a lighter machine by 0.12 kg. Indeed, the PM mass into the machine passes from 1.85 kg to 1.82 kg, considering a PM density of 7500 kg/m^3. The efficiency of a generic machine with injection should not change in a significant way with respect to the control with a sinusoidal current. Indeed, for an improved torque would correspond a slight decrement in terms of machine speed, giving in output a similar power (with assumption of similar losses).

Table 5.5: Comparison analysis

-	M1 Analytical	M1 FE
I peak no inj [A]	683.7	683.7
V peak no inj [V]	11.8	13.8
T no inj [Nm]	208	195
I peak with inj [A]	588	582
V peak with inj [V]	12.6	14.8
T with inj [Nm]	216	201
T inc. [%]	3.7	3.2
Ripple no inj [%]	5.9	10.8
Ripple with inj [%]	7.9	12.2
-	M2 Analytical	M2 FE
I peak no inj [A]	683.7	683.7
V peak no inj [V]	11.8	14.0
T no inj [Nm]	213	199
I peak with inj [A]	-	-
V peak with inj [V]	-	-
T with inj [Nm]	-	-
T inc. [%]	-	-
Ripple no inj [%]	4.1	14.0
Ripple with inj [%]	-	-

5.3 Current harmonic injection in the flux weakening region: considerations

In the previous sections, the analysis to increase the output torque is proposed at MTPA operation point. In this one, the fifth current harmonic injection applied in flux weakening region for a SPM machine with 60% of the rotor surface PM span is considered. This PM span has been selected to maximise the fifth harmonic of the BEMF and in the same time to have a good value of the first one (see Fig. 5.2). In order to get the optimum fifth harmonic amplitude for the injection, the BEMF harmonics fifth and first are considered using the following equation:

$$n_5 = \frac{E5}{E1}. \tag{5.18}$$

From the BEMF FFT which is shown in Fig. 5.10, it is possible to calculate $n_5 = 0.23$.

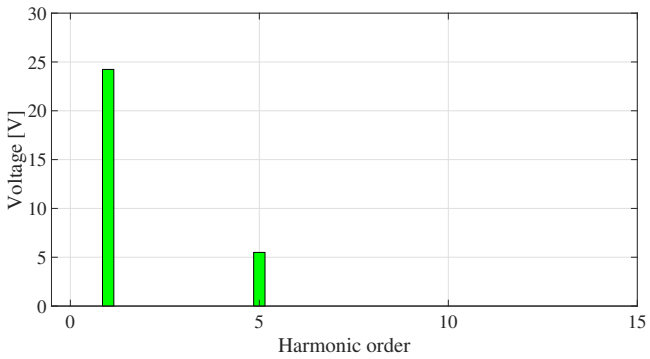

Figure 5.10: BEMF FFT for the SPM machine with 60% of PM span on the rotor surface.

Working in flux weakening region means to increment the rotational speed over the rated operational point. The increment of the rotor speed is linked to an increased voltage amplitude. Therefore, to respect the machine power limit, a reduction of the flux is applied by a phase current decrement. Therefore, an increased speed correspond to a torque decrement.

The idea is to investigate on the possibility to increase the torque in the flux weakening region, respecting the voltage limit of the proposed SPM machine.

As well known in literature, the MTPA for SPM machines in obtained for an angle $\alpha_1 = 90^o$ of the fundamental current. It means $iq = I$ and $Id = 0$. Changing α_1, it is possible to decrease the flux and in consequence to work with an higher speed, increasing the voltage and respecting its limit. The following current angles, expressed in electrical degrees, are considered in the analysis: 100^o, 110^o, 120^o, 130^o, 140^o, 150^o, 160^o, 170^o and 180^o. The torques and powers for both current controls with and without injection, in the flux weakening region, are shown in Fig. 5.11. It can be noticed that for each increment of torque given

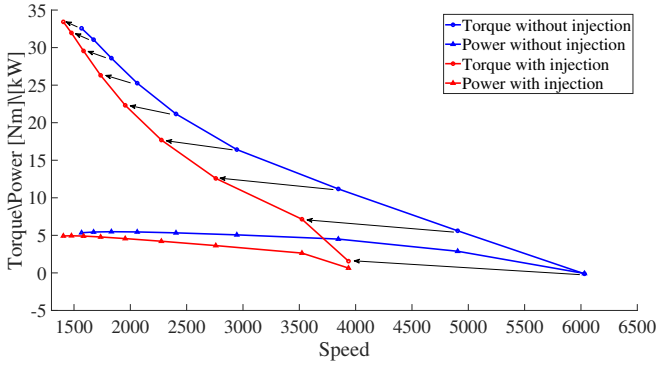

Figure 5.11: Power-Torque curves against Speed in the flux weakening region for the SPM machine with 60% of PM span on the rotor surface.

by the injection, there is a corresponding speed decrement. This leads to a smaller speed range and a limitation to further increasing of the machine speed. Black arrows highlight the torque increment for each point considered. This behaviour, it is in conflictual with the original target of increasing the machine speed thanks to the flux weakening. Therefore, it suggests that applying the current harmonic injection technique for speed above the MTPA operation point does not lead to performance improvements.

5.4 Conclusion

This work investigates on the PM reduction, without affecting the torque performance and Joule losses, for SPM machines. First of all, an analytical model is carried out showing how the no-load flux density, for different spatial harmonics, changes with the Δ_{PM} variation. Then, the same analysis is carried out for the BEMF spatial harmonics studying a triple three-phase winding arrangement. In addition, equations for the optimum harmonic injection amplitudes to maximise the torque, while keeping constant the RMS current with respect to the current control with the only fundamental component, are presented. The current amplitude of each injected harmonics depends of the BEMF ratios. The proposed current harmonics injection technique takes into the account the following temporal harmonics: 3^{rd}, 5^{th}, 7^{th}, 9^{th}, 11^{th}, 13^{th}. The analytical torque comparison between the current control with and without harmonics injection is shown as a function of the Δ_{PM} variation, highlighting the torque increment once the harmonics injection is applied. The analytical model is validated via FEA which compares a SPM machine with 82% of PM span (M1), with and without harmonics injection, and a SPM machine with 88% of PM span (M2), feeding with only the fundamental current component. The analysis shows, for the case under study, that it is possible to reduce the PM content of the 6%, once that the considered current harmonics are injected, without affecting torque performance, peak current and peak voltage. The slight displacement between analytical and FEA can be justified by the fact that the flux at the airgap is not total radial and the analytical model cannot take into the account that. However, the simplified analytical approach can give important information on which PM percentage on the rotor surface is better than others for injecting high current temporal harmonic components in order to increase the torque or to reduce the PM content, keeping the same RMS current value of the current control without injection, thus the same Joule losses.

At the end of this chapter, it has been shown that the application of the current harmonic

injection technique, for improving the torque in the flux weakening region, is not suitable without a machine speed reduction which contrasts to work over the rated speed.

Chapter 6

On Current Harmonic Injection to Maximise the Torque Capability for both Isotropic and Anisotropic Electrical Machines

In this chapter, a comparison between three different methods for improving the torque by fifth harmonic current injection is carried out for SPM and IPM machines. In particular, the fifth harmonic is injected based on amplitudes and angles derived from BEMF (CHIB), load voltage (CHIV) and the optimum solution obtained by FEA (CHIO), respectively. Firstly, the harmonic spectra of no load and load voltages are investigated and validated via FEA for both machine topologies. From the analysis, the values to apply for the fifth harmonic injection are obtained. Secondly, the optimum technique for the current fifth harmonic injection, in order to maximise the torque, is carried out via FEA. Thirdly,

a comparison of the proposed three different techniques is reported on both machine topologies, showing the torque improvements and highlighting their advantages and disadvantages. Finally, the concept is validated via experimental test on a dual three-phase IPM machine with a V-Shape rotor array.

6.1 Analytical Model

In this section, an analytical study of no load BEMF and load voltage is carried out for the spaces 1 and 5 in the ρ_{th} complex plan (space) α_ρ-β_ρ, applying the Space Vector Decomposition (SVD) theory. Considering a dual three-phase winding layout, which can be represented by the sum of two three-phase subsystems shifted each other of $\frac{\pi}{6}$ radians, the voltage equation for a generic x-th phase can be written as:

$$v_x = v_{R,x} + \frac{d\psi_{l,x}}{dt} + \frac{d\psi_{g,x}}{dt} \tag{6.1}$$

where $v_{R,x}$ is the resistive voltage drop, $\frac{d\psi_{l,x}}{dt}$ represents the leakage self inductance in the slot and $\frac{d\psi_{g,x}}{dt}$ takes into the account for all the not leakage flux linked with the x-th phase, sum of stator and rotor contributions; The Clarke transformation for the proposed dual three-phase system is reported below:

$$\begin{aligned} \bar{y}_\rho = &\frac{2}{6}(x_{A1} + x_{B1}e^{j\rho\frac{4\pi}{6}} + x_{C1}e^{j\rho\frac{8\pi}{6}}) + \\ &+ \frac{2}{6}(x_{A2}e^{j\rho\frac{\pi}{6}} + x_{B2}e^{j\rho\frac{5\pi}{6}} + x_{C2}e^{j\rho\frac{9\pi}{6}}) \end{aligned}, \rho = 0, 1, ..., \infty. \tag{6.2}$$

where j is the unity imaginary number, $\bar{y}_\rho$ is the Space Vector in the ρ_{th} complex plan α_ρ-β_ρ. Therefore, the ρ-th space vector of the phase voltages can be written as:

$$\bar{v}_\rho = \bar{v}_{R,\rho} + \frac{d\bar{\psi}_{l,\rho}}{dt} + \frac{d\bar{\psi}_{g,\rho}}{dt}, \rho = 0, 1, ..., \infty. \tag{6.3}$$

Considering only the rotor contribution, the generic phase voltage x-th is the no load BEMF, which is renamed as e_x below:

$$v_x = e_x = \frac{d\psi_{g,x}}{dt} \tag{6.4}$$

Therefore, the phase voltage in the space represented in (6.3), can be re-written as:

$$\bar{e}_\rho = \frac{d\bar{\psi}_{g,\rho}}{dt} \tag{6.5}$$

Leading to:

$$\bar{v}_\rho = \bar{e}_\rho. \tag{6.6}$$

Supplying the machine with a current which presents the only fundamental component, and considering the only spaces $\rho = 1, 5$, the voltages for an SPM machine can be written with good approximation as:

$$\bar{v}_1 = R\bar{i}_1 + L_1\frac{d\bar{i}_1}{dt} + \bar{e}_1 \tag{6.7}$$

$$\bar{v}_5 = R\bar{i}_5 + L_5\frac{d\bar{i}_5}{dt} + \bar{e}_5 \tag{6.8}$$

Under the hypothesis of fundamental current component the space current vectors are $\bar{i}_1 = \bar{i}_{ref}$ and $\bar{i}_5 = 0$. Therefore, the fifth space vector voltage is equal the no load BEMF of the same space:

$$\bar{v}_5(i_5 = 0, i_1 \neq 0) = \bar{e}_5 \tag{6.9}$$

However, the equation (6.9) is true only for machines which present an isotropic magnetic circuit (i.e SPM machines, when not heavily saturated). The next section, a FEA is carried out to identify and demonstrate that there is a displacement between $\bar{v}_5$ and $\bar{e}_5$ for machines with anisotropic behaviour (i.e IPM machines), thus:

$$\bar{v}_5(i_5 = 0, i_1 \neq 0) \neq \bar{e}_5 \tag{6.10}$$

Therefore, the subspaces 1 and 5 are not decoupled.

Table 6.1: IPM Machine parameters

Parameters	Values	Units
Poles number	8	-
Slots Number	48	-
Turns per coil	8	-
Length steak	110.0	mm
Outer stator diameter	203.0	mm
Inner stator diameter	138.0	mm
Slogt height	25.07	mm
Back iron height	33.1	mm
Tooth width	5.2	mm
Slot opening width	2.5	mm
Slot opening height	0.6	mm
Wedge height	0.6	mm
Airgap	0.7	mm
Outer rotor diameter	136.6	mm
Magnet length	20.0	mm
Magnet height	4.0	mm
Cooling	natural convection	
Magnets material	rare earth (NdFeB)	-

6.2 Analytical Model Validation and Search Optimum Current Injection

6.2.1 Finite Element Validation of the Analytical Model

In this subsection, the equations presented in section 6.1 are validated via FEA on both dual three-phase SPM and IPM machines in order to highlight the differences in terms of voltage space 5. Fig. 6.1 shows the layouts of the machines under study.

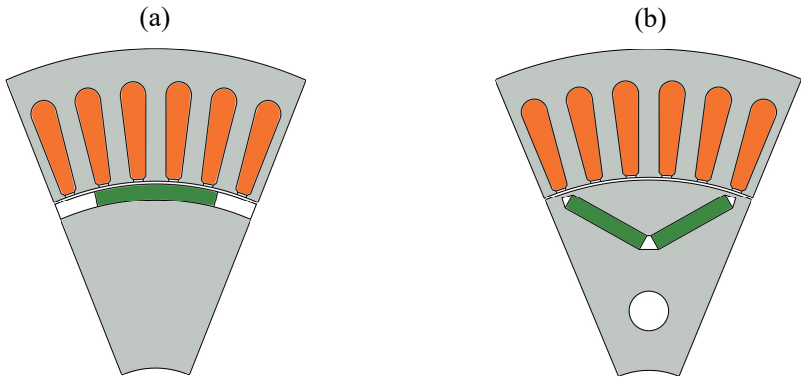

Figure 6.1: Machine analysed: (a) SPM - (b) IPM V-Shape.

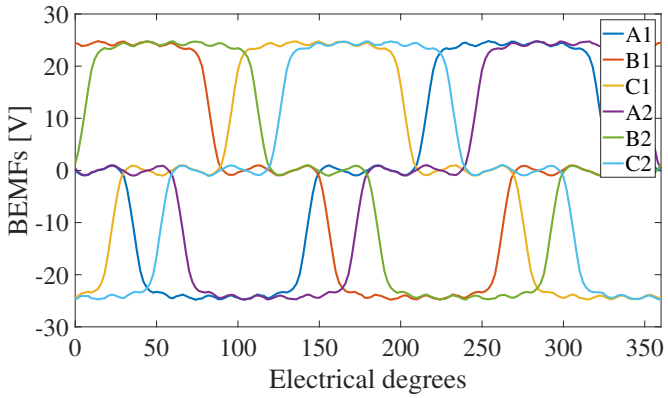

Figure 6.2: SPM machine BEMF waveforms at 1500 rpm.

The two machines feature the same stator, as well as the same winding layout. The main machine parameters of the IPM topology are listed in Table 6.1. The SPM magnets are made by ferrite to avoid the iron saturation and permit a pure isotropic machine behaviour for an appropriate study and comparison with respect to anisotropic machines such as the proposed IPM which presents rare earth (NdFeB) permanent magnets.

Under hypothesis of a fundamental phase current amplitude $I = 71.25A$, the no load BEMFs and load phase voltages are shown in Figs 6.2, 6.3 for the SPM machine and in Figs. 6.4,

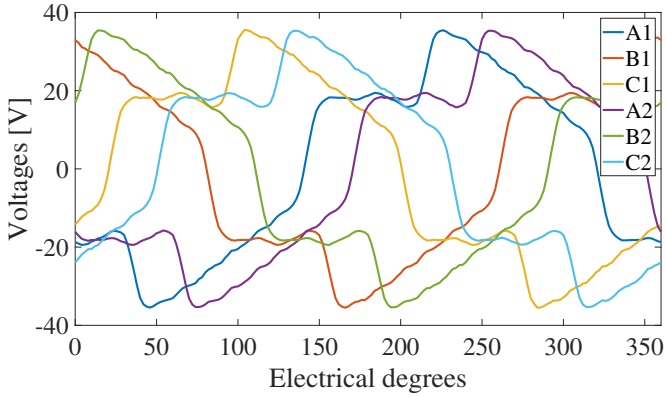

Figure 6.3: SPM machine waveform voltages when the machine is supplied by a fundamental current of I=71.25A.

6.5 for the IPM one.

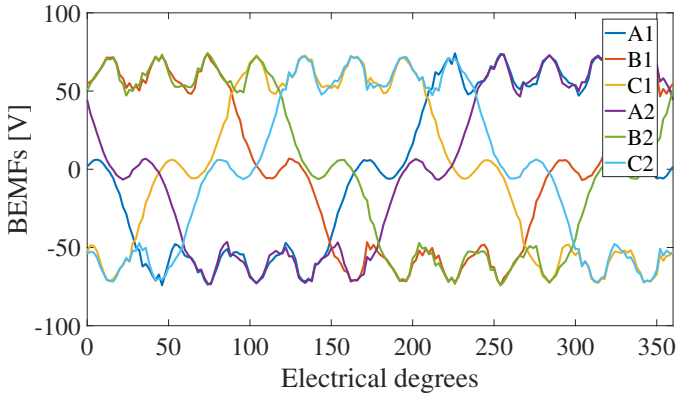

Figure 6.4: IPM machine BEMF waveforms at 1500 rpm.

Studying the space 1 and 5 in separate way (Figs. 6.6 and 6.7), it is possible to appreciate that the no load BEMF for the spatial harmonic ρ_5 are almost equal with respect to the same harmonic in load voltage conditions for the SPM machine whereas they are different for the IPM machine in accordance with the equations (6.9) and (6.10).

Table 6.2 summaries the amplitudes and angles of the spatial harmonics ρ_1 and ρ_5, also

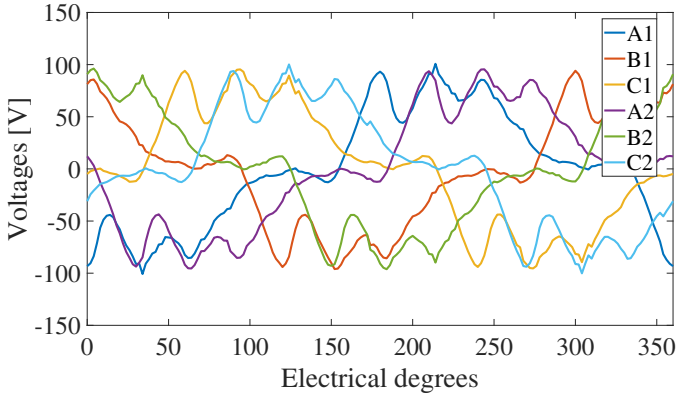

Figure 6.5: IPM machine waveform voltages when the machine is supplied by a fundamental current of I=71.25A.

Table 6.2: no load and load voltages for the spatial harmonics ρ_1 and ρ_5

Machine	E1 [V]	E5 [V]	γ_{E1}	γ_{E5}
SPM	24.3	5.51	91.8	-81.0
IPM	69.6	8.3	92.0	-79.9
Machine	V1 [V]	V5 [V]	γ_{V1}	γ_{V5}
SPM	37.5	5.49	141.6	-81.3
IPM	73.0	13.7	142.5	-160.0

displayed in Figs. 6.6 and 6.7.

6.2.2 Optimum of injection for the fifth harmonic of current

In this subsection, the optimum injection of the fifth current harmonic to maximise the torque, keeping the RMS current constant, is carried out via FEA on both machines under study. At the first stage, the machine is supplied by a fundamental peak phase current $I = 71.25A$, to get the MTPA angle $\alpha_{opt,1}$ for both machine topologies (Fig. 6.8).

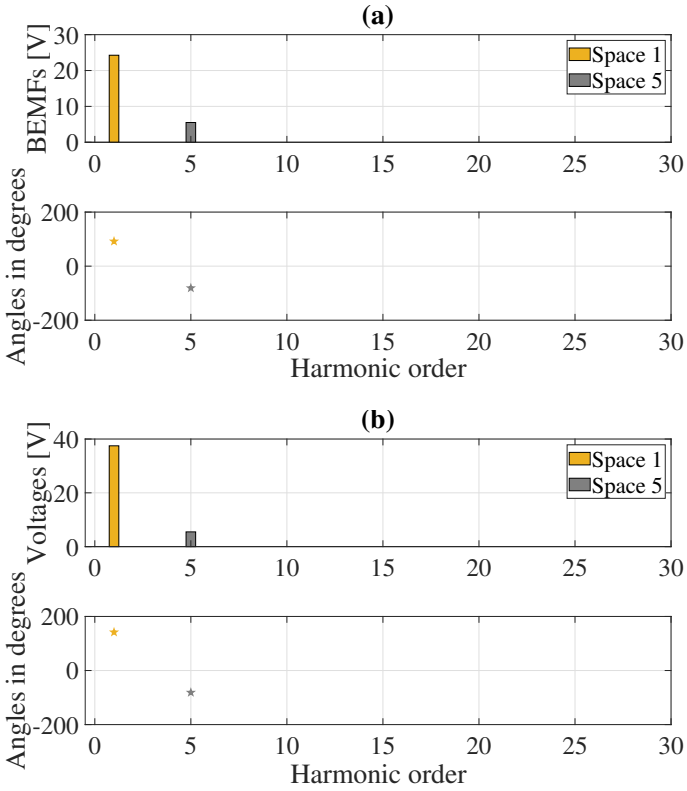

Figure 6.6: (a) SPM machine no load BEMFs spaces 1 (orange) and 5 (grey) - (b) SPM machine load voltages spaces 1 and 5

It has been obtained to change the fundamental current angle $\alpha_{opt,1}$ to keep constant the amplitude $I = 71.25A$ for the initial rotor position. It is defined as the rotor d-axis aligned with the phase A1.

Under the hypothesis of fundamental current harmonic injection only, for the proposed dual three-phase SPM machine, the torque can be written as:

$$T_i = \frac{6}{2}\frac{1}{\omega_m} IE1, \tag{6.11}$$

where ω_m is the mechanical pulsation expressed in rad/s. Injecting the fifth harmonic of

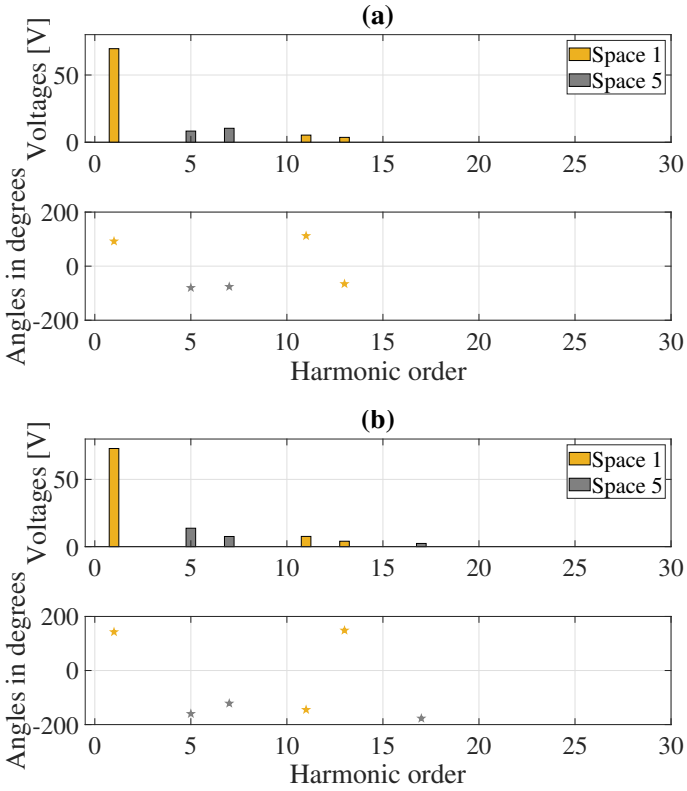

Figure 6.7: (a) IPM machine no load BEMFs spaces 1 (orange) and 5 (grey) - (b) IPM machine load voltages spaces 1 and 5

current, the torque becomes:

$$T_f = \frac{6}{2}\frac{1}{\omega_m}(I1E1 + I5E5) \tag{6.12}$$

Forcing the system to keep the current RMS constant, with the constrain equation written below:

$$I^{*2} + n^2 I^{*2} = I^2, \tag{6.13}$$

The equation (6.12) can be re-written as:

$$T_f = \frac{6}{2}\frac{1}{\omega_m}(\frac{I}{\sqrt{1+n^2}}E1 + n\frac{I}{\sqrt{1+n^2}}E5) \tag{6.14}$$

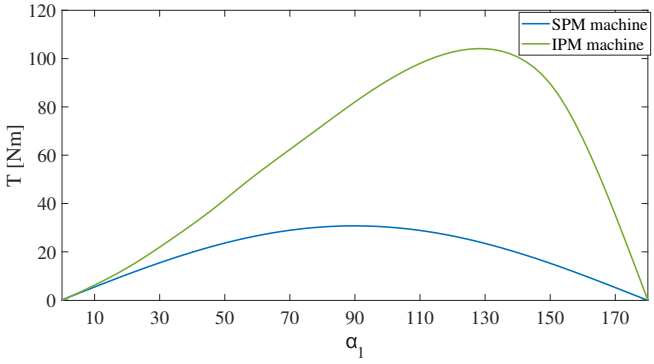

Figure 6.8: MTPA comparison when the machines are supplied by a fundamental current of I=71.25A.

Differentiating (3.12) and (3.15) with respect to n and equalising it to zero, it is possible to get the maximum torque:

$$\frac{d(T_f - T_i)}{dn} = \frac{6}{2}\frac{I}{\omega_m}(n\frac{E5}{\sqrt{1+n^2}} + E1(n\frac{1-\sqrt{1+n^2}}{\sqrt{1+n^2}}) = 0 \tag{6.15}$$

From (6.15), it is possible to get the optimum amplitude for the fifth harmonic:

$$n = \frac{E5}{E1} \tag{6.16}$$

The new fundamental and the fifth harmonics of current can be written, respectively as:

$$I_1 = \frac{I}{\sqrt{1+n^2}} \tag{6.17}$$

$$I_5 = \frac{I}{\sqrt{1+n^2}}n \tag{6.18}$$

In order to determine the optimum angle of injection to maximise the torque, an analysis for different fifth harmonic current angles α_5 is shown in Fig. 6.9 and 6.10 for both SPM and IPM machines, respectively.

The average torque is obtained for each α_5 value. From the analysis of both figures, it is shown that the optimum fifth harmonic injection angle for SPM machines is $\alpha_{opt} = -90^o$

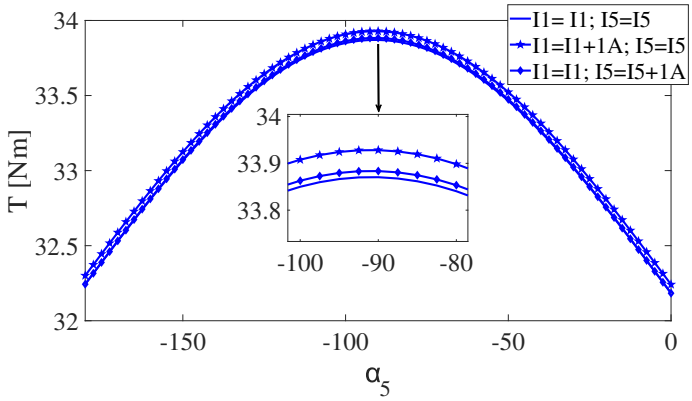

Figure 6.9: SPM machine: Average torque for different α_5 and phase current amplitudes

whereas it is $\alpha_{opt} = -170^o$ for the proposed IPM V-Shape machine. In order to get the optimum fifth harmonic amplitude, differential constant torques for the fundamental and fifth spatial harmonics which are calculated as:

$$z_{T_1} = \frac{dT}{di_1} = \frac{T'_{max} - T_{max}}{di_1} \tag{6.19}$$

$$z_{T_5} = \frac{dT}{di_5} = \frac{T''_{max} - T_{max}}{di_1} \tag{6.20}$$

where T_{max} is the maximum average torque when the machine is supplied with the currents resulting by solving (6.18) and (6.17), T'_{max} is the maximum average torque when the machine is supplied with $I_1 = I_1 + 1A$ and $I_5 = I_5$, T''_{max} is the maximum average torque when the machine is supplied with $I_1 = I_1$ and $I_5 = I_5 + 1A$. The results are included in Figs. 6.9 and 6.10 for the two different machines, respectively. At this point, it is possible to calculate the optimum amplitude n_{opt5} for the injection as:

$$n_{opt5} = \frac{z_{T_5}}{z_{T_1}} \tag{6.21}$$

Table 6.3 summaries the torque results obtained and shown in Figs. 6.9 and 6.10 with the optimum amplitude n_{opt5} and angle $a_{5,opt}$ values for both machine topologies.

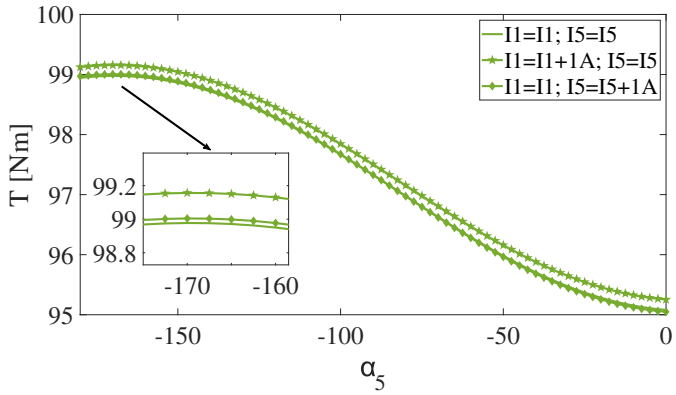

Figure 6.10: IPM machine: Average torque for different α_5 and phase current amplitudes.

As expected, The FEA results show that the optimum amplitude is in accordance with the equation (6.16) for the SPM with a fifth harmonic amplitude n_{E5}=$n_{5,opt}$ = 0.23 as well as the optimum angle which is similar to the expected one α_{E5}=-81^o and $\alpha_{5,opt}$=-90^o. On the other hand, the load voltage analysis presents results with a similar match on the injection angle, but with a higher discrepancy in terms of magnitude, with $n_{V5} = 0.15$ and α_{V5}=-81.3^o. Regarding the IPM machine, the analysis shows that the optimum amplitude $n_{5,opt}$ = 0.15 and angle $\alpha_{5,opt}$=-170^o present an important displacement with respect to the BEMF values n_{E5} = 0.12 and α_{E5}=-79.9^o. In contrast, they are close to the voltage values, in particular for the angle with α_{V5}=-160^o, while the magnitude is n_{E5} = 0.19. The analysis suggests that the proposed CHIV can be applied for both machines with a good accuracy, indifferently.

Table 6.3: Optimum amplitude $n_{5,opt}$ and angle $\alpha_{5,opt}$ for the injection

Values	SPM	IPM
T_{max}	33.8704 Nm	98.9774 Nm
T'_{max}	33.9282 Nm	99.1566 Nm
T''_{max}	33.8835 Nm	99.0050 Nm
n_{opt5}	0.226	0.154
$\alpha_{5,opt}$	-90.00^o	-170.00^o

6.3 Current harmonic injection techniques comparison

In this section, the proposed CHIV is compared with respect to CHIB and CHIO obtained via FEA, which is considered as benchmark. The injection values, which are obtained in subsections 6.2.1 and 6.2.2, are reported in table 6.4. The comparisons are shown in Fig. 6.11 for the SPM and in Fig. 6.12 for the IPM machines.

From Fig. 6.11, it is possible to appreciate a torque improvement by current fifth harmonic injection with respect to supplying the machine with only fundamental component for all three proposed techniques.

Table 6.4: Amplitudes and angles of the proposed three different injection techniques

Values	SPM	IPM
n_{E5}	0.23	0.12
n_{V5}	0.15	0.19
n_{opt5}	0.23	0.15
α_{E5}	-81.00^o	-79.90^o
α_{V5}	-81.30^o	-160.00^o
α_{opt5}	-90.00^o	-170.00^o

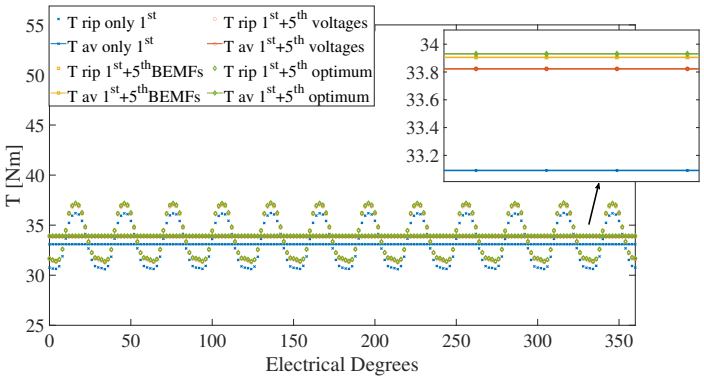

Figure 6.11: SPM machine torque comparison with and without injection for the proposed three different techniques - ripple represented with markers only, average represented with markers and full line.

In particular, the CHIV improves the torque by 2.2% whereas the CHIB, which matches with the CHIO, by 2.4%. It means that for the isotropic SPM machines the technique based on the BEMF values is slightly more accurate than the one based on the voltage. However, the two techniques can be considered comparable in terms of performance. Fig. 6.12 shows a torque increment by 1.13% for the IPM machine due to the CHIV which presents the same result of the CHIO. In contrast, the CHIB shows a lower torque with respect the case without fifth harmonic injection by -0.73%. It can be due to the reluctance effects which are introduced when the machine is supplied by a load current. These effects are take into the account by the CHIV which features ad increases of torque performance comparable with the one obtained with the optimal control parameters.

In Figs. 6.13 and 6.14, the torque harmonic spectra for the control with and without current harmonic injection is shown for all proposed three techniques on both SPM and IPM machines, respectively. As might be expected, the 12th harmonic is the first with an order higher than the fundamental due to the proposed dual three-phase winding configurations. It is possible to appreciate that the harmonic injection does not significantly affect the torque ripple in the SPM machine and it is slightly lower once the current harmonic injection is

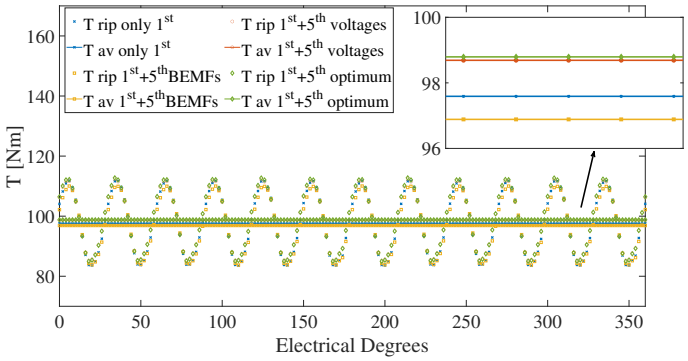

Figure 6.12: IPM machine: Torque comparison with and without injection for three different techniques - ripple represented with markers only, average represented with markers and full line.

applied to the IPM one.

The CHIB can be applied only for isotropic machines, knowing in advance the values and loading the data offline as well as the CHIO with the difference that it can be applied on both machine topologies, ensuring high accuracy.

The proposed CHIV is the unique between them that can be applied online and for both machine topologies ensuring a good accuracy and for that it can be considered model-free. It is possible because once the machine is supplied with a generic current I, the values for the harmonic injection can be measured on the controller, directly. The limit of this technique is mainly on the magnitude of the harmonics to be injected. In fact, the results reported in Table 6.4 show that the injection ratio is $n_{V5} = 0.15$ and $n_{opt5} = 0.23$ for the SPM machine and $n_{V5} = 0.19$ and $n_{opt5} = 0.15$ for the IPM one. However, it does not strongly affect the torque improvement with respect to the optimum technique because the injection angle is enough accurate ($\alpha_{V5} = -81.3^o$ and $\alpha_{opt5} = -90.0^o$ for the SPM machine and $\alpha_{V5} = -160.00^o$ and $\alpha_{opt5} = -170.00^o$ for the IPM one).

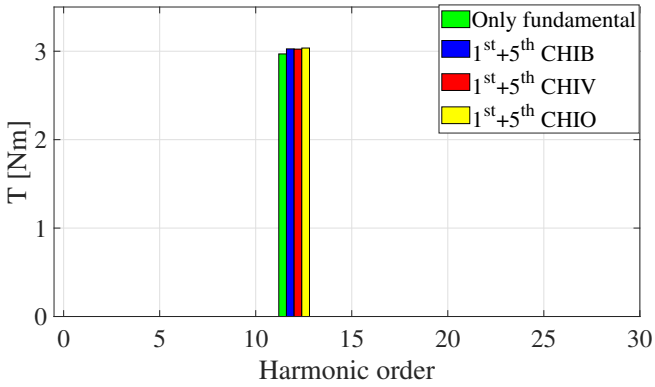

Figure 6.13: SPM machine: FFT torque comparison with and without injection for the proposed three different techniques

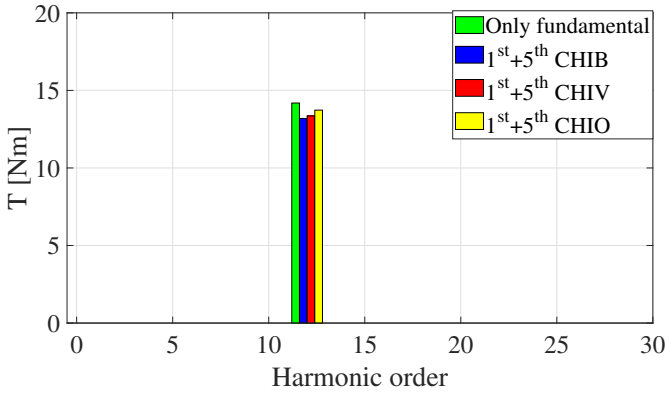

Figure 6.14: IPM machine: FFT torque comparison with and without injection for three different techniques

6.4 Experimental Validation of the Analytical Voltage Analysis

In this section, an experimental test is carried out in order to validate the approach proposed in section 6.1 and 6.2.1. The test rig is shown in Fig. 6.15, where the IPM machine under study, the induction motor (load), the two 3-levels inverters, and the control platform are highlighted. The IPM V-Shape machine under study is presented in Fig. 6.1-(b) and its main parameters are listed in TABLE 6.1. The switching frequency of the inverter switches is 20 kHz and the measured results are acquired at the same frequency from the control board, directly.

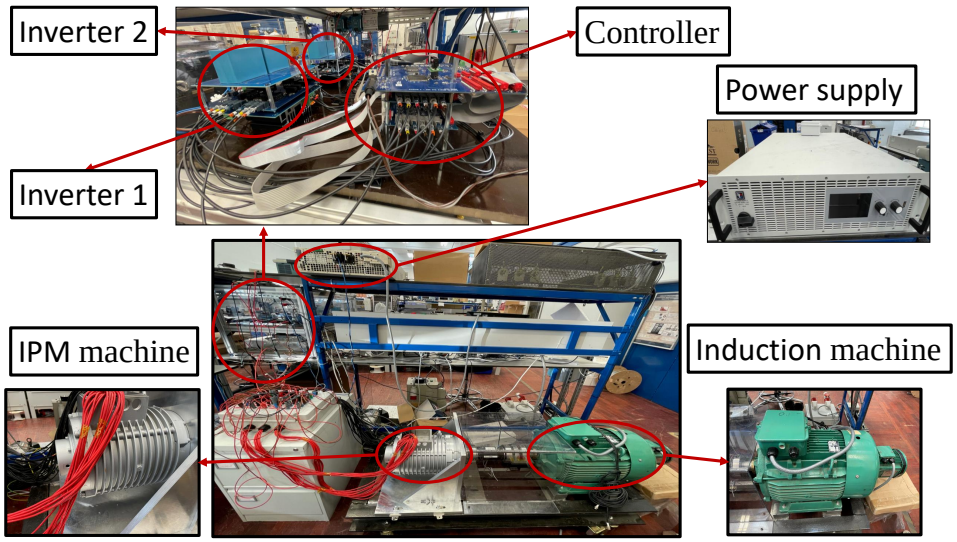

Figure 6.15: Rig for the experimental test.

The inverter current limit is set at $I = 15A$. The experimental phase BEMF waveforms are shown in Fig. 6.16 when the machine is rotating at 1500 rpm thanks to the coupled induction motor. The BEMF waveforms present a slight difference with respect to the FEA

Table 6.5: Experimental no load and load voltages for the spatial harmonics 1 and 5

I [A]	E1 [V]	E5 [V]	γ_{E1}	γ_{E5}
NO LOAD	57.5	6.2	-108.5	12.7
I [A]	V1 [V]	V5 [V]	γ_{V1}	γ_{V5}
7.5	64.8	5.0	-99.0	-9.0
10	66.3	4.9	-96.0	-18.0
12.5	67.8	4.6	-92.3	-19.6
15	69.6	4.6	-89.9	-28.0

results presented in Fig. 6.4 due to the rotor skewing of the real machine. Fig. 6.17 shows the voltage waveforms for the phase A1 with load currents of 7.5A, 10 A, 12.5 A and 15 A, while the machine is rotating at 1500 rpm and the induction motor works as break. All fundamental currents are injected with an angle $\alpha_1 = -105^o el$ (the control coding presents opposite angles with respect to the usual conventions).

Applying the Clarke transformation (6.2) to the obtained voltage waveforms, it is possible to get amplitudes and angles for their space 5, respectively. In table 6.5 are summarised the amplitudes and angles of the no load BEMF and load voltages for the spatial harmonics ρ_1 and ρ_5, which are shown in Fig. 6.18.

Analysing the captured data and focusing on the spatial harmonic ρ_5, it is clear that there is a displacement between amplitudes and angles in no load and load conditions, in accordance with sections 6.1 and 6.2.1. In addition, it is possible to appreciate that the displacement between the angle γ_{E5} and γ_{V5} becomes larger increasing the load current (i.e. the anisotropic behaviour of the machine).

The same back electro-motive force and load voltage analyses are proposed also by FEA, studying the machine in the same load current conditions of the experimental test. The

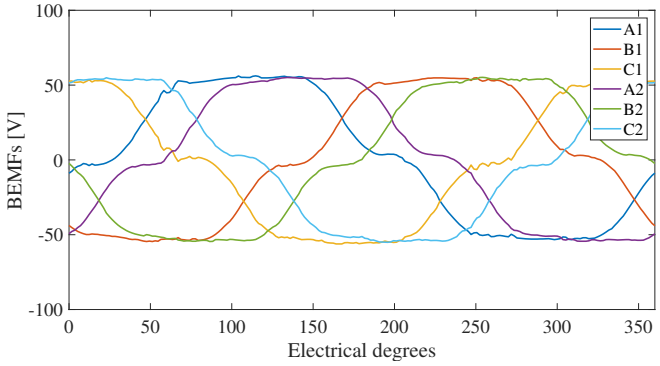

Figure 6.16: IPM machine experimental BEMF waveforms at 1500 rpm: measured from the controller directly

rotor skewing, a slot quarter, of the real machine is taken under consideration simulating for two rotor positions the same load operation point. The final voltage waveform is the combination of the two simulations. Applying the Clarke transformation on the final voltage waveform, it is possible to have the subspace 1 and 5, separately also for the FEA.

In Fig. 6.19, the voltage amplitudes and angles for the mentioned subspaces are analysed in a qualitative way, and it is possible to consider that the BEMF and load voltage space 5 trends are confirmed. Indeed, it shows a larger displacement between the BEMF and load voltage when higher is the load current (i.e., higher machine reluctance). This is more evident for the angles. The quantitative comparison of the subspace 5 between experimental (Fig. 6.18) and FEA (Fig. 6.19) of the voltages shows that there is a maximum amplitude error of 4 % and a maximum angle error of 14 %.

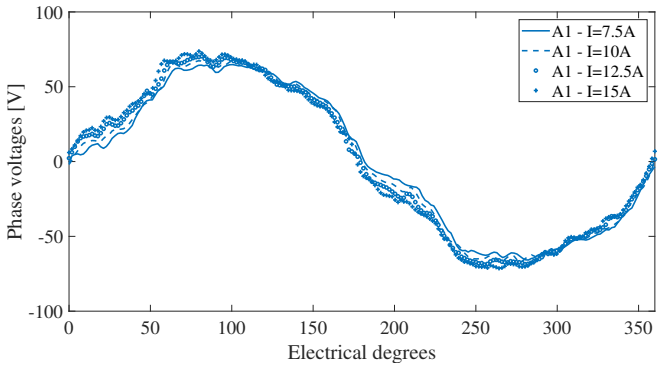

Figure 6.17: IPM machine experimental load voltage waveforms for the phase A1, when the machine is rotating at 1500 rpm: measured from the controller directly

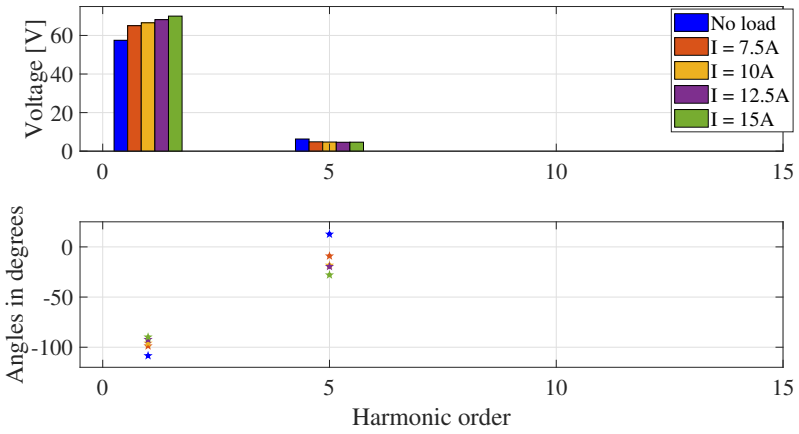

Figure 6.18: IPM machine experimental spatial harmonics 1 and 5 for different load conditions

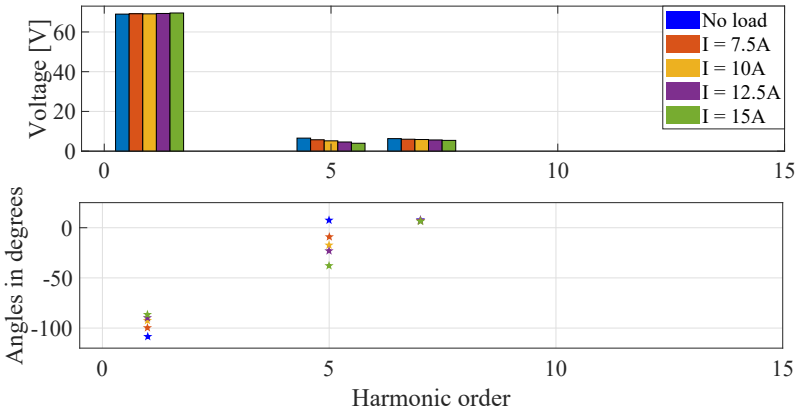

Figure 6.19: IPM machine FEA spatial harmonics 1 and 5 for different load conditions

6.5 Conclusion

This work proposes a novel model-free current harmonic injection technique to maximise the machine torque capability, based on the machine voltage amplitudes and angles (CHIV). FEA simulations are carried out in order to study the differences in terms of voltage waveforms between isotropic and anisotropic machines, showing how these differences affects the performance of the machine under fifth current harmonic injection. The no load BEMF and load voltage for the fifth harmonic are the same for isotropic machines (i.e SPM machines, when not heavily saturated) where there is not reluctance effects. In contrast, the machines with an anisotropic magnetic circuit (i.e IPM) show a displacement in the voltage mapped in the fifth subspace in no load and load conditions due to the reluctance effects, which are introduced when the machine is supplied by a current. The proposed concept is validated on an IPM V-Shape machine, experimentally. Based on this concept, the proposed technique is compared with one based on the BEMF values (CHIB) and the optimum one (CHIO), which is considered as benchmark, in FEA. The FEA shows that the proposed CHIV is similar to the CHIO for both isotropic and anisotropic machines in terms of torque improvement. Therefore, the proposed CHIV can be used with a good accuracy on both isotropic and anisotropic machines, indifferently. On the contrary, the CHIB can be applied on isotropic machines only. In addition, the proposed CHIV can be applied without the prior knowledge of magnitude and phase angle for the injection of the current fifth harmonic, because it uses the indirect measurement of the phase voltages required by the controller to keep the currents at their reference values. Therefore, the proposed approach could be considered model-free.

Chapter 7

Rotor Optimization to Maximise the Torque in Dual Three-Phase IPM V-Shape Machines Under Current Fifth Harmonic Injection

Based on the analysis proposed in chapter 6, it is clear that the IPM V-Shape machine available in laboratory is not adapt to increase the torque capability by current harmonic injection. It is due to the fact that the ratio between the voltage spatial harmonic 5 and 1 is low.

This chapter proposes sensitivity analyses in order to find the optimum rotor configuration, keeping the V-shape concept, to increase the torque by fifth harmonic injection.

In addition, the analyses can help designers and researchers to reduce the PM content in

the machine, without affecting the torque performance and Joule losses.

7.1 FEA: Computational Process

In this section is reported the computational process to get the ripple torque, average torque and the ratio n_{V5} for different angles of the IPM V-Shape and rib next to the airgap. These two parameters are highlighted in Fig.7.1.

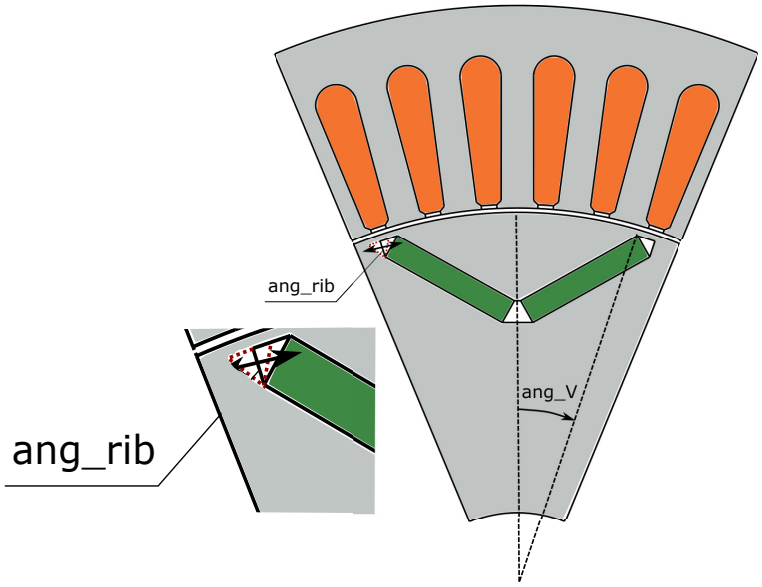

Figure 7.1: IPM V-Shape: highlighting of the V and rib angles.

The stator and the other parameters are the same of the original machine (Table 6.1) which presents a V angle of 16.6^o. In order to save computational time, the hole into the rotor has been removed because its electromagnetic influence can be neglected for the proposed sensitivity analyses.

The computational procedure starts to draw one pole of the machine. The second step analyses the MTPA for the set rotor configuration parameters, changing the current angle while the rotor is blocked in one position, with the d axis of the d-q reference frame aligned with the phase A1 of the machine. The machine is supplied with a fundamental phase current amplitude of $I = 71.25A$, which corresponds to a slot current of $I = 570A$ (nc=8 conductors per slot) and a slot current density of $J = 4.55A/mm^2$. At this point, feeding the machine with the obtained MTPA for the considered current amplitude, the simulations can be implemented for different rotor positions in order to get the average torque, torque ripple and the phase fluxes for one electrical period. Based on the phase fluxes, it is possible to calculate the phase voltages as:

$$v_x = \frac{d\phi_x}{dt}, \tag{7.1}$$

where x is the generic phase and ϕ is the flux in load conditions. The phase voltages are calculated for a machine rotational speed of $\omega_m = 1500rpm$.

Once the phase voltages are obtained, the best solution would be to apply the Clarke transformation (6.2) in order to get the voltage spatial harmonic 5 and 1, separately. However, in order to save time in the computational process, the phase voltages are analysed by FFT. Therefore, the fifth harmonic amplitude $n_{V5} = \frac{V_5}{V_1}$ is calculated dividing the harmonic 5 and 1 which are obtained via FFT. Section 7.2 will be shown that the results between these two solutions are comparable.

The proposed computational process is shown in Fig. 7.2 with a workflow chart.

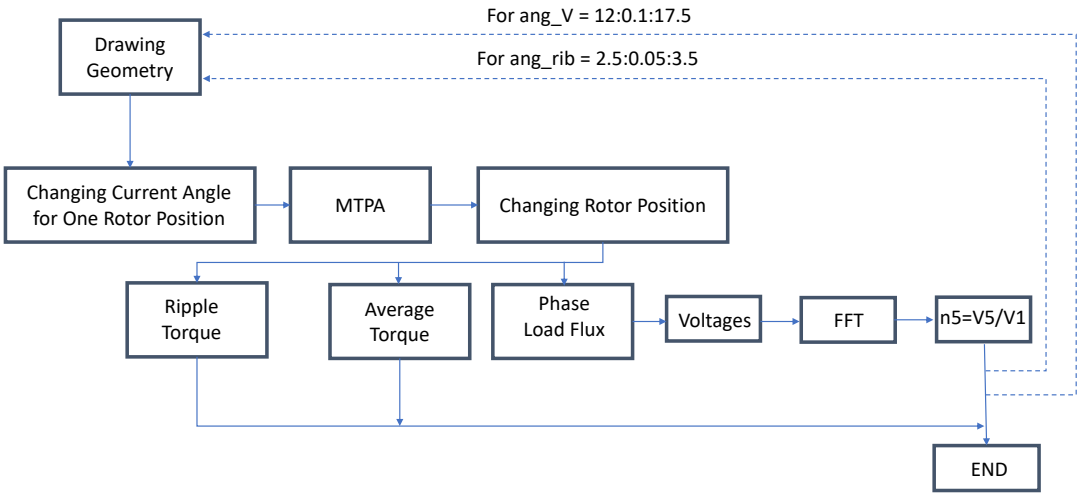

Figure 7.2: Workflow chart of the proposed computational process to enhance the voltage fifth harmonic in a dual three-phase IPM V-Shape machine.

7.2 FEA: Analyses Results Discussion

The proposed sensitivity analyses target is to enhance the ratio between the voltage fifth and first harmonics in order to maximise the torque, injecting the fifth harmonic of current. The proposed analyses investigate on the average torque, ripple and n_{V5} while the V and rib angles are changing. The investigation is carried out for the V angles between 12^o and 17.5^o with a step of 0.1^o whereas the rib angles between 2.5^o and 3.5^o with a step of 0.05^o. The minimum limit has been chosen at 12 degrees because under this value the torque produced by the fundamental is too small due to the PM reduction. It is important to notice that more the V angle is lower, lower is the PM content in the machine. In Fig. 7.3 is shown the analysis of the average torque for different V and rib angle values. As might be expected, the average torque trend increases with the V angle increment which is strictly linked to

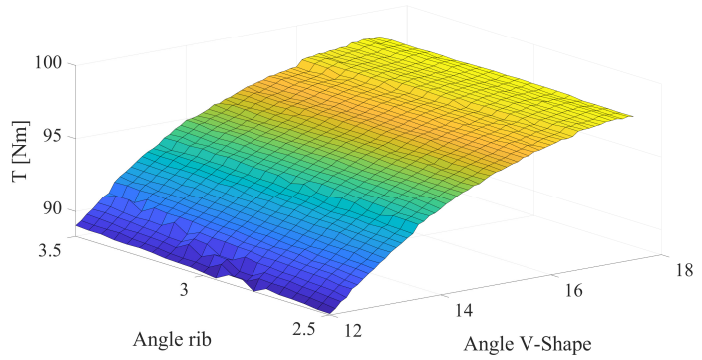

Figure 7.3: IPM V-Shape: analysis of average torque for different V and rib angles.

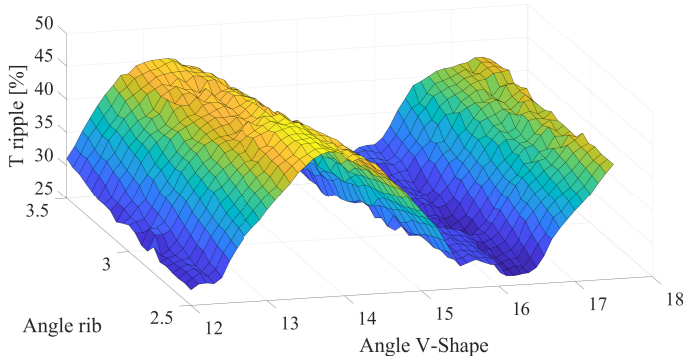

Figure 7.4: IPM V-Shape: analysis of torque ripple for different V and rib angles.

the PM content increment in the machine. It is possible to notice that the rib angle does not influence the average torque in a strong way.

Fig. 7.4 shows the torque ripple for different V and rib angles. It is interesting to notice that the lowest ripple is obtained for the V angle around $12^o/12.5^o$ and $16^o/16.5^o$. This time, the rib angle presents a higher influence with respect to the average torque case. For example, if the V angle is 12^o and rib angle 2.5^o, the ripple is lower than 30% whereas for the same value of the V angle and a rib angle of 3.5^o it exceed this value.

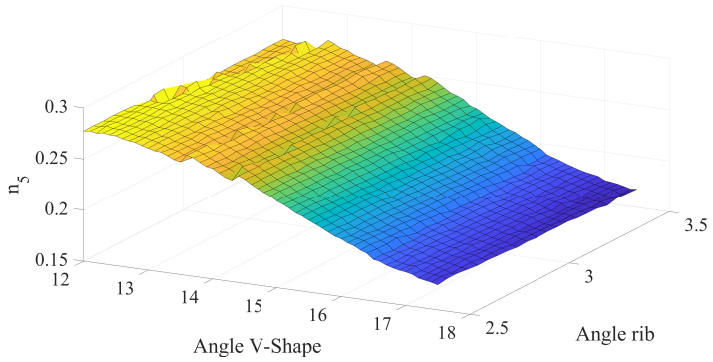

Figure 7.5: IPM V-Shape: analysis of the voltage ratio k_{V5} for different V and rib angles.

Fig. 7.5 displays the ratio between the voltage fifth and first harmonics n_{V5}. In this case, the maximum ratio n_{V5} can be obtained for low V angles. In addition, the rib angles can play a role on the n_{V5} increment, for some V angle configurations more than others.

7.3 Optimum V-Shape rotor configurations

In order to maximise the torque under the injection of the current fifth harmonic, which is based on the voltage fifth and first harmonics, the maximum ratio n_{V5} should be choice. In the same time, the ripple and average torque should be taken into the account given that their values change strongly for different rotor configurations.

Two possible rotor configurations are considered with the following constrains:

1. Torque ripple $< 30\%$; $n_{V5} > 0.27$.
2. Torque ripple $< 35\%$; $n_{V5} > 0.22$; T average $> 93Nm$.

The first rotor configuration wants to achieve the target of torque maximisation under cur-

rent fifth harmonic injection, to keep torque ripple under acceptable values and without taking into the account average torque when the machine is supplied by the only fundamental current component.

The second rotor configuration is thought to get similar torque performance of the original machine, which presents a V angle of 16.6^o and a rib angle of 2.5^o, once the current fifth harmonic is injected. In order to get this achievement a compromise on the ripple minimisation and n_{V5} maximisation is inevitable. However, this solution can guarantee a PM content reduction without affecting the torque and Joule losses.

7.3.1 Machine 1

The machine sketch is shown in Fig. 7.6 which presents a V angle of 12^o and a rib angle of 2.9^o. The stator parameters are exactly the same of the original machine (Table 6.1).

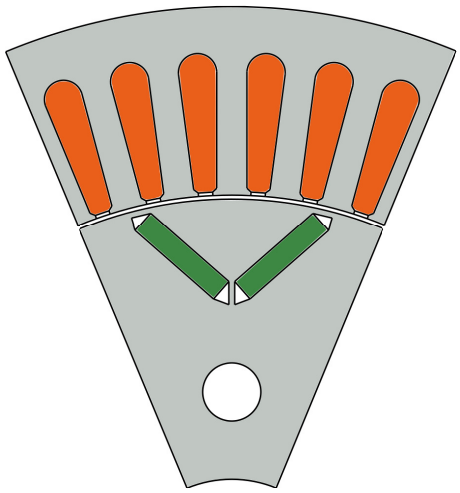

Figure 7.6: IPM V-Shape with a V angle of 12^o *and a rib angle of* 2.9^o

First of all, the validation of the computational process carried out in 7.1, where the ratio

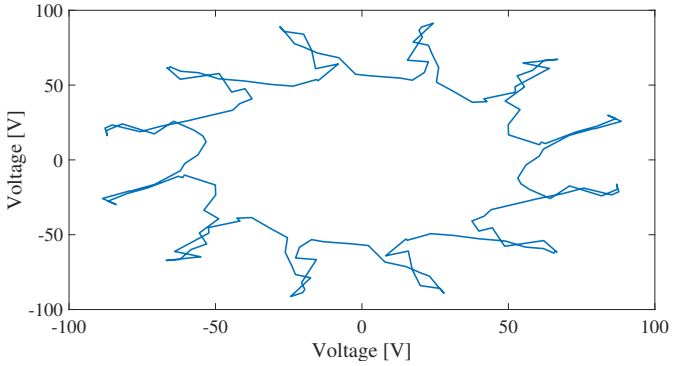

Figure 7.7: Voltage space vector 1 for the machine 1

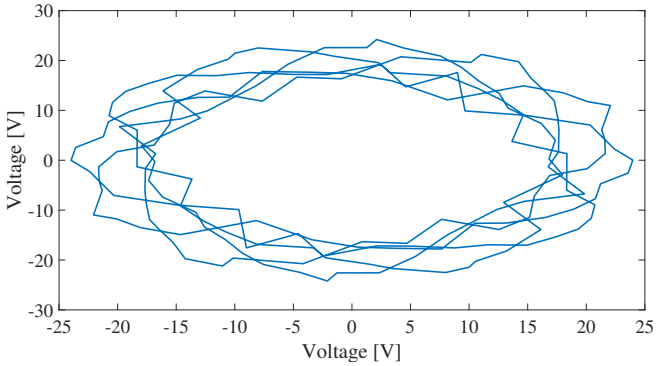

Figure 7.8: Voltage space vector 5 for the machine 1

n_{V5} was based on the FFT voltage analysis, should be done. It is not always true that the FFT and SVD analyses give the same results. Therefore, supplying the machine with a fundamental current and applying the Clarke transformation on the obtained phase voltages, it is possible to get the different harmonics in their spaces. Fig. 7.7 and 7.8 show the space vector first and fifth which permit to study the spatial voltage harmonic first and fifth in a separate way (Fig. 7.9 and 7.10). Analysing the fifth and first spatial voltage harmonics, it is possible to get a ratio $n_{V5} = 0.2729$ which is in accordance with the ratio obtained with the FFT analysis that is $n_{V5} = 0.2785$.

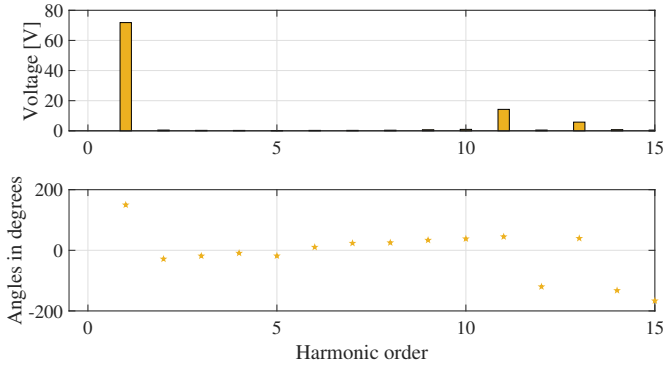

Figure 7.9: Voltage first spatial harmonic for the machine 1

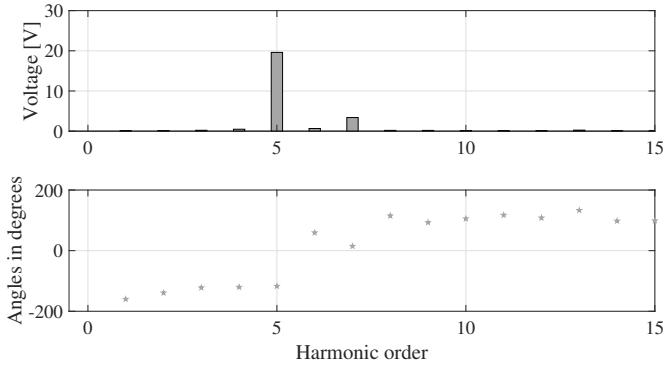

Figure 7.10: Voltage fifth spatial harmonic for the machine 1

Therefore, it is possible to affirm that the computational validation carried out in 7.1 is suitable for the proposed analyses.

Supplying the machine with a sinusoidal current amplitude $I = 71.25A$ for the initial rotor position, where the d axis is aligned with the phase A1, it is possible to get the MTPA angle which is $\alpha_1 = 122.5^o$ as shown in Fig. 7.11.

This rotor configuration presents an output average torque of 88.5 Nm and a ripple about 30%, without injection, as shown in Fig. 7.12, in accordance with the 3D graphs shown in

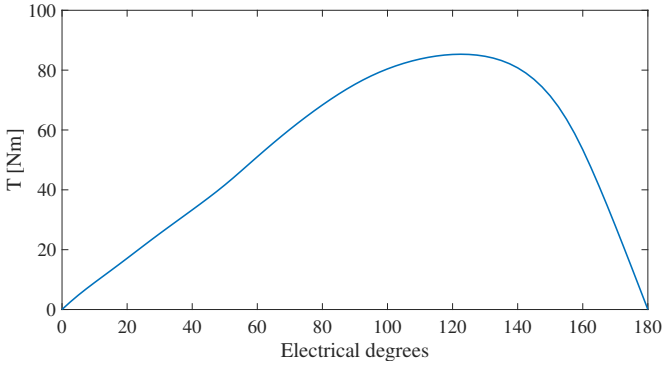

Figure 7.11: Static torque for getting the MTPA in the machine 1

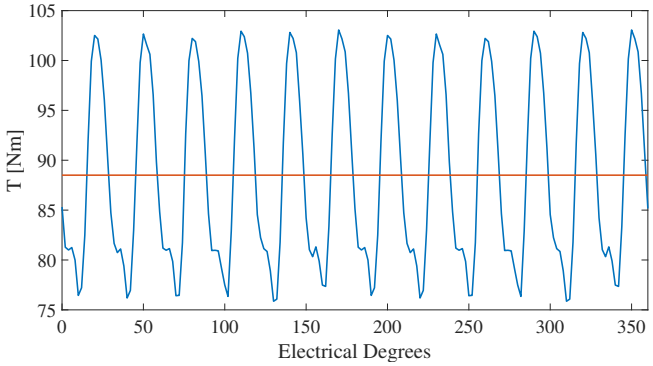

Figure 7.12: Torque ripple for the machine 1 with a sinusoidal current

Fig. 7.3 and Fig. 7.4.

The current fifth harmonic injection technique used is that one based on the voltage values (CHIV) proposed in chapter 6. Based on the equations 6.17, 6.18 and the obtained ratio $n_{V5} = 0.2729$ by SVD, the current first and fifth harmonic amplitudes are: $I1 = 68.74A$ and $I5 = 18.76A$, respectively.

The supplying current can be expressed as function of time as:

$$i(t) = I_1 sin(\omega t) + I_5 sin(5\omega t), \tag{7.2}$$

where ω is the electrical frequency.

The angle for the harmonic injection can be obtained from the voltage fifth spatial harmonic (Fig. 7.10) and it is $\alpha_{V5} = -117.1$.

The phase currents comparison between the control with the only fundamental and the fundamental + fifth harmonics is shown in Fig. 7.13, where it is possible to see that the RMS value is $I_{RMS} = 50.36$ the same for both solutions whereas the peak current is higher by 22.68% for the solution with harmonic injection, passing from 71.25 A without injection to 87.41 A with current fifth harmonic injection.

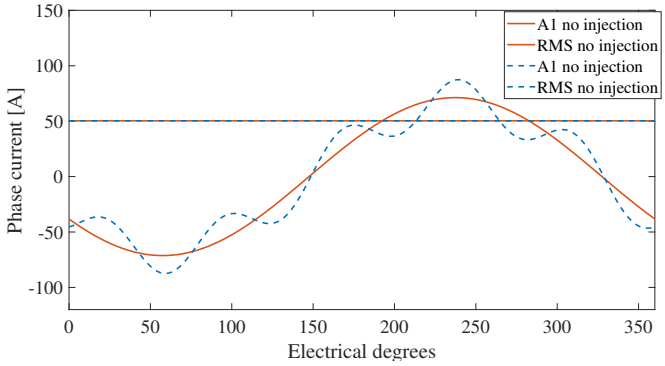

Figure 7.13: Phase current A1 comparison between the control with and without injection for the machine 1

It is worth to investigate also if the current harmonic injection affects the phase peak voltage. Fig. 7.14 shows the phase voltage A1 in both cases with and without harmonic injection.

It is possible to notice that the peak is not affect strongly by current harmonic injection, with a voltage peak value of 98.8 V without injection and 102.5 V with injection. Therefore, the voltage peak increment with the current harmonic injection is of 3.74%.

Finally, the output torque, when the machine is fed with the proposed current harmonic

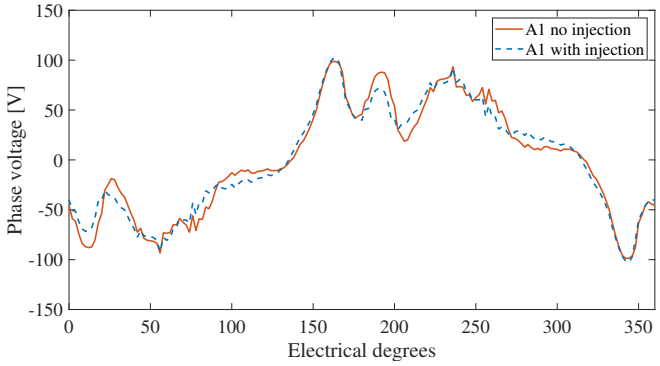

Figure 7.14: Phase voltage A1 comparison between the control with and without injection for the machine 1

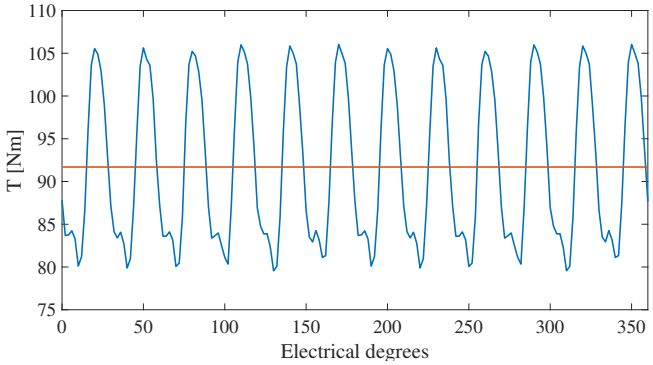

Figure 7.15: Torque ripple for the machine 1 with fifth current harmonic injection

injection technique, is shown in Fig. 7.15. It presents an average torque of 91.7 Nm and a ripple of 28.8%.

Therefore, comparing Fig. 7.12 and Fig. 7.15 it is possible to appreciate an average torque increment by 3.60% and a ripple reduction of 1.20% once the current fifth harmonic is injected.

7.3.2 Machine 2

The rotor parameters for the machine 2 are: V angle of 15.2^o and rib angle of 3.45^o. This rotor configuration presents an angle of MTPA of $\alpha_1 = 130^o$ when the machine is supplied by a sinusoidal current of $I = 71.25A$ as shown Fig. 7.16.

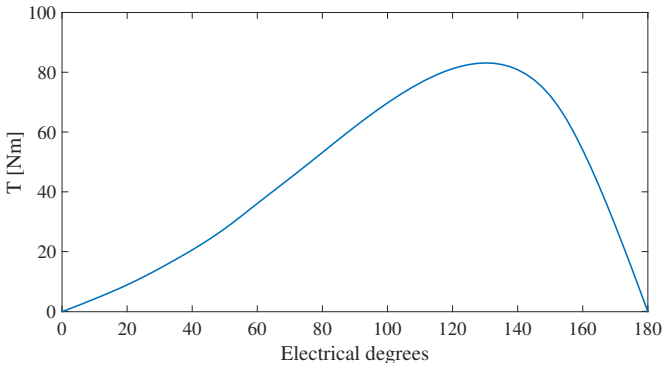

Figure 7.16: Static torque for getting the MTPA in the machine 2

Machine 2 should give an average torque about 96.5 Nm, a ripple around 30% and a ratio n_{V5} about 0.22 in accordance with figures 7.3, 7.4 and 7.5. The target is to get similar output average torque of the original machine with an important reduction of the PM content, injecting the current fifth harmonic.

Fig. 7.17 shows the two machine sketches, where is clear the PM content reduction for the machine 2. The original machine presents a PM volume of 148608 mm^3 whereas the machine 2 of 140832 mm^3, with a reduction of 5.52%. This PM reduction does not affect the average torque as shown in Fig. 7.18, where the output torque is around of 98 Nm for both configurations. In addition, it is possible to appreciate that the torque ripple for the machine 2 is 27.4% whereas it is 28.8% for the original one, with a reduction of 1.4%. The current harmonic injection technique does not affect the Joule losses given that the RMS current does not change as shown in Fig. 7.19. The current peak is slightly higher for the

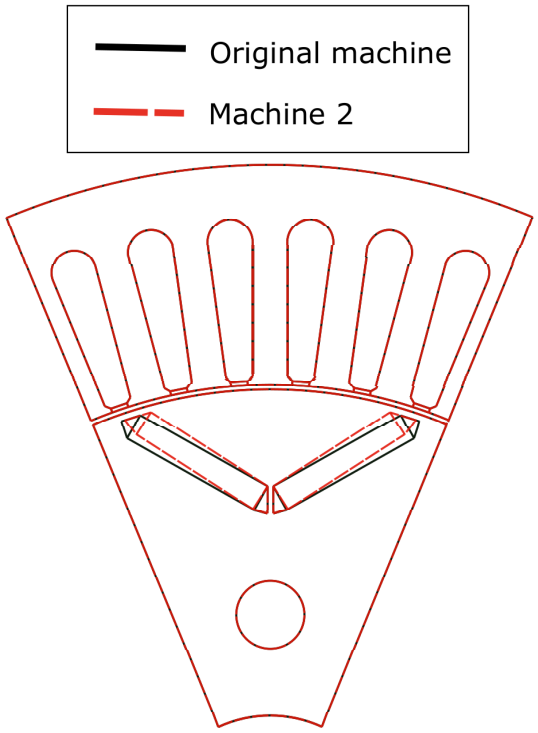

Figure 7.17: Comparison between the original machine and machine 2 rotor configurations.

control with injection by 16.25% passing from 71.25 A to 82.83 A.

The injection is done with the same formulation expressed in 7.2. In this case, The current first harmonic amplitude is I1=69.64 A and the fifth one is I5=15.08 A, based on the voltage ratio n_{V5}=0.2165 which has been obtained by the SVD applied on the phase voltages (Fig. 7.20 and 7.21). From Fig. 7.21, it is possible to get the injection angle for the current fifth harmonic which is $\alpha_5 = -142.5^o$. The considered voltage space vectors are proposed in Fig. 7.22 and 7.23.

Comparing the voltage ratio obtained by SVD n_{V5}=0.2165 and by FFT n_{V5}=0.2223, it is possible to confirm the computational process validation used in section 7.1.

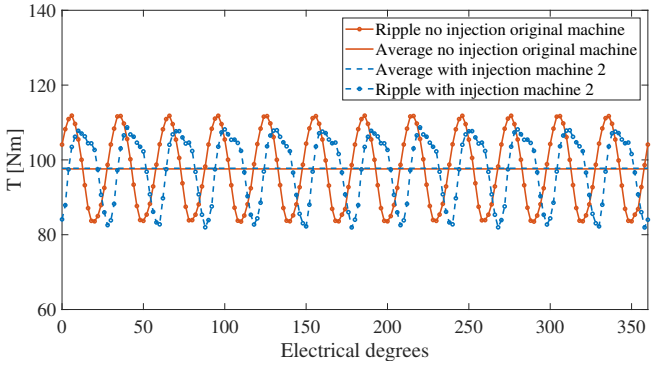

Figure 7.18: Comparison between the original machine and machine 2 average torques.

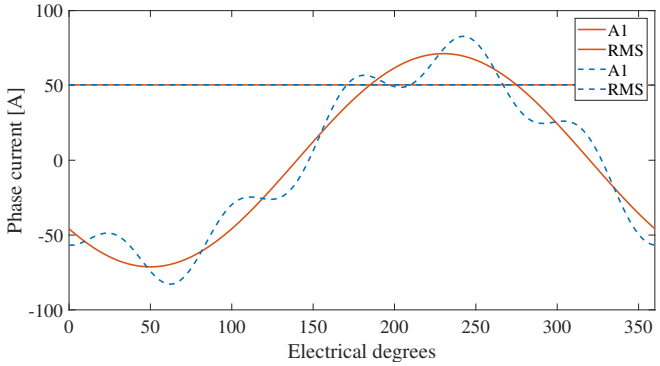

Figure 7.19: Comparison between the phase current with injection for the machine 2 and without injection for the original machine.

The phase voltage comparison is shown in Fig. 7.24, where it is possible to notice that the peaks are practically the same.

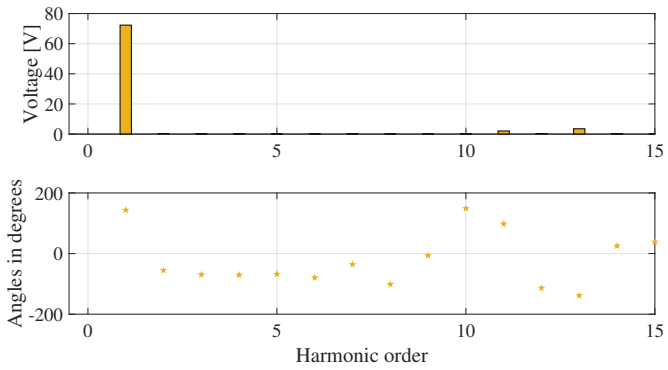

Figure 7.20: Voltage first spatial harmonic for the machine 2

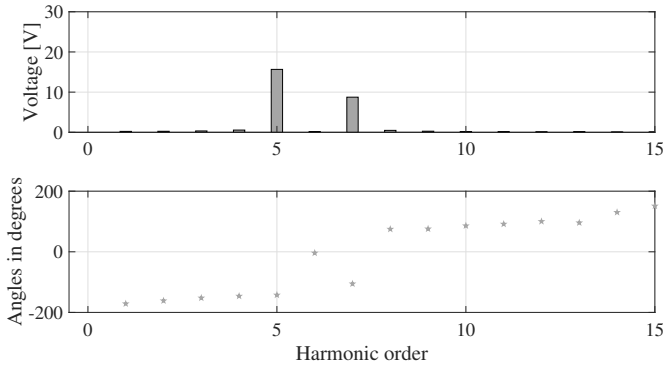

Figure 7.21: Voltage fifth spatial harmonic for the machine 2

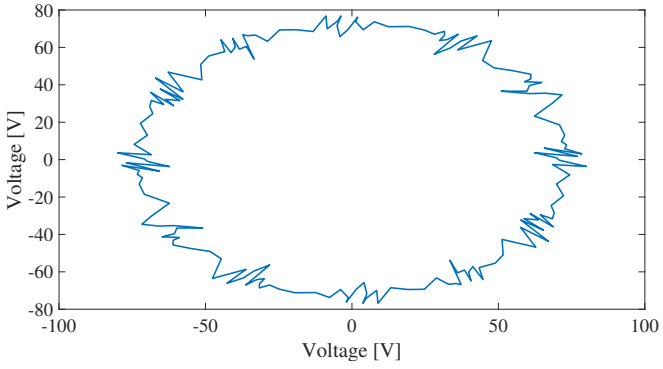

Figure 7.22: Voltage space vector 1 for the machine 2

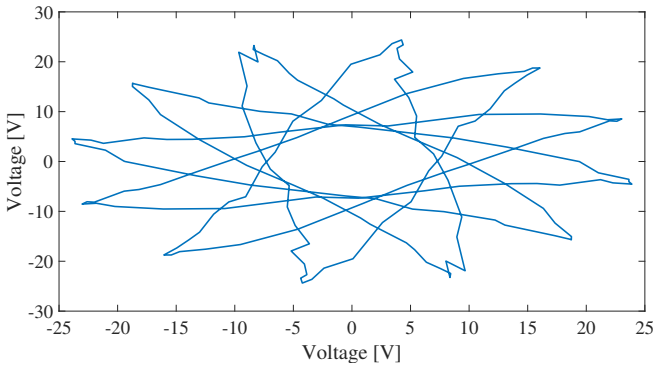

Figure 7.23: Voltage space vector 5 for the machine 2

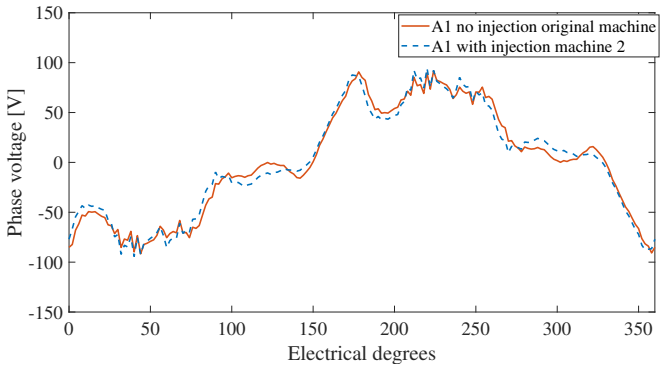

Figure 7.24: Comparison between the phase current with injection for the machine 2 and without injection for the original machine.

7.4 AC losses considerations

As well known in literature, the skin effect is the propensity of a generic AC current to be distributed not homogeneously in the conductor. Practically, it means that the current density is present with high values on the surface only and its value decreases going into the inner part of it. This phenomenon appears in particular for high frequency currents. The not uniform distribution in the conductor is linked with higher resistive losses at the same input current.

Large part of this thesis work focuses on the torque improvement by the injection of the current harmonics with an order higher than the fundamental (i.e., higher frequencies). In the major part of the proposed analyses (except in 4), the AC losses are neglected, considering ideal conductors and taking into the account the low frequencies of the additional injected harmonics.

In this section, a short explanation to justify the choice to neglect the AC losses is proposed for this particular case of study of fifth current harmonic injection.

The AC current density can be written as:

$$J = J_S e^{-(1+j)\frac{d}{\delta}}, \tag{7.3}$$

where J is the current density in a generic conductor, J_S is the current density on its surface, d is the conductor diameter and δ the skin depth. The skin depth δ is defined as the depth below the surface of a generic conductor which presents a current density value $\frac{1}{e}$ lower than the surface current density one. For the frequencies at Hz order, the skin depth δ can be written as:

$$\delta = \sqrt{\frac{2\rho}{\omega\mu}}, \tag{7.4}$$

where ρ is the resistivity of the conductor, ω the angular frequency of the current and μ the permeability of the conductor.

Therefore, the skin depth δ depends of the current frequency and material.

The skin depth δ can be re-written as:

$$\delta = \frac{1}{\sqrt{\pi f \mu \sigma}}, \tag{7.5}$$

where σ is the conductivity of the material.

Using eq. (7.5) for copper at $20^{o}C$ and a current frequency of $50Hz$, the value of skin depth is $\delta = 9.2mm$. This value is much higher with respect to the conductor diameters which are usually used for wiring the electrical machines (for example $0.250mm$). It means that for low frequencies, the skin effect is marginal and cannot not be taken into the account. It is true also for the proposed case of fifth current harmonic injection. Indeed, applying eq. (7.5) for a frequency three times higher than the fundamental $f_5 = 250Hz$, the skin depth value is $\delta = 4.1mm$, much higher of the conductors used for electrical machines.

Chapter 8

Synchronous Reluctance Machine with added Permanent Magnets

This chapter analyses the possibility to insert permanent magnets into a synchronous reluctance machine, which was originally designed with a classical three-phase configuration for washing machine applications, in order to increase the output torque.

Moreover, voltage analyses are carried out to investigate if the permanent magnets insertion can give benefits for the control with the current harmonic injection technique proposed in chapter 6.

Finally, the comparison between the original synchronous reluctance machine, arranged with a dual three-phase winding layout, and the same machine filled with permanent magnets, with and without current harmonic injection, is proposed.

Table 8.1: Synchronous reluctance machine parameters

Parameters	Values	Units
Pole pairs (p)	2	-
Slots number (N)	24	-
Winding turns (nc)	8	-
Length steak	50	mm
Outer stator diameter	102	mm
Inner stator diameter	60	mm
Slot height	11	mm
Back iron height	10	mm
Tooth width	4.5	mm
Airgap (g)	0.3	mm

8.1 Synchronous Reluctance Machine analysis

The Synchronous Reluctance (SynRel) machine under study has been designed with a three-phase distributed winding arrangement for washing machine applications, originally. The geometry is shown in Fig. 8.1 and the main parameters are listed in Table 8.1.

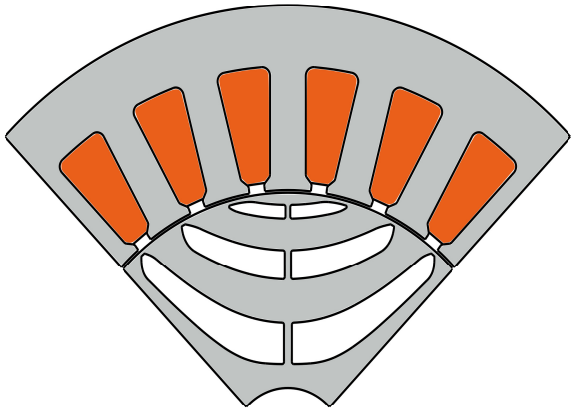

Figure 8.1: Sketch of the proposed synchronous reluctance machine.

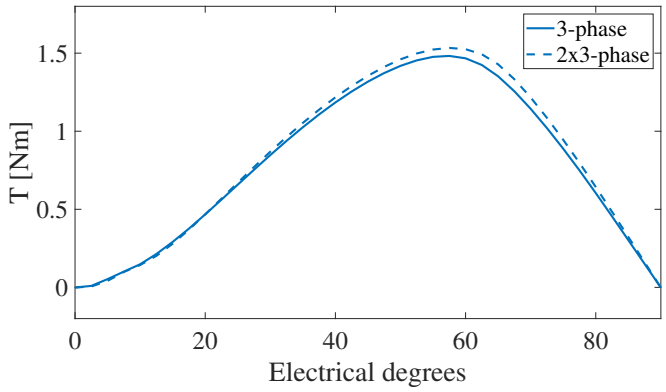

Figure 8.2: Static torque comparison between the dual three-phase winding arrangement and the three-phase one for the proposed synchronous reluctance machine.

Based on the slots and poles combination, the machine can be re-arranged with a dual three-phase distributed winding layout which presents the number of slots per pole and phase $q = 1$. As usual in order to get an improved winding factor, which deals with increased torque capability, the two three-phase subsystems are shifted between each other by $30^o el$.

The static and ripple torque comparison are carried out via FEA on both three-phase and dual three phase winding arrangements in Fig. 8.2 and 8.3, respectively.

The static torque shows the torque variation when the rotor is aligned with the magnetic axis of the phase A and A1 respectively and the current angle is changing in order to find the MTPA. In both cases the MTPA angle is $\alpha_1 = 57.5^o el$. The phase current amplitude is $I = 24.6A$ which has been obtained considering the slot fill factor $kfill = 0.45$, the current density in the slot $J = 4.65A/mm^2$ and the number conductor per slot $nc = 8$. At the MTPA angle, the torque for the dual three-phase machine is $Ts_{2x3P} = 1.55Nm$ whereas it is $Ts_{3P} = 1.48Nm$ for the three-phase one. Therefore, the machine presents an improved torque for the multi-phase machine with respect to the three-phase by 3.38% in static conditions. Using the MTPA angle $\alpha_1 = 57.5^o el$ and the phase current amplitude

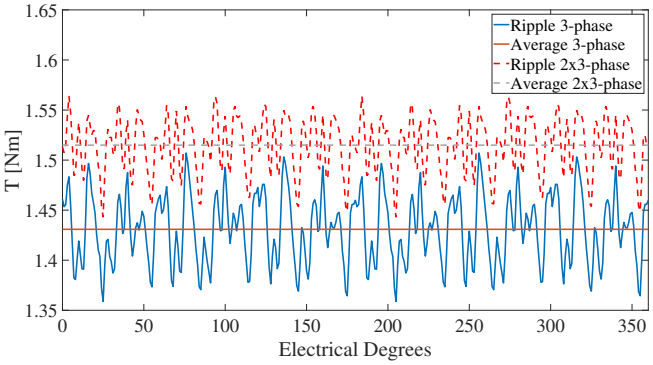

Figure 8.3: Ripple and average torque comparison between the dual three-phase winding arrangement and the three-phase one for the proposed synchronous reluctance machine.

$I = 24.6A$ for an whole rotor electrical period revolution, it is possible to get the ripple torque and its average. The comparison shows an average torque of $T_{2x3P} = 1.52Nm$ and a ripple of $Trip_{2x3P} = 8.0\%$ for the multi-phase machine whereas the average torque is $T_{3P} = 1.43Nm$ and the ripple is $Trip_{3P} = 10.3\%$ for the three-phase one. Therefore, The multi-phase machine presents an higher torque by 6.3% and a lower ripple by -2.3%.

The dual three-phase average torque presents an increment due to an improved winding factor of the fundamental component which passes from 0.9659 to 1. The ripple is reduced thanks to the fact that the dual three-phase machine does not present the 5^{th} and 7^{th} in the stator magneto-motive force, so that the 6^{th} of torque is not generated (Fig. 8.4).

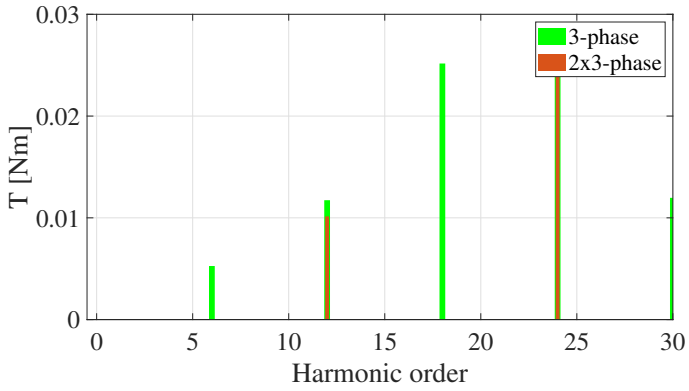

Figure 8.4: FFT torque comparison between the dual three-phase winding arrangement and the three-phase one for the proposed synchronous reluctance machine.

8.2 Synchronous Reluctance Machine with added Permanent Magnets analysis

Synchronous Reluctance machines are designed with the idea to use the different reluctances of the d-q axes to generate torque. The independence from magnets permits to have machines more reliable and less expensive with respect to the PM machines, with the possibility to reach higher speed.

Filling part of the machine barriers with PM magnets permits to increase some voltage harmonics to control the machine with high order current harmonics in addition to the fundamental for an improved torque capability with respect to the PM insertion only. Indeed, the voltage analysis of the multi-phase SynRel machine shows that the amplitudes of the harmonics with an order higher than the fundamental are too low to permit a torque increment by current harmonic injection (Fig. 8.5).

The main constrain for the PM filling barrier is given from the manufacturing point of view. Indeed, the permanent magnets will be produced by a 3D printer in collaboration with the

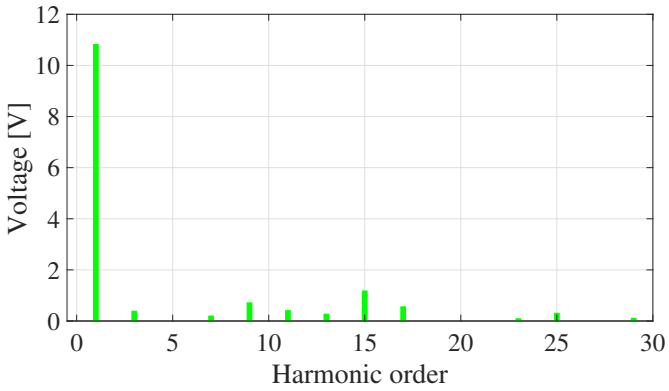

Figure 8.5: FFT voltage analysis of the phase A1 for the proposed dual three-phase synchronous reluctance machine.

advanced and manufacturing department. Therefore, the unique barrier which can be filled by PM is the biggest one at the bottom of the rotor (closest part to the shaft).

The following sections investigate the possibility to enhance the torque by current harmonic injection thanks to the increment of third harmonic voltage in the machine given by the PM insertion.

8.2.1 FEA: computational process and result discussion

The computational process starts to upload one pole of the machine geometry which presents the two bottom flux barriers filled with PM as shown in Fig. 8.6.

The PM are made by rare earth (NdFeB) which presents the B-H characteristic shown in Fig. 8.7.

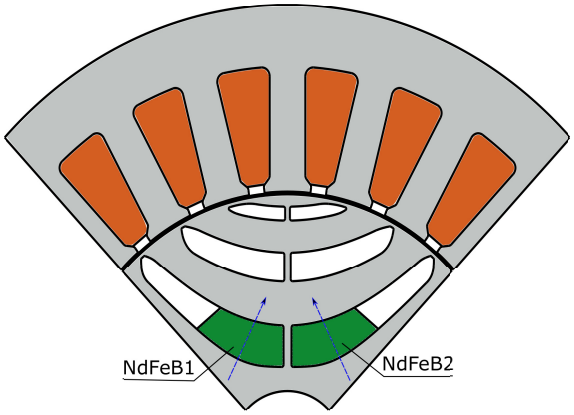

Figure 8.6: Magnetisation direction of permanent magnets.

From the B-H curve, it is possible to calculate the relative permeance flux as:

$$\mu_r = tan^{-1}(\frac{B_r}{H_{ci}}), \tag{8.1}$$

where B_r is the relative flux density and H_{ci} is the coercivity field.

Therefore, the PM permeability can be calculate as:

$$\mu_{PM} = \frac{\mu_r}{\mu_0}. \tag{8.2}$$

Considering that $\mu_0 = 4\pi * 10^{-7} H/m$ and $\mu_r = 1.8786 * 10^{-6} H/m$, the PM permeability is $\mu_{PM} = 1.495$.

At this point, the direction of magnetisation varies through a for cycle. The following procedure presents the same concept of the computational process presented in the section 7.1. In this case, the considered voltage harmonic is the third in order to permit a torque improvement by the third current harmonic injection. The computational procedure is shown in Fig. 8.8. The parameter "c" works on the direction of magnetisation, subtracting/adding its value to the radial direction. Therefore, the PM direction of magnetisation is analysed between $50^o el$ and $130^o el$.

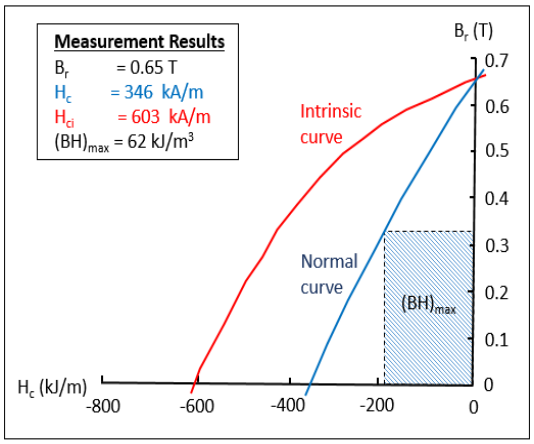

Figure 8.7: B-H curve of the PM available for the 3D printing by advanced manufacturing department.

The ratio between the voltage third harmonic and the first one n_3 is shown in Fig. 8.9 where it is possible to appreciate that the maximum value of the ratio n_3 is for $c = -23$.

The parameters $c = -23$ is also the optimum option in terms of average torque for the proposed machine as shown in Fig. 8.10.

It seems worth to investigate how the ripple can be affected due to the PM insertion. From Fig. 8.11, it is possible to understand that the ripple is huge with respect to the original pure SynRel machine. It is understandable given that the original machine was designed without the permanent magnets. Therefore, a new flux barrier optimization should be done in order to reduce the ripple of the new machine. However, it is not the target of this thesis. It seems clear that the optimum solution to increase the average torque and the ratio n_3 is for the parameter $c = -23$. It means that the magnets have a magnetisation direction of $NdFeB1 = 113^o$ and $NdFeB2 = 67^o$, respectively as shown in Fig. 8.6.

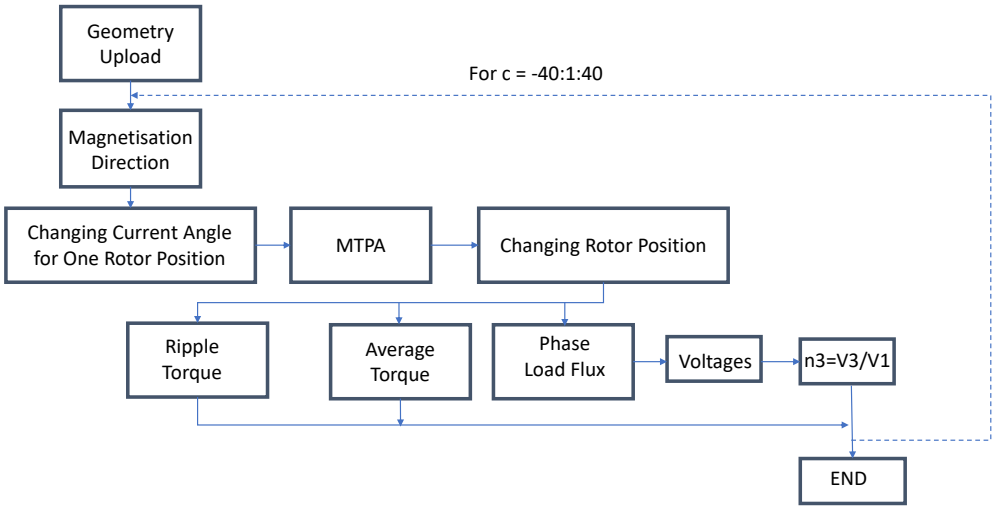

Figure 8.8: Workflow chart of the proposed computational process to enhance the voltage fifth harmonic in a dual three-phase IPM V-Shape machine.

In order to find the correct angle for the injection the space vector decomposition (SVD) theory should be applied to the phase voltages as chapter 6 suggests. Moreover, once the SVD is applied on the voltages, it is possible to validate the computational process to match the ratio n_3 obtained with the FFT and SVD for the optimum rotor configuration. Analysing Fig. 8.12, it is possible to see that the angle injection for the third harmonic is $\alpha_3 = 173^o el$ and the ratio between the voltage third and fundamental harmonics is $n_3 = 0.329$. Comparing n_3 obtained with the FFT ($n_3 = 0.327$) and SVD, it is possible to affirm that the results are practically the same, so that the proposed computational process can be considered validated.

It is worth to notice that in the voltage ratio n_3 (see Fig 8.9) and ripple torque (see Fig. 8.11) there is a discontinuity in correspondence to point $c = +28$. This phenomenon can be due to the fact that $c = +28$ is the first point for which the direction of the magnets does

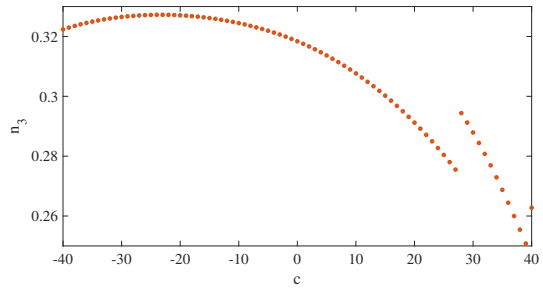

Figure 8.9: Ratio between the voltage third and first harmonics of the proposed synchronous reluctance machine filled with permanent magnet.

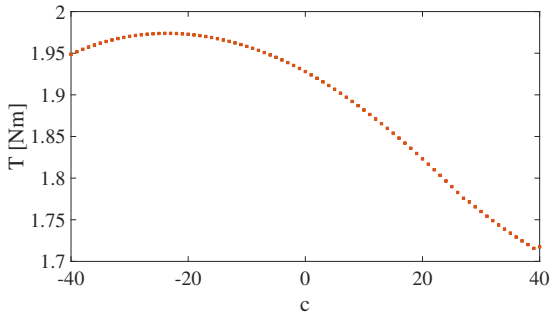

Figure 8.10: Average torque of the proposed synchronous reluctance machine filled with permanent magnet.

not cross the second flux barrier (the middle one) (See Fig. 8.13).

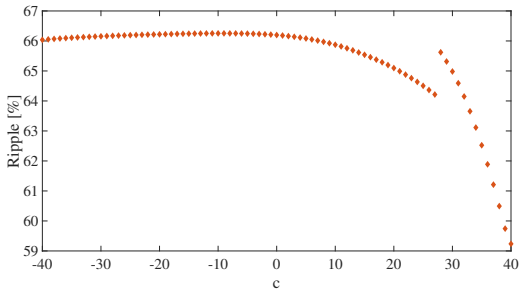

Figure 8.11: Torque ripple of the proposed synchronous reluctance machine filled with permanent magnet.

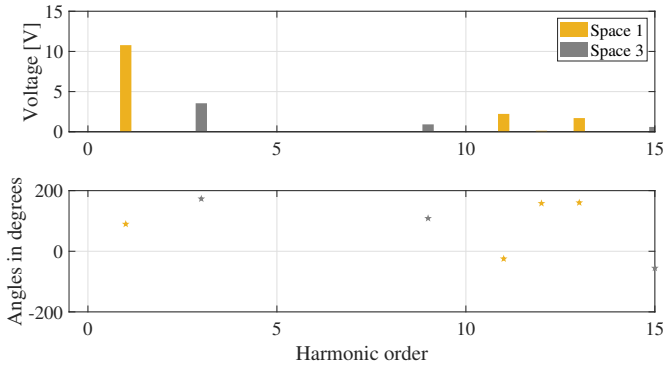

Figure 8.12: Voltage spaces 1 and 5 for the proposed SynRel with PM under a fundamental phase current $I = 24.6A$.

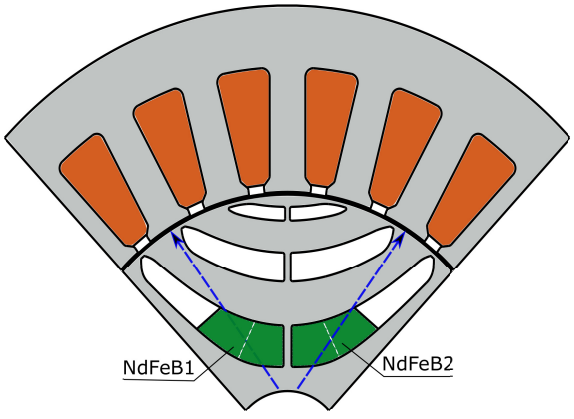

Figure 8.13: Magnetisation direction of permanent magnets for the value c=+28.

8.3 Comparison

Analysing the dual three-phase machine, it is possible to notice an average torque improvement by 30.3% thanks to PM insertion as shown Fig. 8.14, passing from $1.52Nm$ to $1.98Nm$. From the same figure, it is possible to notice an additional torque improvement thanks to the current third harmonic injection by 6.06% with respect to the solution with PM and only fundamental current, passing from $1.98Nm$ to $2.10Nm$. Therefore, the machine torque capability increment is of 36.36% with respect to the original pure SynRel. As already mentioned in the subsection 8.2.1, the PM insertion makes the machine without a real applicability due to the huge ripple.

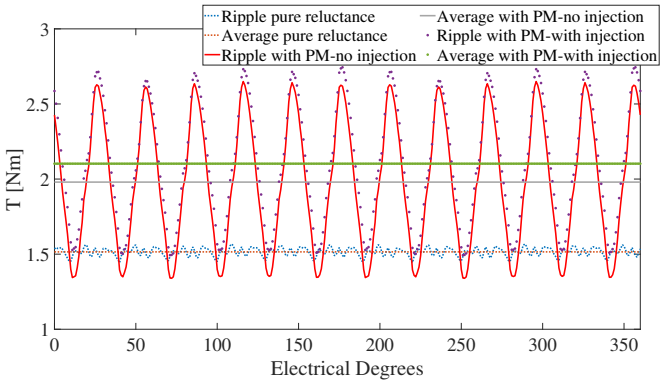

Figure 8.14: Torque comparison for the proposed machine with and without PM and with and without harmonic injection.

The proposed third current harmonic injection technique forces the system to keep constant the RMS current value (i.e., Joule losses) by the following equations:

$$I_1 = \frac{I}{\sqrt{1+n_3^2}} \tag{8.3}$$

$$I_3 = \frac{I}{\sqrt{1+n_3^2}} n_3 \tag{8.4}$$

where I is the original fundamental current amplitude, I_1 the new fundamental current amplitude, I_3 the third harmonic current amplitude and n_3 the voltage ratio obtained by SVD. Therefore, the machine is supplied with the phase current:

$$i(t) = I_1 sin(\omega t) + I_3 sin(3\omega t), \tag{8.5}$$

where ω is the electrical frequency.

The d-axis of the d-q reference frame is aligned with the phase A1. The fundamental current is injected with the MTPA angle $\alpha_1 = 57.5^o el$ and the third harmonic component with $\alpha_3 = 173.1^o el$ which has been obtained applying the SVD on the phase voltages. The phase current is shown in Fig. 8.15 with and without third current harmonic injection. It is possible to appreciate that the RMS value is exactly the same $I_{rms} = 17.37A$ whereas the peak is higher of 25.6% for the control with current harmonic injection passing from $I_{peak} = 24.59A$ to $I_{peak} = 30.88A$. Therefore, the switches of the inverter might need to be oversized.

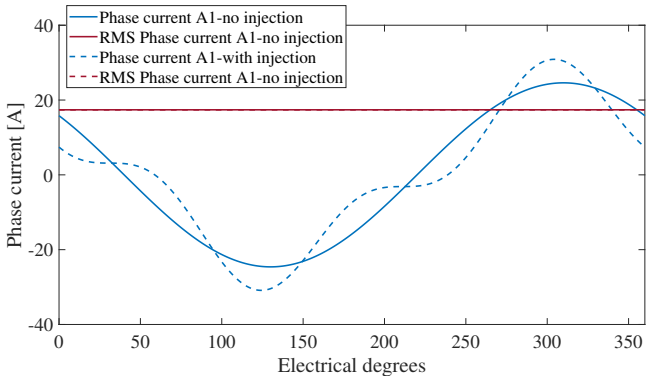

Figure 8.15: phase current A1 with and without third harmonic injection.

8.4 Conclusions

In this chapter, the possibility to insert PM in part of the barriers of a synchronous reluctance machine in order to increase the torque capability by current harmonic injection is proposed. A PM magnetisation direction sensitivity analysis is carried out to maximise the average torque and the ratio between the voltage third and fundamental harmonics. Injecting the third harmonic in the proposed dual three-phase machine, it has been shown an important increment in terms of machine torque capability. However, the PM insertion affects strongly the machine torque ripple. Therefore, rotor flux barriers optimization should be carried out in order to make the machine suitable for real applications.

Chapter 9

Conclusions

This work is focused on the analysis of multi-phase machines and the identification of ways to improve their torque production capability. A number of motor topologies have been investigated to assess pros and cons of the current harmonic injection in different rotor structures.

First of all, the electromagnetic behaviour in terms of flux density distribution in a classical three-phase distributed winding SPM machine was carried out with a simplified analytical model. The findings highlight the advantage of the multi-phase machines with respect to the three-phase ones, which consists in a symmetrical flux density distribution in the stator core. A possible solution to balance the asymmetrical flux density in three-phase machines was proposed with an asymmetrical stator teeth geometry. The mentioned solution allows to get a uniform machine saturation for three-phase machines as well without affecting the torque average and ripple.

Particular focus has been given to the study of distributed winding V-Shape IPM machines

where the increment of the average torque and the reduction of the ripple was obtained by re-configuring the classical three-phase winding arrangement as a dual three-phase one. The macro improvements are given by an improved winding factor and magneto-motive force distribution. It has been shown, on the machine under investigation, how the average torque was increased by about 4%, with a torque ripple reduction of about 11%. In this analysis is mentioned the possibility to reduce the machine volume passing from 110 mm to 106.3 mm, getting a lighter machine by 1.10 kg, to keep the same output torque thanks to the multi-phase re-arrangement. In order to take under considerations the flux density distribution asymmetries in the three-phase machine, a particular iron losses calculation approach is proposed which uses the Steinmetz's equation considering the peak flux density in the teeth, based on the number of slots per pole and phase q. For example, the case of study presented $q = 2$, so that the peak of flux densities in two teeth in a row are considered. Finally, the total iron losses are calculated with a multiplication which considered the half slots number.

In addition, a comparison between a classical three-phase and dual three-phase dual rotor fractional slots Halbach array machine was carried out considering the current third harmonic injection, while maintaining a constant current peak value. In this case, the state-of-art approach is proposed on a particular machine topology. This led to an improved average torque as a consequence of an increased RMS current injected in the machine, which translates in higher Joule losses with a partial contribution of the AC losses component (+38.91%). The comparison shows similar improvements in terms of increased torque percentage between the two winding configurations by 11.22% and 9.57% for the three-phase and dual three-phase, respectively.

An important part of this thesis was dedicated to increase the average torque and/or reduce the PM content, within the rotor structures, on multi-phase SPM machine with a multi-harmonic current injection (keeping constant the RMS current). The proposed analytical model has shown a good match with the FEA results, confirming the validity of the model.

This analysis can give important information to the design engineers whom can select the best PM percentage on the rotor surface based on the selected harmonics for the control. For example, if the control is implemented to inject into the machine the fundamental + fifth harmonics of current, the optimum PM span results 60%. Moreover, for the mentioned case of study, it has been shown that to apply the current harmonic injection technique in the flux weakening region is not suitable in which for an improved torque there is a decrement of speed with a reduction of the its range. Therefore, it contrasts with the target to operate over the MTPA point, which is to reach higher speed.

A model-free current harmonic injection technique for improving the average torque was studied and developed. This has shown good performance on both anisotropic and isotropic machines, and has the potential to be applied on-line. Indeed, the proposed technique was based on the load voltage vectors for the current harmonic injection, which can be easily measured from the board directly. An experimental setup has been developed to test and validate the proposed concept. It has been carried out on a dual three-phase V-Shape IPM machine available in the Power Electronics, Machines and Control (PEMC) research group. In addition, the analysis has been shown that the state-of-art solution for the SPM machine based on the back electro-motive force values cannot be applied on IPM topology ones. Both mentioned techniques are compared with a benchmark carried out by FEA. However, the anisotropic machine under study presented a rotor structure not optimal to inject the fifth harmonic in which this last was too low. Indeed, the proposed IPM machine presented an improved torque by 1.13% only thanks to the proposed current harmonic injection technique (same performance of the benchmark).

Therefore, Based on the technique described above, a sensitivity analysis on the possible rotor configurations to improve the torque density under fifth current harmonic injection on a V-Shape IPM machine was proposed. Two main configurations are highlighted in detail. One aims to maximise the torque under fifth harmonic injection, the other one wants to reduce the PM content in the original machine without affecting the torque performance.

The first one displayed an output torque increment by 3.60% with respect to the control without injection. The second one reduced by 5.60% the PM content into the machine, against the original V-Shape IPM motor, thanks to the injection.

The last part of this thesis was dedicated to study the possibility to fill with additive material permanent magnets the bottom flux barriers in multi-phase synchronous reluctance machines. The possibility to have an additional torque improvement thanks to the third current harmonic injection was proposed. In order to optimise the performance under third current harmonic injection control, a magnetisation direction sensitivity analysis was carried out. The final output torque was higher by 36.36% with respect to the original machine. However, the huge torque ripple due to the PM insertion does not permit to have a real application without a flux barriers re-designing.

Bibliography

[1] E. Levi, R. Bojoi, F. Profumo, H. A. Toliyat, and S. Williamson, "Multiphase induction motor drives - a technology status review," IET Electric Power Applications, vol. 1, pp. 489-516, 2007.

[2] J. S. Thongam, M. Tarbouchi, A. F. Okou, D. Bouchard, and R. Beguenane, "Trends in naval ship propulsion drive motor technology," in 2013 IEEE Electrical Power & Energy Conference, 2013, pp. 1-5.

[3] L. Parsa and H. A. Toliyat, "Five-phase permanent magnet motor drives for ship propulsion applications," in IEEE Electric Ship Technologies Symposium, 2005., 2005, pp. 371-378.

[4] J. Dai, S. W. Nam, M. Pande, and G. Esmaeili, "Medium-Voltage Current-Source Converter Drives for Marine Propulsion System Using a Dual-Winding Synchronous Machine," IEEE Transactions on Industry Applications, vol. 50, pp. 3971-3976, 2014.

[5] F. Scuiller, J. F. Charpentier, and E. Semail, "Multi-star multi-phase winding for a high power naval propulsion machine with low ripple torques and high fault tolerant ability," in 2010 IEEE Vehicle Power and Propulsion Conference, 2010, pp. 1-5.

[6] C. Bassi, A. Tessarolo, R. Menis, and G. Sulligoi, "Analysis of different system design solutions for a high-power ship propulsion synchronous motor drive with multiple PWM

converters," in Electrical Systems for Aircraft, Railway and Ship Propulsion, 2010, pp. 1-6.

[7] B. Gamble, G. Snitchler, and T. MacDonald, "Full Power Test of a 36.5 MW HTS Propulsion Motor," IEEE Transactions on Applied Superconductivity, vol. 21, pp. 1083-1088, 2011.

[8] M. Taha, J. Wale, and D. Greenwood, "Design of a high power-low voltage multiphase permanent magnet flux switching machine for automotive applications," in 2017 IEEE International Electric Machines and Drives Conference (IEMDC), 2017, pp. 1-8.

[9] A. Cavagnino, A. Tenconi, and S. Vaschetto, "Experimental Characterization of a Belt-Driven Multiphase Induction Machine for 48-V Automotive Applications: Losses and Temperatures Assessments," IEEE Transactions on Industry Applications, vol. 52, pp. 1321-1330, 2016.

[10] M. Slunjski, O. Dordevic, M. Jones and E. Levi, "Symmetrical/Asymmetrical Winding Reconfiguration in Multiphase Machines," in IEEE Access, vol. 8, pp. 12835-12844, 2020, doi: 10.1109/ACCESS.2020.2965652.

[11] L. Parsa, "On advantages of multi-phase machines," in 31st Annual Conference of IEEE Industrial Electronics Society, 2005. IECON 2005., 2005, p. 6 pp.

[12] G. Sala, "MULTIPHASE ELECTRIC DRIVES FOR "MORE ELECTRIC AIRCRAFT" APPLICATIONS", Ph.D Thesis, University of Bologna.

[13] A. Tani, M. Mengoni, L. Zarri, G. Serra, and D. Casadei, "Control of Multiphase Induction Motors With an Odd Number of Phases Under Open-Circuit Phase Faults," IEEE Transactions on Power Electronics, vol. 27, pp. 565-577, 2012.

[14] R. Hyung-Min, K. Ji-Woong, and S. Seung-Ki, "Synchronous-frame current control of multiphase synchronous motor under asymmetric fault condition due to open phases," IEEE Transactions on Industry Applications, vol. 42, pp. 1062-1070, 2006.

[15] H. S. Che, M. J. Duran, E. Levi, M. Jones, W. P. Hew, and N. A. Rahim, "Postfault Operation of an Asymmetrical Six-Phase Induction Machine With Single and Two Isolated Neutral Points," IEEE Transactions on Power Electronics, vol. 29, pp. 5406-5416, 2014.

[16] M. Mengoni, G. Sala, L. Zarri, A. Tani, G. Serra, Y. Gritli, et al., "Control of a fault-tolerant quadruple three-phase induction machine for More Electric Aircrafts," in IECON 2016 - 42nd Annual Conference of the IEEE Industrial Electronics Society, 2016, pp. 5747-5753.

[17] G. Sala, G. Valente, A. Formentini, L. Papini, D. Gerada, P. Zanchetta, et al., "Space Vectors and Pseudo Inverse Matrix Methods for the Radial Force Control in Bearingless Multi-Sector Permanent Magnet Machines," IEEE Transactions on Industrial Electronics, 2017.

[18] A. Tani, L. Zarri, M. Mengoni, G. Serra, and D. Casadei, "Detection and localization of high resistance connections in quadruple three-phase induction motor drives," in 2014 International Conference on Electrical Machines (ICEM), 2014, pp. 2094-2100.

[19] W. Zhao, C. Gu, Q. Chen, J. Ji, and D. Xu, "Remedial phase-angle control of a five-phase fault-tolerant permanent-magnet vernier machine with short-circuit fault," CES Transactions on Electrical Machines and Systems, vol. 1, pp. 83-88, 2017.

[20] X. Wang, X. Ren, and J. Y. Zhang, "Short-circuit fault-tolerant control of bearingless permanent magnet slice machine," in 2013 IEEE Energy Conversion Congress and Exposition, 2013, pp. 1148-1153.

[21] S. Dwari and L. Parsa, "Optimum Fault-Tolerant Control of Multi-phase Permanent Magnet Machines for Open-Circuit and Short-Circuit Faults," in APEC 07 - Twenty-Second Annual IEEE Applied Power Electronics Conference and Exposition, 2007, pp. 1417-1422.

[22] R. Bojoi, A. Cavagnino, A. Tenconi, A. Tessarolo and S. Vaschetto, "Multiphase electrical machines and drives in the transportation electrification," 2015 IEEE 1st International Forum on Research and Technologies for Society and Industry Leveraging a better tomorrow (RTSI), 2015, pp. 205-212, doi: 10.1109/RTSI.2015.7325099.

[23] R. O. C. Lyra and T. A. Lipo, "Torque density improvement in a six-phase induction motor with third harmonic current injection," IEEE Transactions on Industry Applications, vol. 38, pp. 1351-1360, 2002.

[24] H. A. Toliyat, S. P. Waikar, and T. A. Lipo, "Analysis and simulation of five-phase synchronous reluctance machines including third harmonic of airgap MMF," IEEE Transactions on Industry Applications, vol. 34, pp. 332-339, 1998.

[25] X. Huangsheng, H. A. Toliyat, and L. J. Petersen, "Five-phase induction motor drives with DSP-based control system," IEEE Transactions on Power Electronics, vol. 17, pp. 524-533, 2002.

[26] K. Wang, Z. Q. Zhu, Y. Ren and G. Ombach, "Torque Improvement of Dual Three-Phase Permanent-Magnet Machine With Third-Harmonic Current Injection," in IEEE Transactions on Industrial Electronics, vol. 62, no. 11, pp. 6833-6844, Nov. 2015, doi: 10.1109/TIE.2015.2442519.

[27] Z. Y. Gu, K. Wang, Z. Q. Zhu, Z. Z. Wu, C. Liu and R. W. Cao, "Torque Improvement in Five-Phase Unequal Tooth SPM Machine by Injecting Third Harmonic Current," in IEEE Transactions on Vehicular Technology, vol. 67, no. 1, pp. 206-215, Jan. 2018, doi: 10.1109/TVT.2017.2771752.

[28] J. Wang, R. Qu and L. Zhou, "Dual-Rotor Multiphase Permanent Magnet Machine With Harmonic Injection to Enhance Torque Density," in IEEE Transactions on Applied Superconductivity, vol. 22, no. 3, pp. 5202204- 5202204, June 2012, Art no. 5202204, doi: 10.1109/TASC.2011.2179399.

[29] Y. Hu, Z. Q. Zhu and M. Odavic, "Torque Capability Enhancement of Dual Three-Phase PMSM Drive With Fifth and Seventh Current Harmonics Injection," in IEEE Transactions on Industry Applications, vol. 53, no. 5, pp. 4526-4535, Sept.-Oct. 2017, doi: 10.1109/TIA.2017.2707330.

[30] A. Cervone, M. Slunjski, E. Levi and G. Brando, "Optimal Third-Harmonic Current Injection for Asymmetrical Multiphase Permanent Magnet Synchronous Machines," in IEEE Transactions on Industrial Electronics, vol. 68, no. 4, pp. 2772-2783, April 2021, doi: 10.1109/TIE.2020.2982099.

[31] M. Farshadnia, M. A. Masood Cheema, A. Pouramin, R. Dutta and J. E. Fletcher, "Design of Optimal Winding Configurations for Symmetrical Multiphase Concentrated-Wound Surface-Mount PMSMs to Achieve Maximum Torque Density Under Current Harmonic Injection," in IEEE Transactions on Industrial Electronics, vol. 65, no. 2, pp. 1751-1761, Feb. 2018, doi: 10.1109/TIE.2017.2745464.

[32] M. Slunjski, O. Stiscia, M. Jones and E. Levi, "General Torque Enhancement Approach for a Nine-Phase Surface PMSM with Built-in Fault Tolerance," in IEEE Transactions on Industrial Electronics, doi: 10.1109/TIE.2020.3007053.

[33] K. Zhang, G. -J. Li, Z. Q. Zhu and G. Jewell, "Impact of Current Harmonic Injection on Performance of Multi-Phase Synchronous Reluctance Machines," in IEEE Transactions on Energy Conversion, doi: 10.1109/TEC.2020.3041252.

[34] G. Feng, C. Lai, M. Kelly and N. C. Kar, "Dual Three-Phase PMSM Torque Modeling and Maximum Torque per Peak Current Control Through Optimized Harmonic Current Injection," in IEEE Transactions on Industrial Electronics, vol. 66, no. 5, pp. 3356-3368, May 2019, doi: 10.1109/TIE.2018.2854550.

[35] G. J. Li, K. Zhang, Z. Q. Zhu and G. W. Jewell, "Comparative Studies of Torque Performance Improvement for Different Doubly Salient Synchronous Reluctance Machines

by Current Harmonic Injection," in IEEE Transactions on Energy Conversion, vol. 34, no. 2, pp. 1094-1104, June 2019, doi: 10.1109/TEC.2018.2870753.

[36] K. Zhang, G. Li, Z. Q. Zhu and G. W. Jewell, "Analytical Modeling of Dynamic Performance with Harmonic Current Injection for Doubly Salient Synchronous Reluctance Machines," in IEEE Transactions on Industry Applications, vol. 56, no. 4, pp. 3477-3487, July-Aug. 2020, doi: 10.1109/TIA.2020.2982858.

[37] J. Feng, L. Huang, Z. Q. Zhu, S. Guo and J. Shi, "Torque Density Enhancement of 6/4 Variable Flux Reluctance Machine With Second-Harmonic Current Injection," in IEEE Transactions on Energy Conversion, vol. 34, no. 2, pp. 1135-1145, June 2019, doi: 10.1109/TEC.2018.2886004.

[38] W. Kong, R. Qu, M. Kang, J. Huang and L. Jing, "Air-Gap and Yoke Flux Density Optimization for Multiphase Induction Motor Based on Novel Harmonic Current Injection Method," in IEEE Transactions on Industry Applications, vol. 53, no. 3, pp. 2140-2148, May-June 2017, doi: 10.1109/TIA.2017.2670519.

[39] L. Huang, Z. Q. Zhu, J. Feng, S. Guo and J. X. Shi, "Feasible Stator/Rotor Pole Combinations of Variable Flux Reluctance Machines With Second Harmonic Current Injection Method," in IEEE Transactions on Industry Applications, vol. 56, no. 5, pp. 4785-4795, Sept.-Oct. 2020, doi: 10.1109/TIA.2020.3002879.

[40] V. Madonna, A. Walker, P. Giangrande, G. Serra, C. Gerada, and M. Galea, "Improved thermal management and analysis for stator end-windings of electrical machines," IEEE Transactions on Industrial Electronics, vol. 66, no. 7, pp. 5057–5069, July 2019.

[41] F. Chai, P. Liang, Y. Pei, and S. Cheng, "Magnet shape optimization of surface-mounted permanent-magnet motors to reduce harmonic iron losses," IEEE Transactions on Magnetics, vol. 52, no. 7, pp. 1–4, July 2016.

[42] S. N. Shafiqin, N. H. Halim, I. Daut, Y. Yanawati, M. Asri, M. Dina, N. Gomesh, I. Pungut, M. Abdullah, and M. N. Syatirah, "Predicting the localized flux distribution in

three phase induction motor between different stator slot size," in 2011 5th International Power Engineering and Optimization Conference, June 2011, pp. 197–201.

[43] A. Al-Timimy, G. Vakil, M. Degano, P. Giangrande, C. Gerada, and M. Galea, "Considerations on the effects that core material machining has on an electrical machine's performance," IEEE Transactions on Energy Conversion, vol. 33, no. 3, pp. 1154–1163, Sep. 2018.

[44] Z. Q. Zhu, D. Howe, and C. C. Chan, "Improved analytical model for predicting the magnetic field distribution in brushless permanent magnet machines," IEEE Transactions on Magnetics, vol. 38, no. 1, pp. 229–238, Jan 2002.

[45] L. J. Wu, Z. Q. Zhu, D. Staton, M. Popescu, and D. Hawkins, "An improved subdomain model for predicting magnetic field of surfacemounted permanent magnet machines accounting for tooth-tips," IEEE Transactions on Magnetics, vol. 47, no. 6, pp. 1693–1704, June 2011.

[46] L. Branz, M. Bortolozzi, and A. Tessarolo, "Analytical calculation of the no-load flux density in the stator core of slotless spm machines," in 2013 International Conference-Workshop Compatibility And Power Electronics, June 2013, pp. 244–249.

[47] V. Madonna, P. Giangrande, C. Gerada, and M. Galea, "Thermal analysis of fault-tolerant electrical machines for aerospace actuators," in pres on IET Electric Power Applications, 2018.

[48] P. Giangrande, V. Madonna, G. Sala, A. Kladas, C. Gerada, and M. Galea, "Design and testing of pmsm for aerospace ema applications," in IECON 2018 - 44th Annual Conference of the IEEE Industrial Electronics Society, Oct 2018, pp. 2038–2043.

[49] S. A. Odhano, P. Giangrande, R. I. Bojoi, and C. Gerada, "Selfcommissioning of interior permanent- magnet synchronous motor drives with high-frequency current injection," IEEE Transactions on Industry Applications, vol. 50, no. 5, pp. 3295–3303, Sep. 2014.

[50] A. Al-Timimy, P. Giangrande, M. Degano, M. Galea, and C. Gerada, "Comparative study of permanent magnet-synchronous and permanent magnet-flux switching machines for high torque to inertia applications," in 2017 IEEE Workshop on Electrical Machines Design, Control and Diagnosis (WEMDCD), April 2017, pp. 45–51.

[51] Y. Burkhardt, A. Spagnolo, P. Lucas, M. Zavesky and P. Brockerhoff, "Design and analysis of a highly integrated 9-phase drivetrain for EV applications," 2014 International Conference on Electrical Machines (ICEM), Berlin, 2014, pp. 450-456. doi: 10.1109/ICELMACH.2014.6960219.

[52] S. Steentjes, G. von Pfingsten, M. Hombitzer and K. Hameyer, "Iron- Loss Model With Consideration of Minor Loops Applied to FESimulations of Electrical Machines," IEEE Transactions on Magnetics, vol. 49, no. 7, pp. 3945-3948, July 2013. doi: 10.1109/TMAG.2013.2244072.

[53] G. Yang, Z. Cui and L. Song, "Analysis of iron losses in induction motor with an improved iron-loss model," 2014 IEEE Conference and Expo Transportation Electrification Asia-Pacific (ITEC Asia-Pacific), Beijing, 2014, pp. 1-4. doi: 10.1109/ITEC-AP.2014.6940945.

[54] S. Xue, et al., "Iron Loss Model for Electrical Machine Fed by Low Switching Frequency Inverter," IEEE Transactions on Magnetics, vol. 53, no. 11, pp. 1-4, Nov. 2017, Art no. 2801004. doi: 10.1109/TMAG.2017.2696360.

[55] D. Golovanov, A. Galassini, L. Flanagan, D. Gerada, Z. Xu, and C. Gerada, "Dual-rotor permanent magnet motor for electric superbike," in 2019 IEEE International Electric Machines Drives Conference (IEMDC), May 2019, pp. 951–956.

[56] C. Gerada, M. Galea and A. Kladas, "Electrical machines for aerospace applications," 2015 IEEE Workshop on Electrical Machines Design, Control and Diagnosis (WEMDCD), Torino, 2015, pp. 79-84, doi: 10.1109/WEMDCD.2015.7194513.

[57] S. Zhang et al., "Permanent magnet technology for electric motors in automotive applications," 2012 2nd International Electric Drives Production Conference (EDPC), Nuremberg, 2012, pp. 1-11, doi: 10.1109/EDPC.2012.6425118.

[58] H. Tahanian, M. Aliahmadi and J. Faiz, "Ferrite Permanent Magnets in Electrical Machines: Opportunities and Challenges of a Non-Rare-Earth Alternative," in IEEE Transactions on Magnetics, vol. 56, no. 3, pp. 1-20, March 2020, Art no. 900120, doi: 10.1109/TMAG.2019.2957468.

[59] I. Boldea, L. N. Tutelea, L. Parsa and D. Dorrell, "Automotive Electric Propulsion Systems With Reduced or No Permanent Magnets: An Overview," in IEEE Transactions on Industrial Electronics, vol. 61, no. 10, pp. 5696-5711, Oct. 2014, doi: 10.1109/TIE.2014.2301754.

[60] M. Barcaro and N. Bianchi, "Interior PM Machines Using Ferrite to Replace Rare-Earth Surface PM Machines," in IEEE Transactions on Industry Applications, vol. 50, no. 2, pp. 979-985, March-April 2014, doi: 10.1109/TIA.2013.2272549.

[61] S. S. R. Bonthu, A. Arafat and S. Choi, "Comparisons of Rare-Earth and Rare-Earth-Free External Rotor Permanent Magnet Assisted Synchronous Reluctance Motors," in IEEE Transactions on Industrial Electronics, vol. 64, no. 12, pp. 9729-9738, Dec. 2017, doi: 10.1109/TIE.2017.2711580.

[62] Q. Chen, G. Liu, W. Zhao, M. Shao and Z. Liu, "Design and Analysis of the New High-Reliability Motors With Hybrid Permanent Magnet Material," in IEEE Transactions on Magnetics, vol. 50, no. 12, pp. 1-10, Dec. 2014, Art no. 8207010, doi: 10.1109/TMAG.2014.2342662.

[63] G. Lee, S. Kim, J. Hong and J. Bahn, "Torque Ripple Reduction of Interior Permanent Magnet Synchronous Motor Using Harmonic Injected Current," in IEEE Transactions on Magnetics, vol. 44, no. 6, pp. 1582- 1585, June 2008, doi: 10.1109/TMAG.2008.915776.